POLITECNICO DI MILANO

Facoltà di Ingegneria Industriale e dell'Informazione

Corso di Laurea in Ingegneria Biomedica

CHARACTERIZATION OF THE FLOW INSTABILITY IN PATIENT-SPECIFIC ARTERIOVENOUS FISTULAE FOR HEMODIALYSIS

Relatore: Prof. Gabriele Dubini

Correlatori: Prof. Andrea Remuzzi

Ing. Bogdan Ene-Iordache

Tesi di laurea di:

Michela Bozzetto

Matricola 801045

Anno accademico 2013/2014

Contents

List of figures

List of tables

Sommario

Introduzione

L’insufficienza renale terminale costituisce un problema sanitario in continua crescita a livello mondiale. Il numero di pazienti che soffrono di questa patologia nel mondo è stato stimato alla fine del 2012 di circa 3.010.000, con un tasso di crescita annuo del 7% [4].

L'emodialisi è il trattamento più comune per i pazienti affetti da insufficienza renale terminale. Per effettuare un trattamento efficacie è necessaria la costruzione di un accesso vascolare (AV) funzionale, che garantisca un prelievo di sangue sicuro ed adeguato dal paziente e un reinserimento dello stesso dopo che ha attraversato il circuito extracorporeo della dialisi. La fistola artero-venosa (FAV) proposta da Brescia e Cimino [8] rimane a tutt'oggi l'accesso permanente di prima scelta. Tale accesso è ottimale per la sua capacità di mantenere una buona pervietà a lungo termine e per la bassa incidenza di complicanze infettive e malattie trombotiche rispetto al graft artero-venoso e al catetere venoso centrale [13], [14]. La tecnica chirurgica di creazione della FAV consiste nel collegamento (anastomosi) dell’arteria radiale o brachiale con la vena cefalica, in modo da offrire tre un bypass dei vasi distali e fornire,quindi, un circuito a bassa resistenza, che risulta in un adeguato flusso di sangue attraverso l’accesso.

Nonostante i progressi clinici e tecnologici, la FAV presenta ancora oggi un notevole tasso di fallimento precoce, principalmente a causa della formazione di iperplasia neointimale [56]. Questa patologia è responsabile di stenosi venosa e conseguente trombosi, complicanza che solitamente si verifica in seguito a un periodo di malfunzionamento della FAV.

Diversi studi hanno discusso l'elevata correlazione tra la localizzazione delle stenosi e l’emodinamica locale, determinata dalla geometria dei vasi e dal *pattern* di flusso [28], [29], [32]. E’ stato osservato, infatti, che la modulazione del fenotipo endoteliale dipende dagli stimoli biomeccanici a cui questo è sottoposto e che è presente un forte legame tra lo sviluppo di iperplasia neointimale e la presenza di flusso disturbato. Recenti studi hanno

indicato che sforzi di taglio alla parete (wall shear stress, WSS) bassi e oscillanti contribuiscono a modificare il fenotipo endoteliale, rendendolo da "resistente" a "suscettibile" alla formazione di iperplasia neointimale [39]. Le simulazioni fluidodinamiche hanno indicato il ruolo dell'emodinamica come fattore scatenante della formazione di iperplasia neointimale nelle FAV, suggerendo una stretta correlazione tra flusso disturbato e sviluppo della neointima.

Questo lavoro di tesi ha avuto come obiettivo fondamentale la caratterizzazione della natura del flusso disturbato osservato in lavori precedenti su modelli *patient-specific* di FAV, ponendo particolare attenzione alla transizione da flusso laminare a flusso turbolento. L'obiettivo secondario è stato quello di confrontare il regime di moto presente nelle FAV con quello di una biforcazione carotidea, distretto caratterizzato da una geometria simile a quella delle FAV e da un flusso elevato, al fine di valutare se il flusso disturbato è presente anche in un distretto con condizioni fisiologiche o se il flusso disturbato caratterizza solo le FAV.

Materiali e metodi

Modelli 3D di FAV

La ricostruzione 3D delle FAV è stata realizzata a partire da immagini di risonanza magnetica raccolte 40 giorni dopo l'intervento chirurgico, utilizzando il Vascular Modeling Toolkit (*vmtk*) [57], una raccolta di librerie e strumenti che permette non solo la ricostruzione 3D, ma anche l'analisi geometrica e la generazione di mesh per le simulazioni fluidodinamiche (Figura 1).

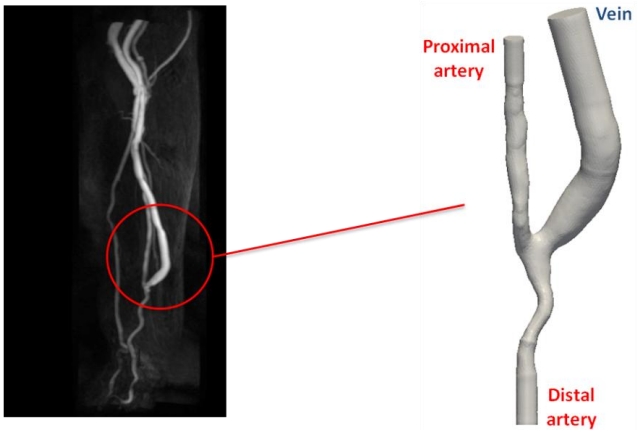

Figura 1 Esempio di immagine di risonanza magnetica e di ricostruzione 3D ottenuta con *vmtk*

In questo lavoro di tesi sono state ricostruite tre FAV *side-to-end* radio-cefaliche e tre FAV *side-to-end* brachio-cefaliche. Al fine di studiare la dinamica dei fluidi in modelli *patient-specific* di FAV abbiamo deciso di eseguire simulazioni numeriche nei modelli che presentavano una stenosi meno pronunciata.

Simulazioni numeriche del flusso di sangue nelle FAV

Le simulazioni numeriche sono state eseguite utilizzando *Gnuid* [60], un solver open-source progettato per risolvere le equazioni di Navier-Stokes per fluidi incomprimibili. La discretizzazione spaziale implementata in *Gnuid* si basa su uno schema *pressure-correction*, che combina un metodo di Galerkin (dG) discontinuo per la velocità e un metodo di Galerkin continuo (cG) per la pressione.

Le condizioni al contorno *patient-specific* imposte in Gnuid sono state ottenute utilizzando il solver Python Network (*pyNS*) [54], uno strumento open-source che permette di simulare il rimodellamento della parete dei vasi e le conseguenti variazioni del flusso sanguigno in seguito alla costruzione della FAV. Questo solver si basa sulla propagazione dell'onda di pressione attraverso un modello a parametri concentrati 0D/1D, nel quale la circolazione del braccio e l'anastomosi sono modellati utilizzando resistenze e induttanze disposte in serie, mentre l'aorta, i vasi della parte inferiore del corpo, il braccio controlaterale e la testa sono modellati solo parzialmente utilizzando elementi di tipo Windkessel (Figura 2).

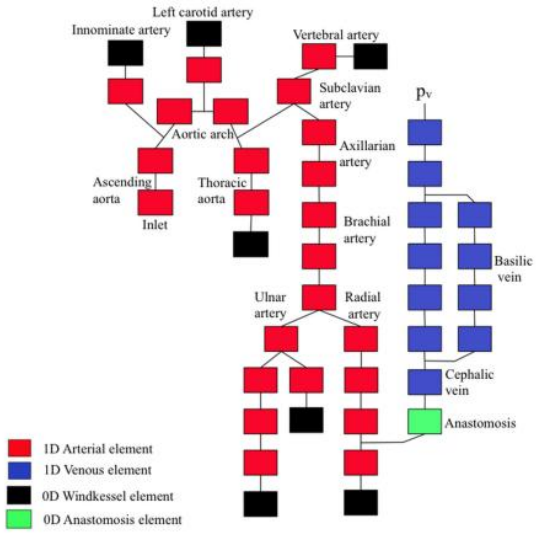

Figura 2 Elementi del network del braccio sinistro con una FAV *side-to-end*

Le forme d'onda del flusso in l'ingresso e in uscita sono state estrapolate da pyNS, utilizzando la forma d'onda di flusso del segmento di arteria più vicino alla anastomosi.

La condizione al contorno di pressione nulla è stata impostata all'uscita della vena e, al fine di garantire una condizione di non-scivolamento, è stata applicata velocità nulla alle pareti, che sono state considerate rigide. Il sangue è stato considerato un fluido newtoniano e incomprimibile, con densità costante di 1.045 g/cm^3. La viscosità dinamica del sangue è stata calcolata dai dati specifici del paziente.

Simulazioni numeriche effettuate

In questo lavoro di tesi, le simulazioni CFD sono state eseguite su due FAV radio-cefaliche e su due FAV brachio-cefaliche. Per ogni simulazione sono stati risolti due cicli cardiaci completi in modo da smorzare i transitori iniziali del fluido. La tabella 1 contiene i dati principali delle simulazioni CFD; lo *scaling factor* indica la percentuale di flusso che attraversa l'arteria distale rispetto al flusso di ingresso nell'arteria prossimale.

PATIENT	**BC 20008**	**BC 20018**	**RC 20005**	**RC 20009**
Mesh [elements]	855327	668853	1259417	1053447
Qmean inlet [mL/min]	866.06	1104.35	531.78	591.51
Qmean outlet [mL/min]	22.2	41.86	19.73	13.52
Scaling factor [%]	2.56	3.79	3.71	0.02
Re inlet	1517	1450	969	1502
α inlet	3.86	4.26	3.28	3.40
Blood viscosity [Poise]	0.027	0.034	0.024	0.024

Tabella 1 Dati delle simulazioni CFD

Nella seconda parte del nostro studio sono state eseguite quattro simulazioni supplementari al fine di studiare l'influenza dei seguenti parametri sulla soluzione: il numero di elementi della mesh, la posizione della condizioni al contorno di pressione nulla e la variazione della portata volumetrica di sangue.

Risultati

Generici pattern di flusso

Le *streamlines* 2D e 3D del vettore velocità appaiono rettilinee nell'arteria prossimale e si evolvono in vortici e flussi secondari nell'anastomosi.

L'andamento della velocità in alcuni punti caratteristici è stato descritto lungo la *centerline* di ogni modello simulato, rivelando flusso laminare nell'arteria prossimale di ingresso e significativa instabilità subito dopo l'anastomosi (Figura 3).

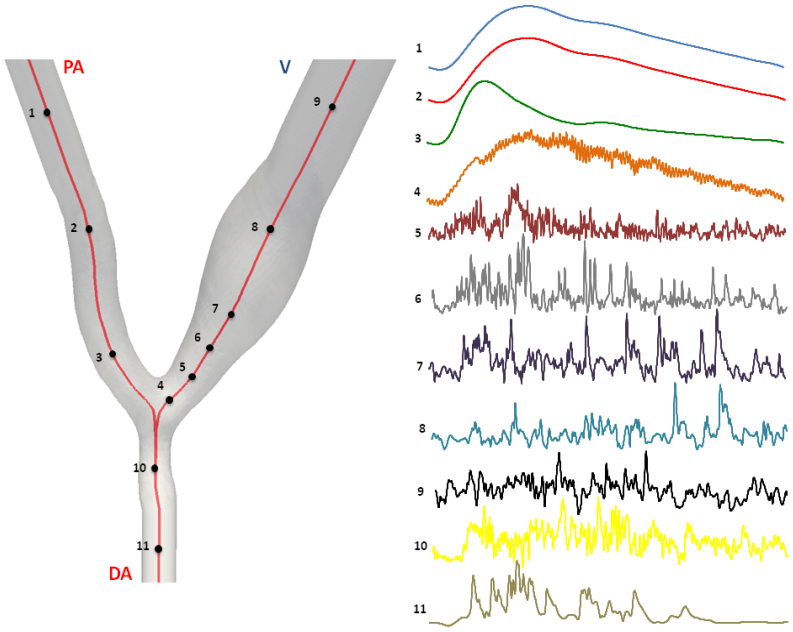

Figura 3 Esempio dei trend di velocità in funzione del tempo in alcuni punti specifici selezionati nella FAV RC 20018

Le isosuperfici che rappresentano l'intensità del vettore velocità hanno rivelato la complessità del flusso: subito dopo l'anastomosi esse hanno perso la forma ben costruita e l'uniformità mostrate nell'arteria prossimale, si sono fratturate e sono andate a riempire solo una parte limitata del vaso, mostrando l'instabilità di flusso caratteristica della vena.

I pattern di WSS hanno mostrato valori alti in corrispondenza dell'anastomosi, caratteristica comune a tutte le FAV.

Parametri di flusso disturbato

Aree con basso TAWSS sono state riscontrate lungo la parete dell'anastomosi, sulla parete interna della vena e sulla parete interna dopo la curvatura della vena e zone con OSI non nullo sulla parete interna della vena dopo l'anastomosi e sull'arteria distale. Valori non nulli e oscillanti di transWSS, la componente di WSS perpendicolare alla direzione media del flusso, riscontrati in tutti i casi simulati confermano l'instabilità e la natura multidirezionale del flusso vicino alla parete.

Infine, per quanto riguarda l'influenza di alcuni parametri sull'instabilità del flusso, il risultato più interessante è stato ottenuto diminuendo la portata volumetrica: questa diminuzione corrisponde ad una diminuzione di OSI, in particolare sulla parete interna della vena, e a uno smorzamento di oscillazioni dell'intensità del WSS sulla vena stessa.

Confronto con una normale biforcazione carotidea

Al fine di capire se l'instabilità di flusso può verificarsi anche in una biforcazione carotidea sana, sottoposta a una portata di sangue fisiologica, è stata fatta una simulazione numerica utilizzando lo stesso solver *Gnuid*. Le *streamlines* 2D e 3D del vettore velocità hanno segnalato la presenza di flusso laminare in tutta la biforcazione carotidea e i trend di velocità escludono la presenza di qualsiasi instabilità (Figura 4).

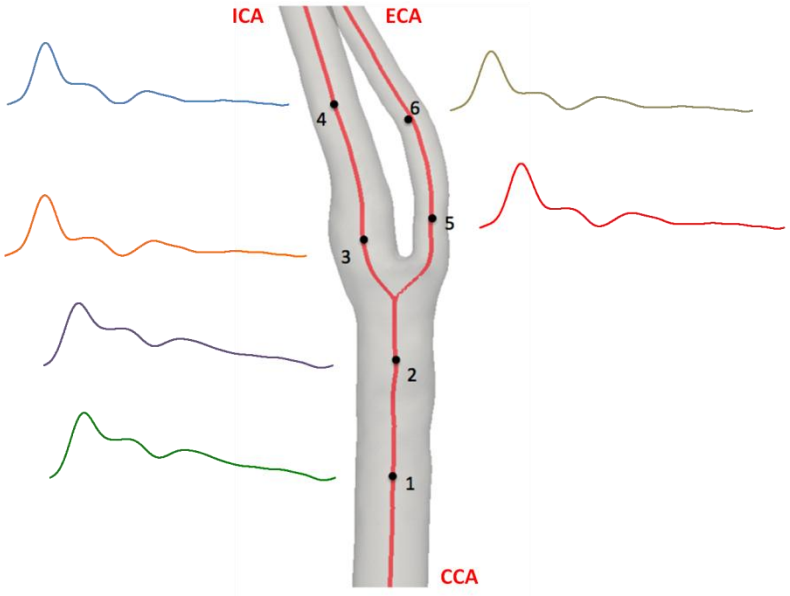

Figura 4 Trend di velocità in funzione del tempo in alcuni punti specifici selezionati nel modello di carotide

Discussione

In questo lavoro di tesi, mediante simulazioni fluidodinamiche con flusso pulsatile in modelli *patient-specific* di FAV, è stato possibile descrivere la natura del flusso disturbato, ponendo particolare attenzione all'instabilità del flusso.

In tutti i casi simulati è stata osservata la presenza di un regime di moto di transizione da laminare a turbolento in corrispondenza dell'anastomosi e lungo l'arteria distale: flusso laminare è stato rilevato nell'arteria prossimale, mentre flussi secondari e vortici locali nella vena e nell'arteria distale; i trend di velocità hanno mostrato la presenza di instabilità subito dopo l'anastomosi, smorzata man mano che ci si sposta verso la vena distale o in seguito alla diminuzione della portata, in linea con i trend di velocità trovati da Valen-Sendstad et al. [76] nel sifone carotideo. Le oscillazioni dei vettori velocità nelle FAV hanno dato come conseguenza valori bassi e oscillanti di WSS sulla superficie interna della vena e sulla arteria distale, in linea con precedenti studi *patient-specific* [46], [50], [51].

I *pattern* di TAWSS e OSI rappresentati per tutti i modelli di FAV hanno confermato i *pattern* trovati nel precedente lavoro di tesi di Semperboni [53].

Studiando i parametri che possono influenzare il passaggio dal regime di flusso turbolento a quello laminare, il risultato più importante è stato ottenuto riducendo la portata: le zone di flusso disturbato (alto OSI) sono diminuite e l'elevata instabilità di velocità e WSS tracce ha mostrato un'attenuazione significativa.

Una simulazione fluidodinamica eseguita su una normale biforcazione carotidea ha mostrato flusso laminare in tutte le regioni del modello e ha quindi portato alla conclusione che l'instabilità di flusso trovata nella FAV non è presente in questo distretto vascolare, perlomeno in caso di flusso fisiologico e assenza di stenosi.

Sviluppi futuri

In questo studio è stato osservato in tutte le FAV simulate un flusso di transizione nella vena.

Lo sviluppo di questo flusso oscillante e multi-direzionale può determinare la formazione di iperplasia neointimale nella FAV appena creata.
Sulla base di questa ipotesi, due principali sviluppi futuri potrebbero essere ipotizzati:

- L’analisi del flusso utilizzando un stetoscopio elettronico (3M Littmann) per la registrazione del suono, seguita da analisi software. Studi precedenti [88], [89] hanno indicato che l'analisi della forma d'onda registrata dallo stetoscopio è in grado di rilevare le caratteristiche del suono associate al passaggio del flusso da laminare a turbolento a valle del sito di stenosi vascolare. Poiché gli studi angiografici sono costosi e invasivi e l'accuratezza diagnostica dell’ ecografia è sempre disponibile quando si verifica una diminuzione del flusso, l’auscultazione sembra essere un metodo monitoraggio semplice ed efficacie.

- Realizzazione di un dispositivo in grado di sottoporre le cellule endoteliali ai pattern di flusso e di velocità risultanti da simulazioni CFD. Davies et al. [90] hanno esposto le cellule a un flusso turbolento, anche in presenza di bassa intensità del vettore WSS. Anche Fry et al. [91] e Prado et al. [92] hanno rilevato che, esponendo le cellule a pattern di velocità e di WSS modelli con fenotipi simili a quelli presentati in questa tesi, l’endotelio nelle regioni di flusso turbolento presentava placche neointimali.

Abstract

Introduction

End-stage renal disease (ESDR) is a growing global health problem. The number of patients being treated for ESDR globally was estimated to be 3.010.000 at the end of 2012, with a grow rate of 7% per year [4].

Hemodialysis is the most common treatment for patients suffering from renal failure.
A successful hemodialysis procedure requires a functional vascular access (VA) that provides a safe and effective way of withdrawal and return of blood to the extracorporeal circuit: the access of first choice is the arteriovenous fistula (AVF) [8], that is optimal for its capability of maintaining a good long-term patency and for the low incidence of infective complications and thrombotic diseases, compared to the arteriovenous graft and to the central vein catheter [13], [14]. The AVF is usually created through the surgical anastomosis of the radial or brachial artery to the cephalic vein: this procedure offers a bypass of the distal vessels, providing a parallel low-resistance circuit that results in adequate high blood flow rate through the VA.

Despite clinical and technological advancements, the AVF still has significant early failure rates, mainly due to the formation of neointimal hyperplasia related to hemodynamic conditions [56]. This process is the more responsible for venous stenosis and consequent thrombosis, the final complication after a period of AVF dysfunction.

Several studies have discussed the high correlation between the localization of the stenoses and local hemodynamics determined by the vessel geometry and the blood flow pattern [28], [29], [27]. It has been demonstrated that the modulation of endothelial phenotype depends on the biomechanical stimuli and a strong relationship between the development of neointimal hyperplasia and the presence of disturbed flow has been noticed. Recent studies have indicated that low and reciprocating wall shear stress (WSS) contributes to change the endothelial phenotype from atheroprotective to atheroprone, that is susceptible to the formation of neointimal hyperplasia [39]. Computational fluid dynamics determined

the hemodynamics role as an upstream event in the ignition and formation of neointimal hyperplasia in the AVF.

The present thesis was aimed at investigating and characterizing more in detail the nature of the flow instability found in previous studies, with special attention on the transition from laminar to turbulence in patient-specific AVF. The secondary aim was to compare the flow pattern observed in the AVF model with the flow pattern of a normal carotid bifurcation, a vascular segment characterized by a complex geometry with high flow rate, in order to investigate to which extent flow instability may develop also in physiological conditions or if it characterizes selectively the AVF.

Matherials and methods

3D models of the AVF

3D models reconstruction has been realized starting from MRA images collected forty days after surgery, using the Vascular Modeling Toolkit (*vmtk*) [57], a collection of libraries and tools for 3D reconstruction, geometric analysis and mesh generation for image-based modeling of blood vessels (Figure 1).

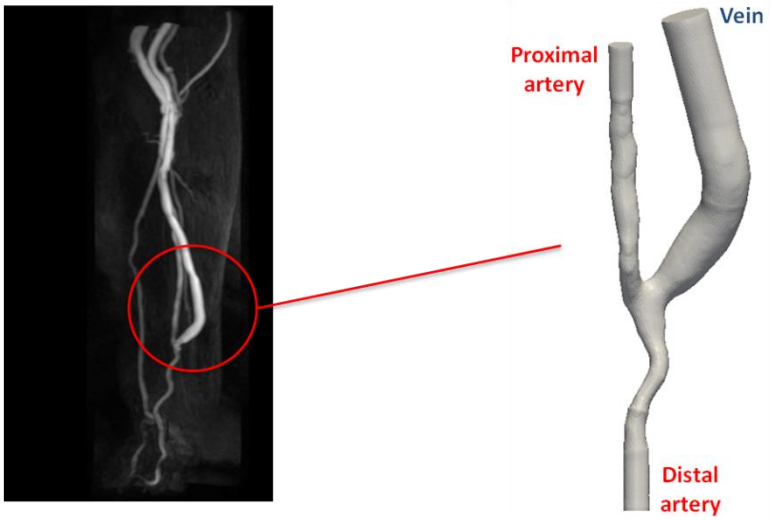

Figure 1 Example of MRA image and 3D reconstruction obtained using *vmtk*

In the present thesis three radio-cephalic and three brachio-cephalic side-to-end AVF have been reconstructed. In order to study the fluid dynamics in patient-specific AVF, we have decided to run CFD simulations in the less stenotic models.

Numerical simulations of blood flow in the AVF

Numerical simulations have been performed using *Gnuid* [60], an open source solver for the incompressible Navier-Stokes equations. The discrete formulation of *Gnuid* is based on a pressure-correction scheme, combining a discontinuous Galerkin (dG) approximation for the velocity and a standard continuous Galerkin (cG) approximation for the pressure.

Patient-specific boundary conditions imposed on *Gnuid* have been obtained using Python Network solver (pyNS) [54], an open open-source solver which allows to simulate vessel wall remodeling and related changes in blood flow. The model is based on 0D/1D pulse wave propagation model of lumped parameters segments with serial arrangement of resistor and inductor, representing detailed arm circulation together with the anastomosis, whereas the aorta and the vessels in the lower body, contralateral arm and the head are partially modeled with three element Windkessel segments (Figure 2).

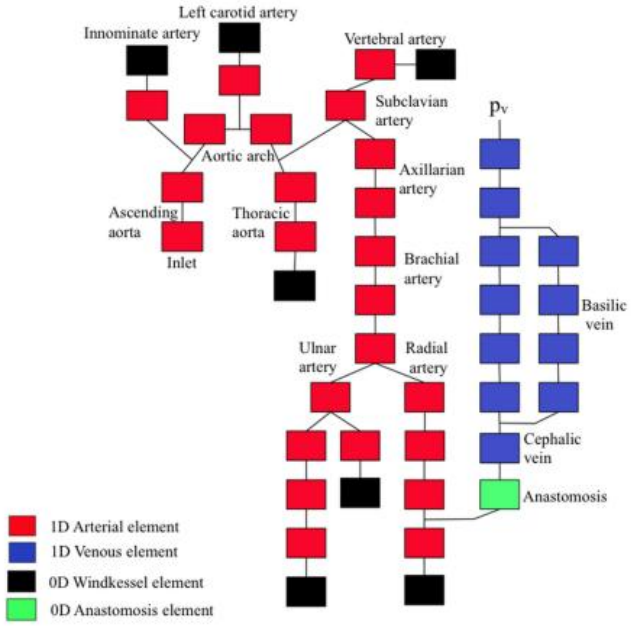

Figure 2 Elements of the network of the left arm with side-to-end AVF

The flow rate waveform used for the inlet and outlet was extrapolated from pyNS, using the flow waveform of the artery segment closer to anastomosis.

Zero-pressure boundary condition has been set on the vein outlet and zero-velocity on the walls, which were considered rigid, has been applied to ensure no-slip condition. Blood has been considered a Newtonian and incompressible fluid, with constant density of 1.045 g/cm^3. The dynamic blood viscosity has been calculated from patient specific data.

Computed simulations

In the present work, CFD were performed on two radio-cephalic and two brachio-cefalic AVF. For every simulations two complete cardiac cycles were solved in order to damp the initial transients of the fluid. Table 2 contains the most important CFD patient-specific data; the scaling factor indicates the percentage of flow through the distal artery, determining the partition of blood flow.

PATIENT	**BC 20008**	**BC 20018**	**RC 20005**	**RC 20009**
Mesh [elements]	855327	668853	1259417	1053447
Q mean inlet [mL/min]	866.06	1104.35	531.78	591.51
Q mean outlet [mL/min]	22.2	41.86	19.73	13.52
Scaling factor [%]	2.56	3.79	3.71	0.02
Re inlet	1517	1450	969	1502
α inlet	3.86	4.26	3.28	3.40
Blood viscosity [Poise]	0.027	0.034	0.024	0.024

Table 2 CFD data

In the second part of our study four additional simulations have been computed in order to study the influence of the following parameters on the solution: mesh density, zero-pressure boundary condition and blood volumetric flow rate.

Results

General flow pattern

Velocity 2D and 3D streamlines appeared straight in the proximal artery and evolved in vortices and secondary flow in the anastomosis. The velocity trend in some feature points have been described along the centerline of every simulated model, revealing laminar flow in the proximal feeding artery and flow instability right after the anastomosis (Figure 3).

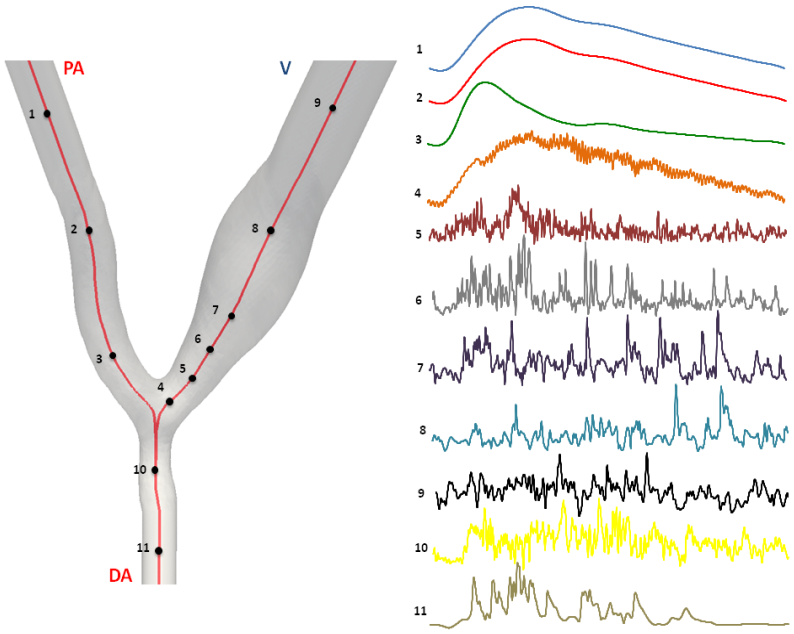

Figure 3 Example of velocity vs. time traces at selected probe points of RC 20018

The increase in flow complexity is revealed by velocity magnitude isosurfaces: right after the anastomosis the surface loses the well-constructed shape and the smoothness shown in the proximal artery: it breaks and fills just a limited part of the vessel, revealing the flow instability characteristic for the vein.

Wall shear stress patterns revealed high WSS at the anastomosis, which is a common feature for all the AVF.

Disturbed flow parameters

Areas of low TAWSS were found along the wall of the anastomotic floor, near the anastomotic heel on the inner wall of the vein and on the inner wall after the curvature of the vein. Non-null OSI zones were found on the inner wall of the vein after the anastomosis and on the distal artery. Non-zero and oscillating transWSS in high OSI zones

represented in all the simulated cases the instability and the multidirectional nature of the flow near the wall.

Finally, regarding the influence of some parameters on flow instability, it's been demonstrated that the most interesting result is obtained descreasing the volumetric flow rate: it corresponds to a decreasing of OSI, especially on the inner wall of the vein and a damping of oscillation of WSS magnitude in the vein.

A comparison with a normal carotid

With the aim of establishing whether flow instability may occur also in a healthy carotid bifurcation with physiological blood volumetric flow rate, it has been simulated with the same solver used for the AVF. 2D and 3D velocity streamlines revealed laminar flow in the whole carotid bifurcation and velocity traces ruled out any presence of instability (Figure 4).

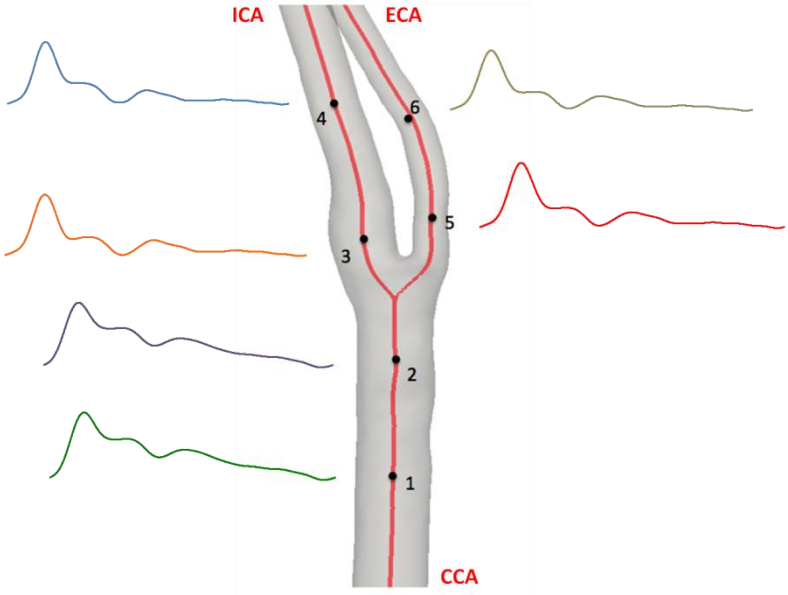

Figure 4 Velocity vs. Time traces, normalized by their respective cycle averages, at selected probe points of the carotid model

Discussion

In the present thesis, by employing pulsatile CFD simulations in patient-specific models it was possible to describe the nature of the disturbed flow, with focus on flow instability.
In all simulated cases, transitional laminar-to-turbulent flow developing in the juxta-anastomotic vein and along the distal artery was observed.
Laminar flow in the proximal artery and secondary flows and local vortexes in the venous and distal artery segment were found and velocity traces revealed instability right after the anastomosis that damped moving towards the distal vein, or by decreased flow rate, in line with velocity traces found by Valen-Sendstad et al. [76] in the carotid siphon. The oscillations of the velocity vectors in the AVF result in low and reciprocating WSS on the inner surface of the juxta-anastomotic segment and on the distal artery, in line with previous patient-specific studies [46], [50], [51].

Maps of TAWSS and OSI as indicators of disturbed flow were obtained in all AVF models, with localizations as demonstrated in the previous thesis work by Semperboni [53].

By studying which parameters may affect the transition from turbulence to laminar flow, we have found that the most important was the reducing of the flow rate: the disturbed flow zones (high OSI) diminished accordingly and the high instability of both velocity and WSS traces showed a significant damping.

A comparison CFD study performed on a normal carotid bifurcation, revealing laminar flow in all the regions of the model, led to the conclusion that the flow instability found in the AVF is not observed in such a vascular district, at least for physiological flow and absence of stenosis.

Future developments and perspectives

In this study transitional flow developing in the juxta-anastomotic vein has been observed in all AVF cases. The development of both oscillating and multi-directional disturbed flow may sum together to boost the neointima formation in the newly created AVF.

On the basis of this hypothesis, two main future developments could be imagined:

- Investigation of the flow status by using an electronic stethoscope (3M Littmann) for AVF sound recording, followed by software analysis. Previous studies [88], [89] indicated that stethoscope waveform analysis can detect sound features associated with the change from laminar flow to turbulent flow downstream the site of vascular stenosis. As VA angiographic studies are expensive and invasive and diagnostic accuracy of color duplex ultrasound in AVF stenosis is not always available when decreased flow occurs, auscultation seems to be a simple monitoring method to assess the VA.

- Realization of a device that can impose flow and velocity patterns resulting from CFD simulations to the EC. Davies et al. [90] exposed EC to a turbulent flow, even with low WSS magnitude. Also Fry et al. [91] and Prado et al. [92] found that the EC in the turbulent region were non-directional and neointimal plaques were focally distributed, by exposing EC to velocity and WSS patterns that are phenotipically similar to those presented in this thesis

1. Clinical background

The present chapter contains the physio-pathological aspects of the renal apparatus with particular reference to the vital functions and the conditions in which these are compromised, causing renal failure. Some epidemiological data are provided, starting from the global condition and moving to the Italian situation. Furthermore, the main kidney's replacement treatments are described, focusing on hemodialysis. Finally, the main kinds of vascular access, the crucial component of hemodialysis circuit, are analyzed, underlying the general consensus in the literature and in the vascular access guidelines on the superiority of arteriovenous fistula over arteriovenous graft and central venous catheter.

1.1 Physiology of the kidney

1.1.1 Kidney's anatomy

The kidneys are a pair of organs lying on either side of the vertebral column between the peritoneum and the back wall of the abdominal cavity at the level of the twelfth thoracic vertebra. The fissure on the medial border of each kidney is called hilum: this is the region where the renal arteries enter and the veins exit the kidney. Here is also where the renal pelvis, whose major function is to act as a funnel for urine flowing to the ureter, occurs. The external part of the pelvis is divided into chambers called calices, which converges to the ureter and whose main function is to collect the urine coming from the pelvis.

Each kidney has two main regions: the outer renal cortex and the inner renal medulla.

The cortex is reabsorbing the filtered material, while the medulla is a highly metabolically active area, which serves to concentrate the urine (Figure 1.1).

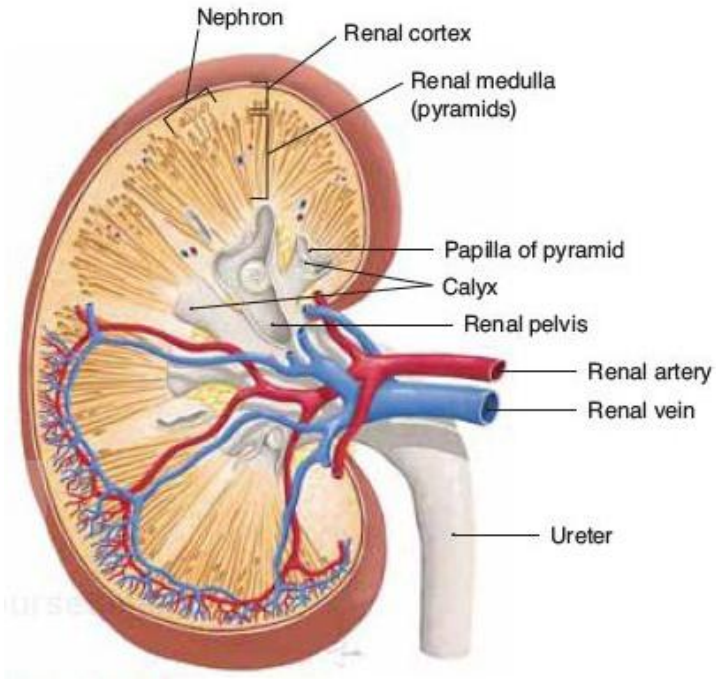

Figure 1.1 Main anatomic components of the kidney

The basic structural and functional unit of the kidney is the nephron, a tiny and complex filtering structure composed of two parts: the glomerulus, which filters high quantities of solutes and water, and the renal tubule, which reabsorbs most of the filtered load, including nutrients and electrolytes.

The glomerulus is a network of capillaries, which receives its blood supply from an afferent arteriole and drains into an efferent arteriole. The resistance of these arterioles results in high pressure within the glomerulus, aiding the ultrafiltration, the process in which fluids and soluble materials in the blood are forced out of the capillaries and into Bowman's capsule. The filtered liquid then flows to the renal tubule, through the proximal tubule first and the loop of Henle then. Here the fluid is reabsorbed into the peritubular capillaries, including approximately two-thirds of the filtered salt and water and all filtered organic solutes. After passing through the renal tubule, the filtrate continues to the collecting duct system and leaves the medullary collecting ducts through the renal papillae, emptying into the renal calyces, the renal pelvis, and finally into the urinary bladder via the ureter (Figure 1.2).

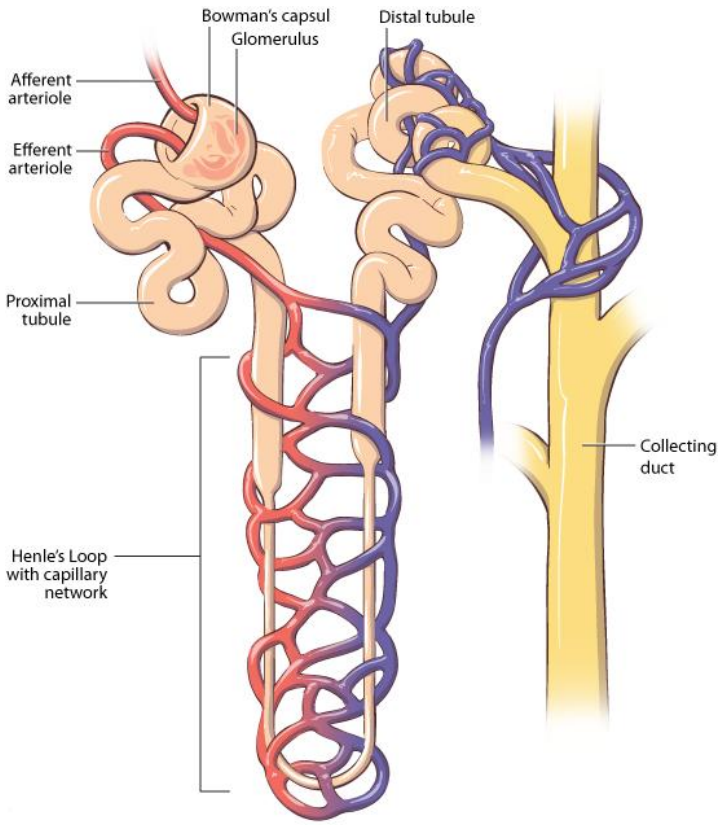

Figure 1.2 Main structures of the nephron: the glomerulus and the renal tubule

Normally, the kidneys receive 1 to 1.25 L/min of blood, which represent about 20% of the cardiac output. This amount far exceeds that needed to provide the kidney's intrinsic oxygen requirement but ensures optimal clearance of all wastes.

The main processes occurring in the kidneys producing urine are:

1) *Filtration*: it takes place between the glomerular capillaries and the Bowman's capsule; every day the kidneys filter about 180 L of plasma: the composition of the filtered liquid is similar to the plasma, except for cells and proteins that are contained in it.
2) *Reabsorption*: it consists on the recovery of water and filtered solutes, flowing from the tubules to the capillaries. The main substances are glucose, low molecular weight proteins, vitamins, water and salts.
3) *Secretion*: it is the process during which some substances flows from the blood to the renal tubules, adding to the filtered solutes. Substances that need rapid removing (drugs and H^+ ions) are among these solutes.

1.1.2 Kidney's functions

The kidneys perform a wide range of vital functions, maintaining the homeostasis of the organism and the constant composition and volume of body fluids.

The main functions of the kidneys are:

1) Removal of excess water from the blood in order to balance the volume of extracellular fluid;
2) Removal of metabolic wastes: urea, creatinine, uric acid and toxins;
3) Regulation of osmolarity and concentration of the electrolytes (Na^+, K^+, Cl^-, HCO_3^-, PO_4^{3-}, Ca^{2+});
4) Regulation of acid-base balance secreting H^+ and reabsorbing HCO_3^-;
5) Regulation of arterial pressure by mean of water and vasodilator factors;
6) Release of hormones: eritropoyetina, renine, calcitriolo and prostaglandins;
7) Glucogenesis.

1.2 Renal failure

Renal pathologies are one of the main causes of death and invalidity in all the countries. They can be distinguished in two main categories:

- *Acute Kidney Injury (AKI):* usually develops rapidly in response to decreased renal blood flow (renal ischemia), exposure to substances harmful to the kidney, inflammatory process in the kidney or obstruction of the urinary tract which impedes the flow of urine. Usually this condition is reversible and does not cause permanent damage.

- *Chronic Kidney Disease (CKD):* usually results from gradual and permanent loss of kidney function over time and it may take from months to years. It causes an accumulation of liquids and toxins in the tissues resulting in iperazotemia and uremia. Because renal replacement therapy (RRT) or transplantation is required to survive, the pathological condition is called end stage renal disease (ESRD).

1.2.1 Etiology and classification of CKD

The etiology of renal failure can be quite various and depends upon the particular event that initiates kidney damage. In the developed countries the three main causes of CKD are diabetes, high blood pressure and glomerulonephritis, a group of diseases that cause inflammation and damage to kidney's filtering units. Also inherited kidney disease, such as the polycystic kidney disease (PKD), which causes large cysts formation in the kidney damaging the surrounding tissue, is a diffused cause of CKD. If uncorrected, any of these events can lead to renal failure [1]. Figure 1.3 shows the incidence of the main pathologies causing renal failure, registered in the Italian report (RIDT) of 2010 [2]:

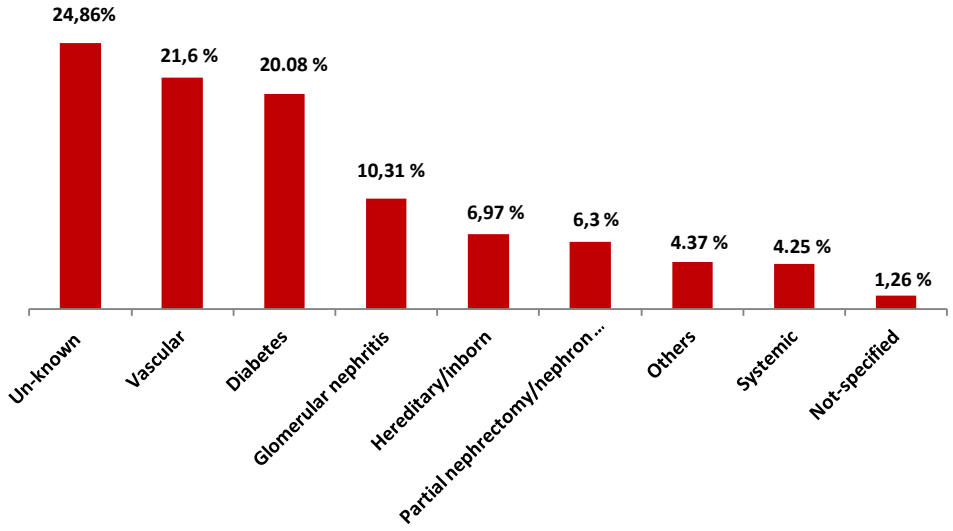

Figure 1.3 Incidence of different causes of CKD [2]

Glomerular filtration rate (GFR) has been accepted as the best index of overall kidney function in health and disease. The guidelines called Kidney Disease Outcomes Quality Initiative (KDOQI) [3] published by National Kidney Foundation, defined several stages of CKD, which can lead to decreased GFR:

- *Stage I*: it is characterized by the presence of structural or functional abnormalities of the kidney, initially without decreased GFR (> 90 mL/min/1.73 m^2), which over time can lead to decreased GFR.
- *Stage II:* it is characterized by mild reduction in GFR (60 to 89 mL/min/1.73 m^2). At this stage, patients usually have hypertension and may have laboratory abnormalities indicative of dysfunction. This condition can be determined by measurements of serum creatinine levels.
- *Stage III*: it is characterized by moderate reduction in GFR (30 to 59mL/min/1.73 m^2). This stage is distinguished by the presence of azotemia (nitrogen metabolism) and expressed by an elevation in serum creatinine and serum urea nitrogen.
- *Stage IV:* it is characterized by severe reduction in GFR (15 to 29mL/min/1.73 m^2). In this extreme stage of CKD, the worsening of azotemia, anemia and other laboratory abnormalities reflect dysfunction in several organ systems.

- *Stage V*: it is characterized by kidney failure (GFR, <15 mL/min/1.73 m^2). In most cases, this level of kidney dysfunction is accompanied by a constellation of symptoms and laboratory abnormalities in several organ systems. Kidney replacement therapy (dialysis or transplantation) is typically required.

1.2.2 Epidemiology of ESRD

End stage renal disease is a growing global health problem, strictly connected with progressive ageing population and increased survival rate of CKD patients. The number of patients being treated for ESRD globally was estimated to be 3.010.000 at the end of 2012 and, with a ~7% growth rate, continues to increase at a significantly higher rate than the world population. In the US, Japan and the European Union, dialysis population growth rates are significantly lower than the growth rates in regions such as Asia, Latin America, Middle East and Africa. This variation in growth rates may be partially explained by differences in demographics and the maturity of dialysis programs in developed countries [4].

In Italy, the RIDT of 2010 for dialysis and transplantation shows data with similar trend of the global view: 42.488 patients in hemodialysis, with a prevalence of 788 pmp, and 8.638 new patients compared to the previous year, registering a incidence of 162 pmp [2]. Figure 1.4 shows the trends of prevalence and incidence in the years 2005 to 2010:

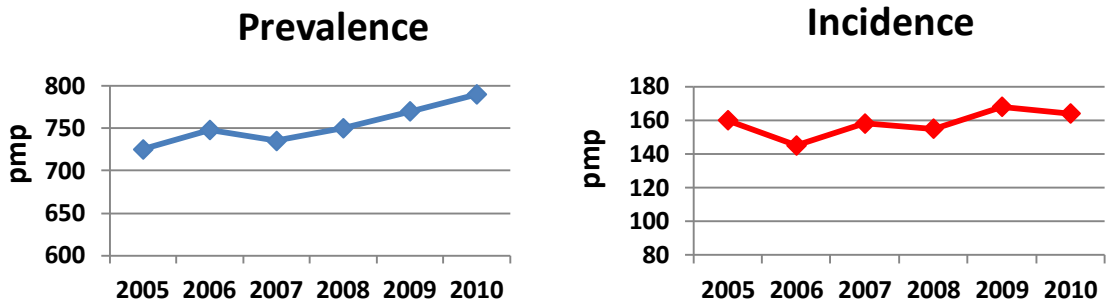

Figure 1.4 Historical trend of incidence and prevalence of hemodialysis patients in Italy between 2005 and 2010 [2]

The survival alternatives for a patient suffering from renal failure are chronic dialysis treatments (either hemodialysis or peritoneal dialysis) and renal transplantation. Worldwide, hundreds of thousands of patients are currently treated with dialysis, due to the limited number of donors.

1.3 Dialysis treatments

The first historical description of the dialysis procedure was published in 1913. Abel, Rowntree and Turner "dialyzed" anesthetized animals by directing their blood outside the body and through tubes with semi permeable membranes [5]. George Haas, a German doctor, was the one who performed the first attempt of dialysis involving humans. Thanks to the technical improvements in the equipment, in 1945 Willem Kolff performed the first successful dialysis treatment [6]. Doctor Kolff's success proved the usefulness of the concepts developed by Abel and Haas: the separation of substances and the removal of water from solutions through semipermeable membranes (diffusion and osmosis processes).

There are two main types of dialysis:

- Hemodialysis: it uses an extracorporeal circuit with a special filter to cleanse the blood of the patient;
- Peritoneal dialysis: this treatment uses the peritoneal cavity in the abdomen as a reservoir for the dialysis solution and the thin membrane lining this cavity as a suitable barrier through which blood can be filtered.

Nowadays, hemodialysis is the most common treatment, with approximately 2.106.000 patients undergoing hemodialysis (89% of all dialysis patients) and about 252.000 patients undergoing peritoneal dialysis (11%) [3].

1.3.1 Hemodialysis

Hemodialysis is a blood purifying therapy that allows to replace the three main functions of the kidney:

- removing wastes, such as urea, from the blood;
- restoring the proper balance of electrolytes in the blood;
- eliminating extra fluid from the blood.

This procedure is realized in an extracorporeal circuit (dialyzer), shown in Figure 1.5, where two needles can be used to access patient's vascular system. Blood is withdrawn from the body via the arterial needle by a peristaltic pump, circulated through the dialyzer, and then returned to the patient through the venous needle. Heparin is infused downstream from the blood pump in order to avoid blood coagulation.

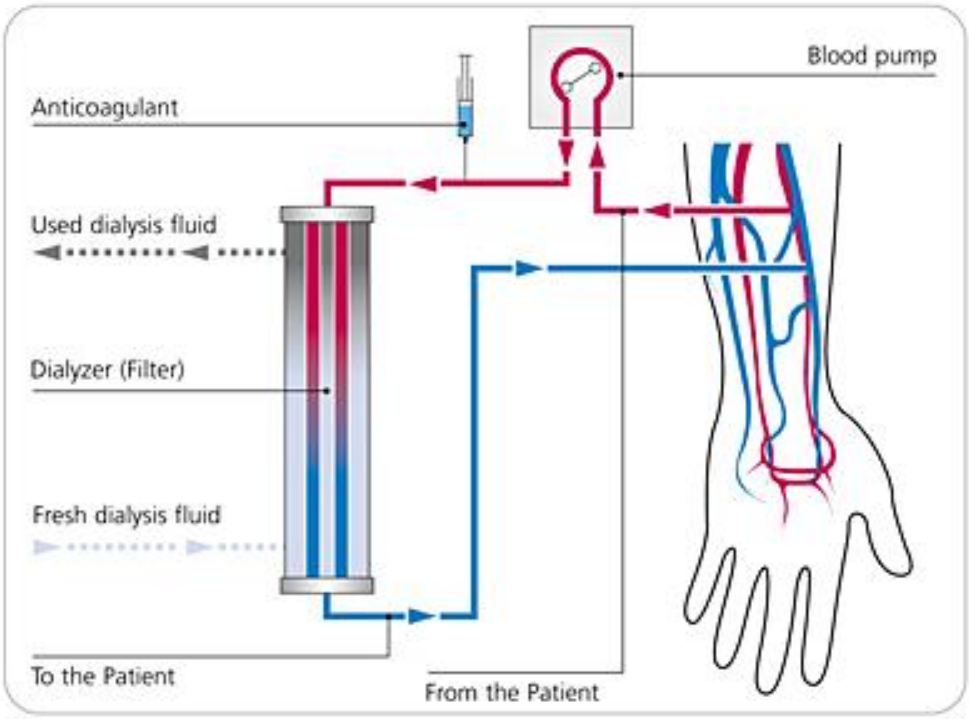

Figure 1.5 Hemodialysis circuit with the main components

Within the dialyzer the blood flows through hollow fibers surrounded by a semi-permeable membrane separating the blood from a liquid (dialysate), a solution of water, acid solution and bicarbonate, which is critical in achieving the desired blood purification, body fluid and electrolyte homeostasis. Diffusive and convective mass transfer occur across the semi-

permeable membrane characterized by 50 Å diameter pores, allowing changes in the composition of body fluids. Diffusive transport, the net movement of a solute from a region of higher concentration to a region of lower concentration, depends on solute molecular weight and charge, trans-membrane concentration gradients, blood and dialysis fluid flow rates and membrane characteristics. Small molecules (e.g. urea) are cleared well through diffusive transport. The diffusive flow through the membrane is defined as:

$$J_{diff} = P_L \cdot \Delta C$$

where P_L is the permeance of the membrane (permeability on the length unit in the direction of the diffusion) and ΔC is the concentration gradient.

In addition to the removal of wastes through diffusion, the other task of the dialyzer is to remove extra water that tends to lie in the blood of patients with ESRD. Ultrafiltration (UF) consists in a convective flow across a semi-permeable membrane in response to a trans-membrane pressure gradient and improves the clearance of poorly diffusible middle-sized molecules (e.g. 2-microglobulin). The convective flow through the membrane is defined as:

$$J_{conv} = L_P(\Delta P - \Delta\pi)$$

where L_P is the filtration coefficient of the membrane, ΔP the pressure drop between blood and dialysate and $\Delta\pi$ the difference between the osmotic pressure in the dialysate and in the blood due to the presence of proteins. For regular dialysis at blood flow up to 250 mL/min the dialysate should be 500 mL/min.

Hemodialysis is usually performed three or more times a week for 4 hours: the primary need is an adequate vascular access that can provide adequate flows and can ensure adequate time of the treatment.

1.4 The vascular access

A successful hemodialysis procedure requires a functional vascular access (VA) that provides safe and effective way of withdrawal and return of blood to the extracorporeal circuit.

The first article describing the importance of an adequate access to the blood circuit, required for chronic hemodialysis, was published in 1944 by the pioneer of the first hemodialysis in humans, Willem Kolff [6]. It took other 16 years before Quinton and Scribner introduced the first permanent vascular access: the Scribner shunt [7]. This device consisted of 2 tubes connecting the patient to the dialyzer: one was inserted into a suitable peripheral artery and one into a vein. After the treatment, the circulatory access was maintained by connecting the two tubes outside the body using a small U-shaped device over a stainless steel plate. The major disadvantages of Scribner shunts were high thrombosis and infection rates, resulting in a limited shunt and hence patient life span. In 1966, Brescia and Cimino solved the VA problem with a surgically created arteriovenous fistula (AVF) between the radial artery and the cephalic vein at the wrist [8]. This new VA was able to deliver flow rates of 250-300 mL/min for unlimited time. Results were satisfactory, 13 AVF functioned without any complication and two failed before cannulation. Exposure to high-pressure arterial flow promoted enlargement and thickening of the venous wall. After approximately six weeks of maturation, a robust vessel wall developed and the AVF could sustain repeated cannulation, allowing regular hemodialysis. The VA should be easy to use, reliable and with minimal risk to the individual receiving hemodialysis. Furthermore, in order to maximize the amount of blood cleansed during hemodialysis and minimize the time of the treatment, the vascular access should allow high volumes of blood flow.

There are currently three main types of VA:

1) The native arteriovenous fistula (AVF), widely described in the next paragraph;
2) The arteriovenous graft (AVG): it consists of the connection of an artery to a vein using a synthetic (usually polytetrafluoroethylene (PTFE)) tube, and it may be the best option in case of small veins. This type of VA is not treated in the present thesis.

3) The central vein catheter (CVC): it is usually a cuffed, double-lumen silicone catheter used in case of AKI or ESRD. Due to its high rate of infection, it should be used with caution, as the last choice of VA, and therefore is not considered in the present thesis.

1.4.1 Arteriovenous fistula (AVF)

A year after the publication of Brescia, Cimino and Appel, the AVF technique was amended to allow successful creation of an end to-end anastamosis between radial artery and cephalic antebrachial vein in the forearm [9]. This technique restricted arterial inflow into the AVF to that delivered by the feeding radial artery and thus led to a high risk of developing steal syndrome. The technique was further refined in 1968 by Rohl, who devised the radial artery-side-to-vein-end anastamosis, with or without ligation of the radial artery distal to the anastomosis, allowing for a more suitable positioning of the AVF with excellent subsequent flows. This technique has become the standard AVF creation procedure, predominately within the upper limbs [10].

A diagrammatic representation of a lower arm AVF is shown in Figure 1.6:

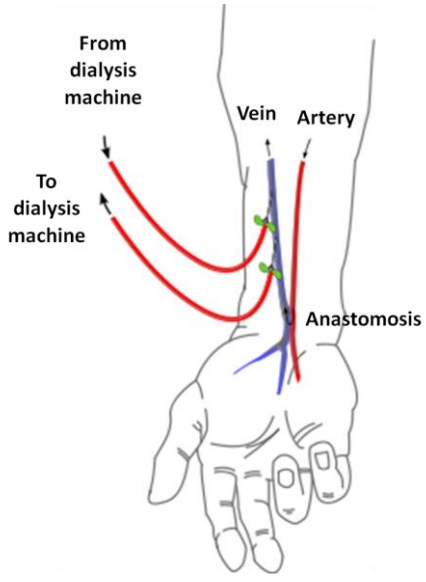

Figure 1.6 Typical radiocephalic AVF with cannulation points for connection to the haemodialysis circuit

The AVF is usually created through the surgical anastomosis of the radial or brachial artery to the cephalic vein. The anastomosis of the artery to the vein offers a bypass of the distal vessels, providing a parallel low-resistance circuit. This leads to a high blood flow rate, which is adequate for an efficient hemodyalisis.

There are three main types of anastomosis, shown in Figure 1.7:

- Side-to-side anastomosis: artery and vein are connected in their longitudinal sense, according to the original Brescia's technique
- Side-to-end anastomosis: connects the end of the vein to the side of the artery through longitudinal arteriotomy;
- End-to-end anastomosis: vein and artery are connected in their transversal sense.

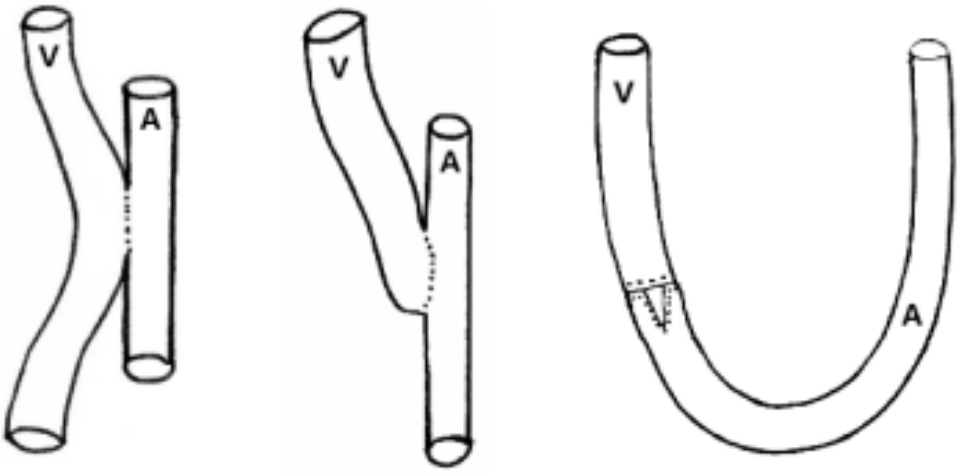

Figure 1.7 Different types of anastomosis. From right to left: side-to-side, side-to-end and end-to-end anastomosis [11]

The side-to-end anastomosis is nowadays the most used, presenting high flow rate and low venous hypertension.

In a newly created AVF the artery and the vein must remodel to accommodate the markedly increased blood flow that results from the arterialization of the vein. The maturation is assumed when vein's diameters is at least 0.6 cm, the flow rate more than 600 mL/min within 6 weeks from the surgery [12].

The main VA-related complications are:

- Early maturation failure: incapacity of providing adequate flow and dilatation, due to anatomic factors such as diameter or intimal thickness of feeding artery and draining vein;
- Stenosis: due to neointimal hyperplasia formation, which causes a significant reduction of blood flow rate and high recirculation;
- Thrombosis: mostly due to intravascular stenosis from anatomical defects arising within venous drainage from the access site although rarely from the arterial inflow.
- Infections due to vascular cannulation;
- Aneurisms: dilatation of the basal part of the arterialized vein.

Nowadays the autogenous AVF is the preferred type of vascular access [13]. It is considered the best option because of its longer survival and lower complication rates as compared with other forms of VA. Large studies showed a graded mortality risk from both cardiovascular and infectious diseases depending on access type, with the highest risk associated with CVC, followed by AVG and then by native AVF [14]. Furthermore, the cost of VA care was more than five-fold lower in those patients who began treatment with functioning native fistulae comparing to those who were treated with grafts or permanent catheters [15]. Therefore, both the KDOQI guidelines of National Kidney Foundation [16] and the European Best Practice guidelines (EBPG) [17] recommend the AVF as first choice VA in hemodialysis.

Patency of the VA remains the Achilles' heel of the hemodialysis treatment in our days. Early AVF failure (defined as inability to use AVF or failure within 3 months of initial use) occur in about 21%, while overall VA patency at 1 year averages 66% and 56% 2 years after surgery, as reported by Caroli et al. [18] in the ARCH clinical study (Figure 1.8).

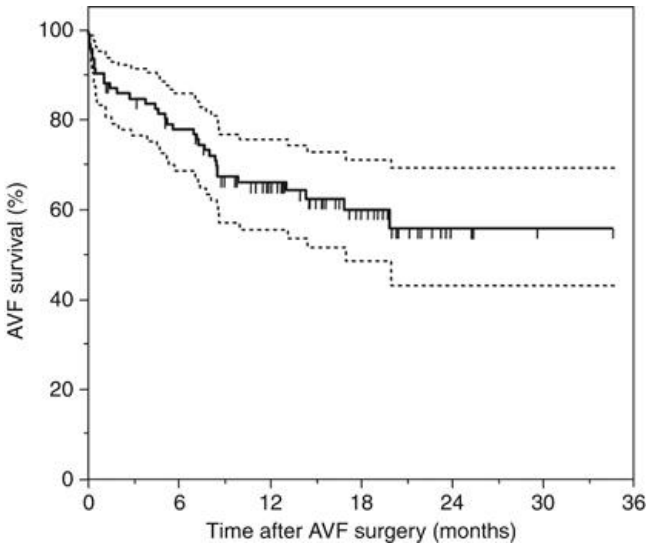

Figure 1.8 VA in the 93 patients with end-stage renal disease and newly created arteriovenous fistula (AVF) enrolled in the ARCH clinical study [18]

Low primary and secondary patency rates, 60% at 1 year and 51% at 2 years for the primary patency rate and 71% at 1 year and 64% at 2 years for the secondary patency, were also reported in a systematic review of 46 articles published between 2000 and 2012 [19].

As maintaining adequate long-term VA for chronic hemodialysis patients needing RRT is one of the most difficult problems vascular surgeons face, it appears evident the importance of studying the causes and factors that lead to fistula failure.

2. Hemodynamics and pathogenesis in the AVF

The present chapter contains the description of the pathogenesis of the AVF failure, caused mainly by the formation of neointimal hyperplasia, which results in stenosis and thrombosis. After the presentation of the role of disturbed flow on the formation of neointimal hyperplasia, a state of the art of AVF patient-specific computational fluid dynamics (CFD) studies will follow.

2.1 Pathogenesis of AVF stenosis

Understanding of vein adaptation and the possible subsequent progressive development of neointimal hyperplasia on the vessel wall may improve the long-term results of AVF patency. Numerous factors, including physical forces, morphologic changes and biochemical events are known to be involved in this process.

2.1.1 Vessel wall biology

The walls of arteries and veins are composed of endothelial cells (EC), smooth muscle cells (SMC) and extracellular matrix, including collagen and elastin. These are arranged into three concentric layers:

- *Tunica intima*: the innermost and thinnest layer, consists of a single layer of endothelial cells lying on a subendothelial connective tissue layer known as the internal elastic lamina, composed of collagen (type IV), laminin and heparin sulfate proteoglycans.
- *Tunica media*: the thickest layer, composed of vascular smooth muscle cells, elastic fibres and extracellular matrix, which vary in amount depending on the type of vessel. It provides mechanical strength to the vascular wall and regulates blood flow through contraction and dilatation, processes controlled by autonomic nerves (nervi vasorum) and local metabolic factors. Elastic fibers allow the vessel to expand with systole and contract with diastole, thereby propelling blood forward. The medial layer is supported by another layer of connective tissue, the external elastic lamina.
- *Tunica adventitia*: the outer layer, consists of a collection of fibroblasts, perivascular nerves and nutrient microvessels embedded in a collagen-rich extracellular matrix (ECM). Recent studies suggest a more dynamic picture of the adventitia that emphasizes critical roles played by interacting adventitial cell types in growth, inflammation, repair, and disease of the artery wall [20].

Arteries and veins have all these layers of tissues in their walls, but the proportions of these layers differ. The tunica media of the arteries contains more SMC than the tunica media of their counterpart, the veins, and this allows the arteries to constrict and dilate to adjust the volume of blood needed by the tissues that they feed and to withstand and absorb the

pressure waves which start from the heart and are transmitted by the blood; the elastic artery layer permits the compliance of the arteries. Figure 2.1 shows the different size of the layers, underlying the presence of a thicker tunica media layer in the arteries, which are characterized by high pressure fields.

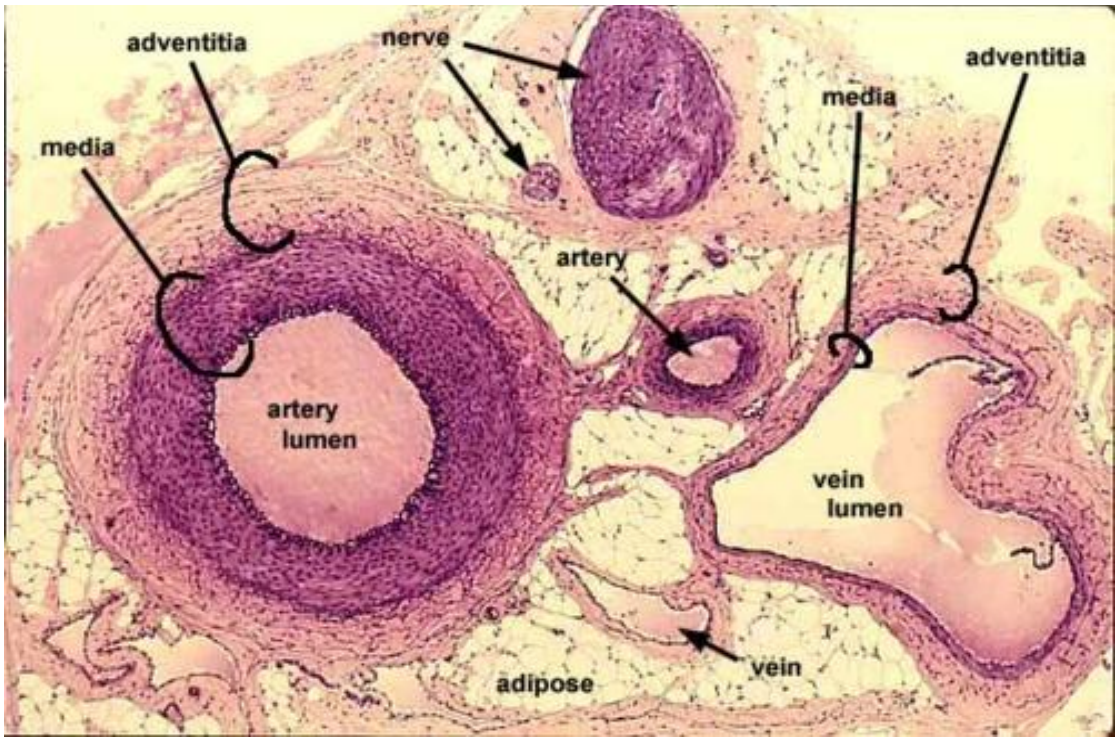

Figure 2.1 Comparison between arterial and venous walls: the main difference is the presence of a thicker tunica media in the artery, while the veins are characterized by a thicker tunica adventitia

2.1.2 Mechanisms of Intimal hyperplasia

Neointimal hyperplasia, the abnormal migration and proliferation of SMC with associated deposition of extracellular matrix in the intimal layer of the vein, is one of the main causes of AVF failure. The phases of upstream events leading to neointimal hyperplasia can be classified into platelet activation and adhesion, leukocyte recruitment and transmigration, and SMC migration and proliferation [21].

As shown in Figure 2.2, the creation of the anastomosis leads to endothelial denudation, particularly at the perianastomotic sides. Besides damage to the endothelium, high arterial pressure and flow cause damage to the media layer of the vein.

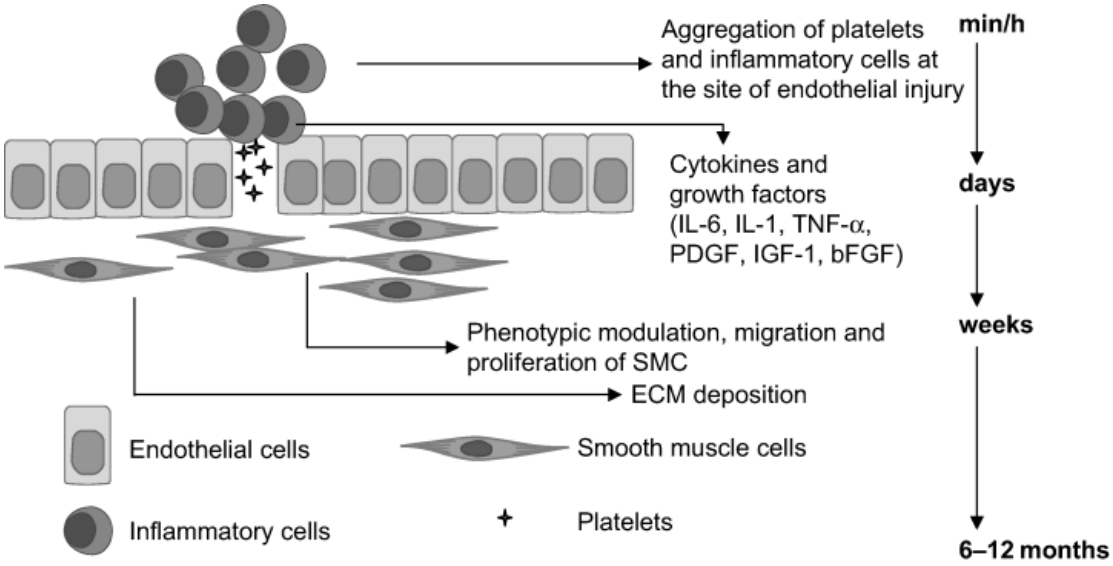

Figure 2.2 Time-course effects and effect of growth factors and cytokines leading to formation of IH-mediated [21]

The endothelium has a central role in the cascade of events. Both dead and injured EC can release inflammatory mediators that trigger platelet aggregation and recruitment of leukocytes to this area. In the activated EC, increased expression of growth factors, such as basic fibroblast growth factor (βFGF), promotes SMC migration from the media to the intima and stimulates the proliferation of EC and SMC [22]. Proliferation of SMC in the intima is associated with deposition of extracellular matrix, resulting in a rapid formation of a neointimal layer over the site of surgical injury. The possibility of adventitial migration of fibroblasts to the media and intima results in that the adventitia may have a key role in neointimal hyperplasia formation, as a source of neointimal precursor cells that contribute to the cellular mass of developing neointimal hyperplasia [23].

It is hypothesized that neointimal hyperplasia serves as a substrate for the development of vein atherosclerosis. Such accelerated form of neointimal hyperplasia increases the chance of vein occlusion.

2.1.3 Stenosis and thrombosis

The main cause of AVF failure is an initial failure to mature followed by venous stenosis. The commonly used parameter to characterize the hemodynamic relevance of a stenosis is a reduction in vessel diameter exceeding 50% based upon a comparison with the adjacent, normal vein. This evaluation is usually conducted using angiographic and/or ultrasonographic techniques. It is unclear the exact pathology and whether the primary factor is venous neointimal hyperplasia, but the characteristic lesion is a juxta-anastomotic stenosis. Several studies have reported venous neointimal hyperplasia before dialysis access surgery [24], [25], caused by factors like ESRD, ageing, obesity, diabetes and cardiovascular disease. Allon et al. [26] did not find any preexisting neonintimal hyperplasia in 50 hemodialysis patients and found severe neointimal hyperplasia in six patients with non-maturing AVF that was not present at the time of the surgery, a strong demonstration that venous neointimal hyperplasia develops *de novo* after AVF creation.

Localization of the stenoses suggests a high correlation with the geometry of the AVF and to the local hemodynamics. The study conducted by Sivansen et al. [27] on side-to-end AVF was aimed to identify stenoses and their locations. They found that stenotic lesions were localized at three specific sites, shown in Figure 2.3: at the anastomosis (Type 1 stenosis), on the curvature of the vein (Type 2 stenosis) and where the vein straightens out (Type 3 stenosis).

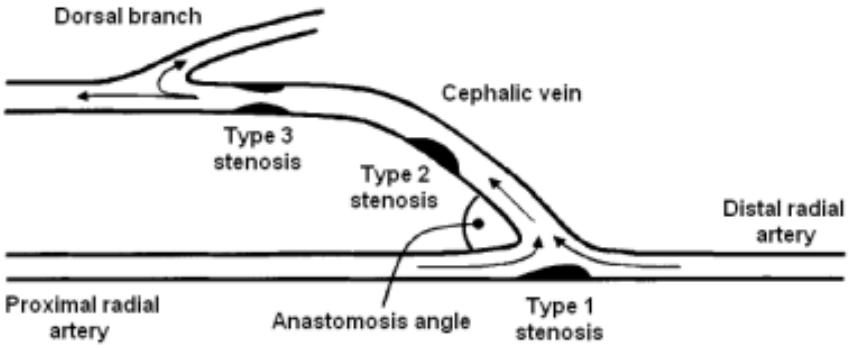

Figure 2.3 Sites of stenoses in a radio-cephalic fistula [27]

Type 1 and type 2 stenoses were not progressive and were probably a direct result of adaptation to altered hemodynamics when the vein is anastomosed to the artery. Type 3 stenoses were generally progressive, eventually encroaching on the venous lumen and limiting blood flow. A study of Asif et al. [28] confirmed the location of the stenosis at the juxta-anastomotic vein, as shown in Figure 2.4.

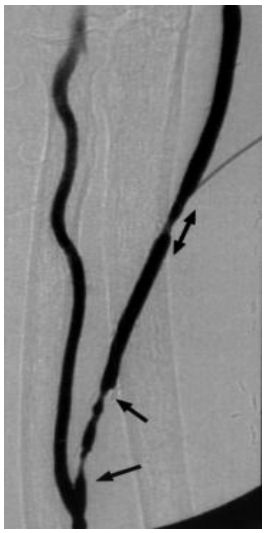

Figure 2.4 Arrows demonstrating juxta-anastomotic lesion in a forearm AVF [28]

Maya & Allon [29] found that approximately 50-60% of stenoses develop at or near the arterial anastomosis of the fistula, whereas the rest occur more proximally in the venous circulation, including up to 20% that involve central veins. In this field, studies of Roy-Chaudhury are of fundamental importance. His research group found that stenoses occur at the swing segment in wrist fistulae (Figure 2.5b) and in the proximal vein in fistulae that are constructed at the elbow (Figure 2.5c) [30].

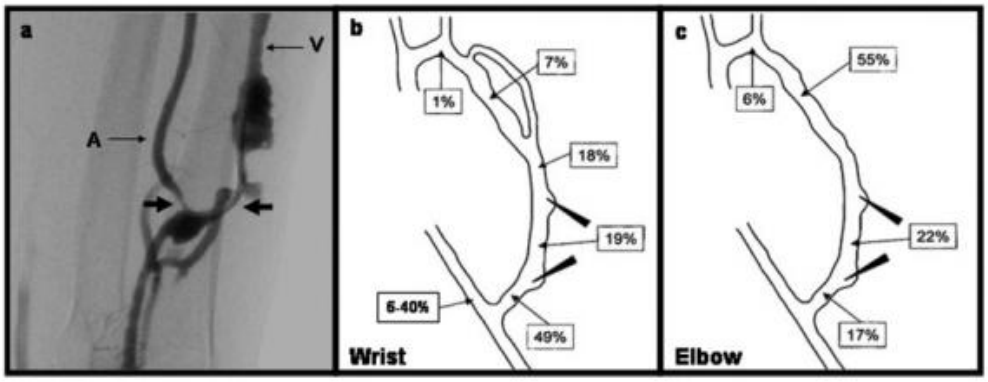

Figure 2.5 (a) A juxta-anastomotic stenosis (shown by arrows), resulting in AVF failure; (b) Sites of venous stenosis of AVF at the wrist; (c) Sites of venous stenosis of AVF at the elbow [30]

With the aim of identifying the specific cell types present within venous tissue samples from patients with stenotic AVFs, they collected tissue segments near the stenotic portions, near the anastomosis [31], shown as regions 2 in Figure 2.6.

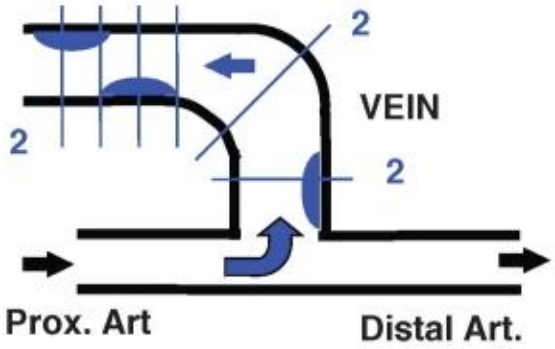

Figure 2.6 Anatomical location of venous neointima within the venous segment that is downstream the arteriovenous anastomosis in AVFs [31]

Histological and immunohistochemical analyses were conducted on the samples: sections were examined with a standard streptavidin biotin immunohistochemical technique for the gene expression to differentiate between contractile medial-like smooth muscle cells, myofibroblasts, fibroblasts and macrophages. Results shown in Figure 2.7 emphasized the role of the myofibroblast as the predominant cell type involved in the pathogenesis of neointimal hyperplasia (similar to the data previously described by them in the context of early AV fistula failure [32]) and draw attention to a possible migration of adventitial fibroblasts from the adventitia to the intima through the venous media.

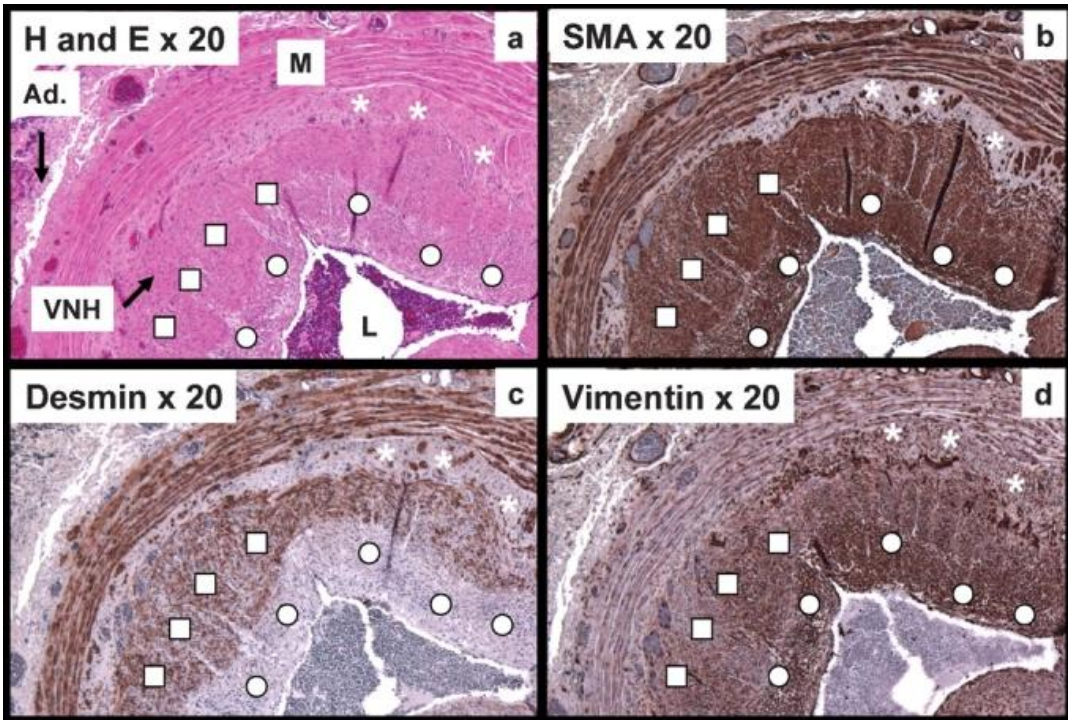

Figura 2.7 Venous neointimal hyperplasia in dialysis access dysfunction; the white asterisks denote a region of fibroblasts, the white circles a region of myofibroblasts and the white squares a region of contractile smooth muscle cells and myofibroblasts. Ad. = adventitia, M = media, VNH = venous neointimal hyperplasia [31].

In AVF, significant stenoses may not elevate dynamic or static pressures, although such lesions can result in decreased access flow and elevated recirculation, that are associated with increased risk for thrombosis [33]. In most patients, thrombosis is the final complication after a period of AVF dysfunction and requires a prompt intervention, as the risk of delay is progressive growth of the thrombus that makes interventional procedures more difficult and risky with regard to long-term patency. Periodic monitoring and surveillance of the AVF can help in identifying narrowings before they cause thrombosis and may help to improve long-term AVF survival.

2.2 Hemodynamics in the AVF

Several published findings support an important role of blood flow dynamics in AVF maturation or non-maturation [34]. In fact, it is known that in AVF the stenoses occur in specific sites, consistently related to the local hemodynamics determined by the vessel geometry and the blood flow pattern. As the locations of these sites seem to match the areas of disturbed flow, it is important to study how the hemodynamic stimuli and the flow patterns may influence the pathogenesis of neointimal hyperplasia in the venous side of vascular access after the creation of the anastomosis.

2.2.1 Hemodynamic stimuli

Blood vessels are capable of continuous adaptive structural change (remodeling) in response to modification of two parameters: wall shear stress and circumferential shear stress. Blood moving along vessel wall incurs a shear stress on the wall, the Wall Shear Stress (WSS or τ), given by the following definition:

$$\tau = -\mu \cdot \gamma'$$

where μ is blood dynamic viscosity of the patient and γ' is the shear rate.

In case of ideal cylindrical vessel and steady flow τ can be calculated with Poiseuille's equation:

$$\tau = \frac{32\mu Q}{\pi D^3}$$

where Q is blood volumetric flow rate, μ is blood viscosity and D is the diameter of the vessel.

The transmural pressure, the pressure drop between internal and external sides of the wall of the vessel, causes a circumferential shear stress (σ) that can be calculated using Laplace equation:

$$\sigma = \frac{\Delta P \cdot D}{2s}$$

where ΔP is the transmural pressure and s is the wall thickness.

Two feedback loops control the vessel wall remodeling, as shown in Figure 2.8. Increased blood flow increases τ, eliciting an increase in vessel diameter, which returns τ to its initial level. Increased transmural pressure increases σ, leading to augmentation of wall mass and wall thickness and acts on σ, trying to return it at its initial level [35].

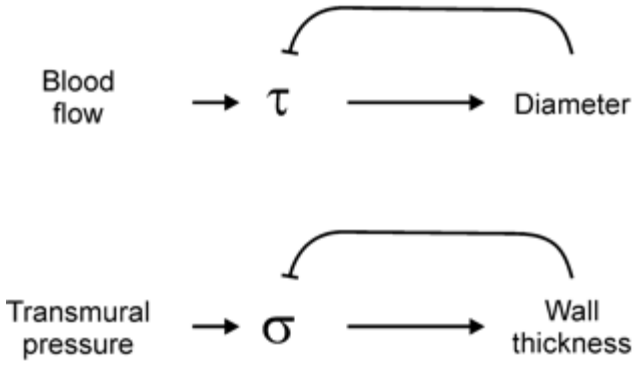

Figure 2.8 Negative feedback loops controlling vessel wall remodeling [35]

2.2.2 The role of hemodynamics in AVF remodeling and adaptation

The surgical creation of AVF produces several hemodynamic changes: both venous dilatation and flow volume increases are crucial factors to obtain a functioning AVF. Furthermore, the geometry of the anastomosis imposes rapid changes in the direction of blood flow. To summarize, there are two events occurring after fistula creation, triggered by the hemodynamic stimuli:

- a dramatic rise in the flow rate, leading to the dilatation of the vessel in order to keep WSS within a narrow, so called "physiological range" [36]. In fact the increase in the blood flow rate increases τ on EC that produce mediators of vascular cells proliferation and matrix deposition, resulting in enlargement of the vessel lumen and a consequent reduction of WSS to the physiologic range;
- an increased muscular thickness in the wall, which is a process referred to as vein arterialization, as a result of the increase in circumferential stress [37].

Vascular remodeling in the AVF aims to accommodate blood vessels at the new hemodynamic condition and restore the basal levels of σ and τ.

2.2.3 The response of endothelium to shear forces: disturbed vs. laminar flow

The mechanisms of remodeling and adaptation previously described can not act in specific regions of the vasculature, like branches and curvatures, as well as in some regions of AVF, where disturbed flow may develop. The pattern of disturbed flow is irregular and

features secondary and recirculation eddies that may change in direction with time and space, which results in low and reciprocating WSS on the EC [38]. It has been observed that disturbed flow acting on EC *in vitro* induces selective expression of pro-oxidant, proinflammatory, procoagulant and proapoptotic genes. A study of Dai et al. [39] defined two prototypic arterial waveforms, "athero-prone" and "athero-protective" (Figure 2.9), representative of the WSS in two distinct regions of the carotid artery (carotid sinus and distal internal carotid artery), that are typically "susceptible" or "resistant," respectively, to atherosclerotic lesion development. It can be observed that WSS values of the "athero-prone" waveform are low and oscillating in the range -10/+5 dynes/cm^2.

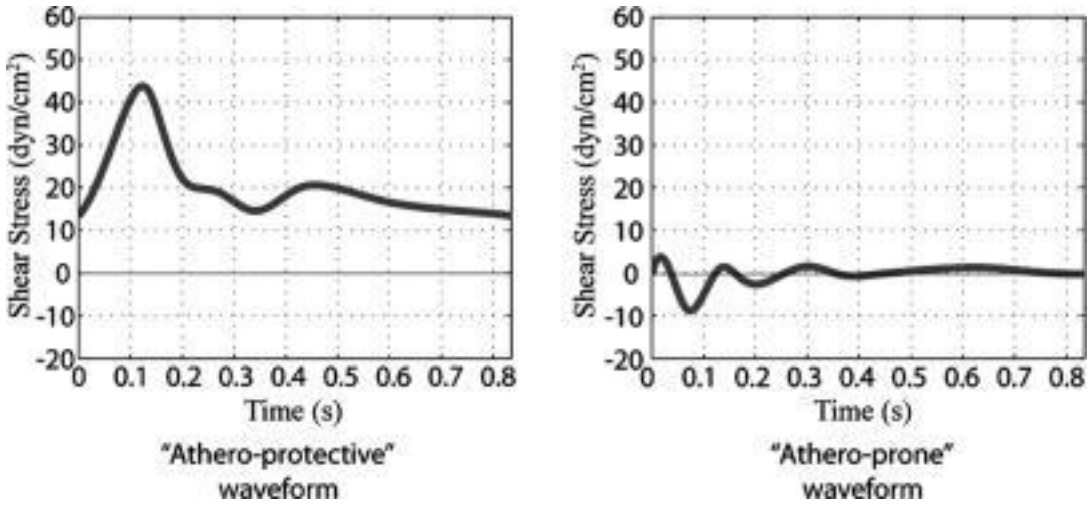

Figure 2.9 Prototypic athero-prone and athero-protective waveforms [39]

These two waveforms were applied to cultured EC modified cone and plate device with a computer-controlled user interface [40], [41] and then the differential patterns of EC gene expression analyzed. Analysis of transcriptional profiles showed that athero-prone and athero-protective waveforms induce distinct patterns of gene expression, revealing a proinflammatory phenotype in case of athero-prone waveform, expressing several important chemokine/chemokine receptors. Furthermore, EC displayed dramatic differences in cell shape and alignment under athero-prone and athero-protective waveforms, shown in Figure 2.10.

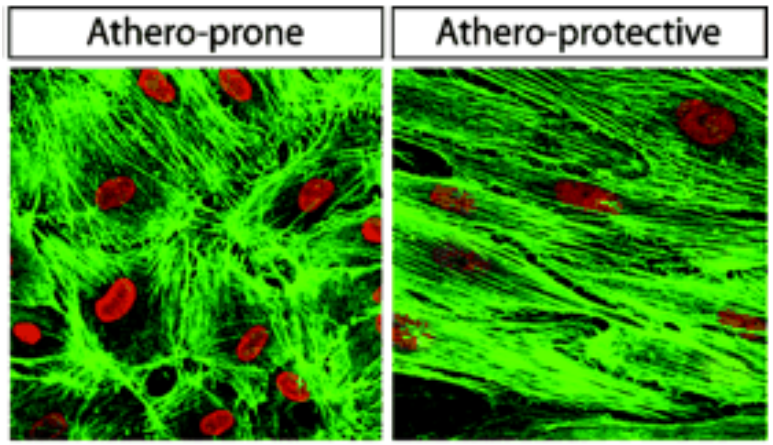

Figura 2.10 Differences in cell shape and alignment under different waveforms [39]

These data strongly implicate the modulation of endothelial phenotype by biomechanical stimuli and result in a strong linkage between these stimuli and sites of neointimal hyperplasia and atherosclerotic lesion development, summarized in Figure 2.11.

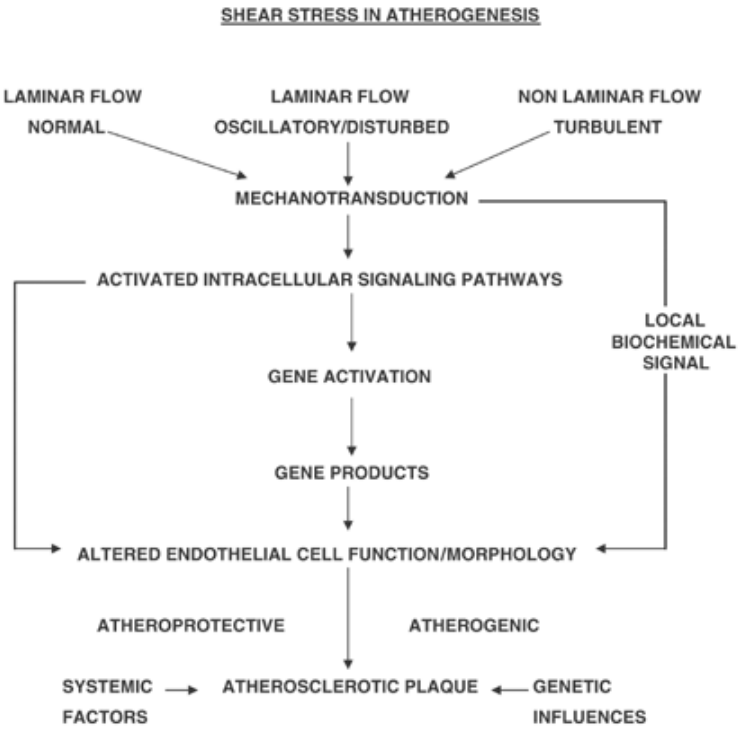

Figure 2.11 Scheme of the activation of atheroprone and atheroprotective responses [42]

Furthermore, it has been shown that low or near-zero shear stress itself also promotes neointimal formation *in vivo*, as demonstrated by Morinaga et al. [43] on autogenous vein grafs of dogs and recently by Krishnamoorthy et al. [44] in a pig model of AVF.

In contrast to disturbed flow, sustained laminar flow within a physiological range and a predominant direction activates signaling pathways that induce expression of several atheroprotective and antithrombogenic genes and endothelial nitric oxide synthase with a protective effect on EC [45].

2.4 State of the art of CFD simulations in AVF

2.4.1 CFD studies on AVF models

The WSS at the AVF anastomosis was investigated in several CFD studies in the last decade. Using CFD, Krueger et al. [46] characterized the local hemodynamics, and in particular the WSS, in conventional side-to-end AVF and patch form anastomosis (Venaflo). Kharboutly et al. [47],[48] reconstructed a patient specific AVF from computed tomography angiography. An accurate map of unsteady velocity profiles and WSS was drawn up. In contrast with other authors, they did not observe any association between calcification and areas of oscillating WSS, but suggested a potential association between calcification and high temporal WSS gradients. Ene Iordache et al. [49] found areas of the vessel wall with very high WSS gradients on a patient specific end-to-end AVF, on the bending zone of the radial artery and on the venous side, after the anastomosis. Secondary blood flows were also observed in these regions. Carroll et al. [50] reconstructed a 3D geometry of a healthy vein and a fully matured patient-specific AVF from a series of 2D MRI scans. Complex flow patterns were observed and the maximum and mean WSS magnitudes are significantly elevated respect to the contralateral arm vein. Flow reversal was found within the juxta-anastomotic vein and the efferent vein. All of these studies found high WSS values at the anastomosis, but did not find disturbed flow patterns on the AVF walls.

In 2012 Ene-Iordache et al. [51] performed numerical simulations of blood flow inside idealized models of AVF aimed at characterizing the patterns of haemodynamic shear stress: they found areas of low and oscillating WSS on the juxta-anastomotic vein in either side-to-end or end-to-end AVF models, as shown in Figure 2.12.

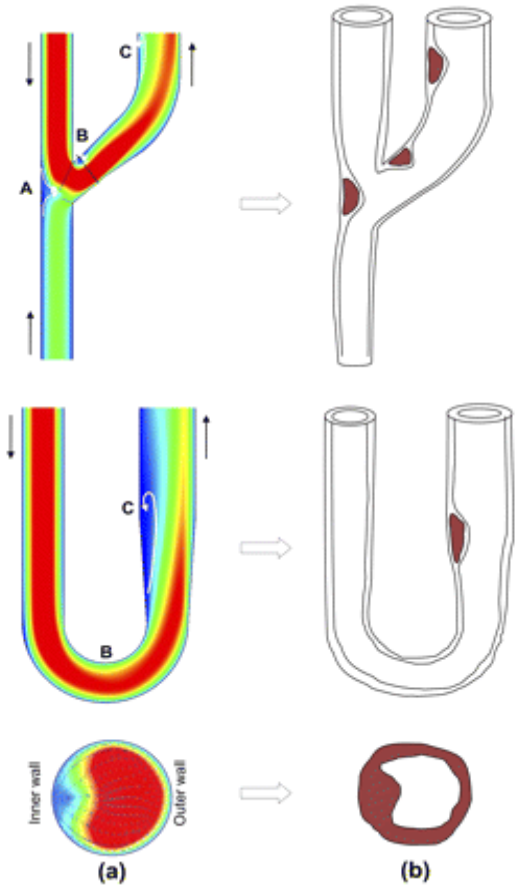

Figure 2.12 Representation of zones of low and oscillating shear stresses that trigger formation of neointima [51]

Based on such findings, they further studied the influence of the anastomosis angle on the pattern of disturbed flow showing that the smaller the angle, the smaller is the area of low and oscillating WSS [52]. Following this research line, evaluations in side-to-end patient-specific models conducted by Semperboni [53] suggested that anastomosis angle, curvature, planarity and local changes in sectional area can strongly influence the fluidynamics of the AVF. These image-based CFD studies reported velocity streamlines for the peak systolic blood flow for two patients AVF, as shown in Figure 2.13. They

revealed laminar flow in the proximal artery and secondary flow and local vortexes in the venous segment, confirming the results obtained with idealized models.

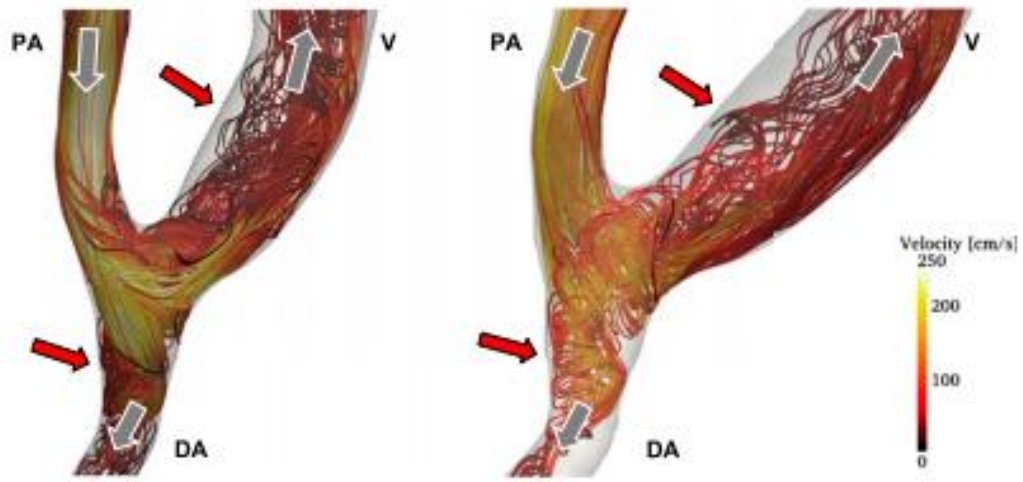

Figure 2.13 Blood velocity streamlines inside two patient-specific AVFs [56]

Such CFD results and the use of the computational tool pyNS in planning the VA surgery [54], [55] in patients starting hemodialysis treatment were the foundation of a recent review by Remuzzi & Ene-Iordache [56] on the hemodynamics role as an upstream event in the ignition and formation of neointimal hyperplasia in VA.

2.5 Aim of the present study

Despite clinical and technological advancements, the VA still has significant early failure rates, mainly due to neointimal hyperplasia related to the hemodynamic conditions.

As shown above, a number of studies have found disturbed flow patterns on the juxta-anastomotic vein, either in idealized or patient specific models.

The present thesis was aimed at investigating and characterizing more in detail the nature of flow instability, with special attention to the transition from laminar to turbulence in patient-specific AVF.

The secondary aim was also to compare the flow pattern observed in the AVF model with the flow pattern of a normal carotid bifurcation, anatomical district characterized by a complex geometry similar to the AVF's and by high flow rate.

3. 3D reconstruction of AVF models

The present chapter contains guidelines to perform 3D reconstruction of patient specific models starting from MRA images. The first part includes a detailed description of the methodology used to reconstruct the AVF models and subsequent mesh generation. The second part covers the results of 3D reconstruction presenting the models chosen for the CFD simulations.

3.1 3D patient specific models reconstruction from MRA images

For the present work six models of side-to-end AVF have been reconstructed: three radio-cephalic and three brachio-cephalic models. Images of the patients used for the reconstruction were stored in the study database for the European project ARCH, a joint initiative of four medical centers (including Mario Negri Institute) and three industrial partners. The main objective of the study was the collection of structural and functional informations for development and validation of patient specific image-based computational modeling tools for surgical planning and assistance in the management of complications arising from VA creation in patients requiring chronic hemodialysis treatment. Images available in the database have been acquired using contrast-enhanced (CE-MRA), the standard reference for non-invasive vascular imaging due to the high-resolution of this technique. Figure 3.1 shows an example of an acquisition: the image on the left contains almost the whole thorax, the image on the right shows a zoom on the district of interest. All the images used for the reconstruction have been collected 40 days after the surgery, in order to wait for the vascular adaptation and the maturation of the AVF.

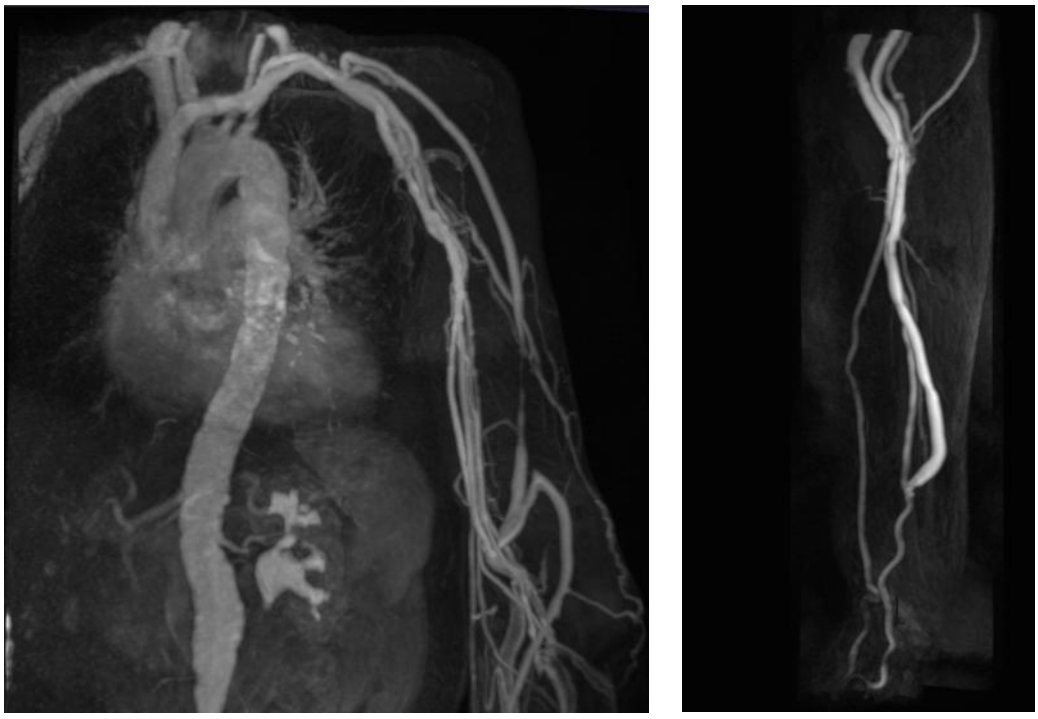

Figure 3.1 Example of images acquired with CE-MRA

3.1.1 Reading DICOM and selecting a Volume of Interest (VOI)

3D models reconstruction has been realized with the Vascular Modeling Toolkit (*vmtk*) [57], a collection of libraries and tools for 3D reconstruction, geometric analysis, mesh generation and surface data analysis for image-based modeling of blood vessels. Vmtk is an open-source software realized by Luca Antiga, composed of C++ classes (VTK and ITK -based algorithms), Python classes and PypeS (Python pipeable scripts, a framework which enables *vmtk* scripts to interact with each other).

The clinical images available in DICOM format can be read using the command:

```
vmtkimagereader -f dicom -d dicom_directory_path --pipe vmtkimageviewer
```

where dicom_directory_path is the folder where DICOM images are stored.
The command imagereader can not only allow to read the image, but also to reorient the image volume correctly based on its orientation relative to the patient. The command vmtkimageviewer lets to visualize images and once the view pops up, it is possible to:

- rotate the volume
- translate the volume
- zoom the volume
- probe the image planes (coordinates and gray-levels)
- move the image planes

Once the position of the fistula has been identified, the format of the images has to be converted in **`*.mha`** format (Meta Image), extracting also a volume of interest (VOI) containing the AVF. To extract a VOI an instance of **vmtkimagevoiselector** between the DICOM reader and the writer can be placed:

```
vmtkimagereader -f dicom -d dicom_directory_path --pipe vmtkimagevoiselector -ofile image_volume_voi.mha
```

The command **vmtkimagevoiselector** makes a render window pop up and a yellowish cube is the tool used to select the VOI (Figure 3.2):

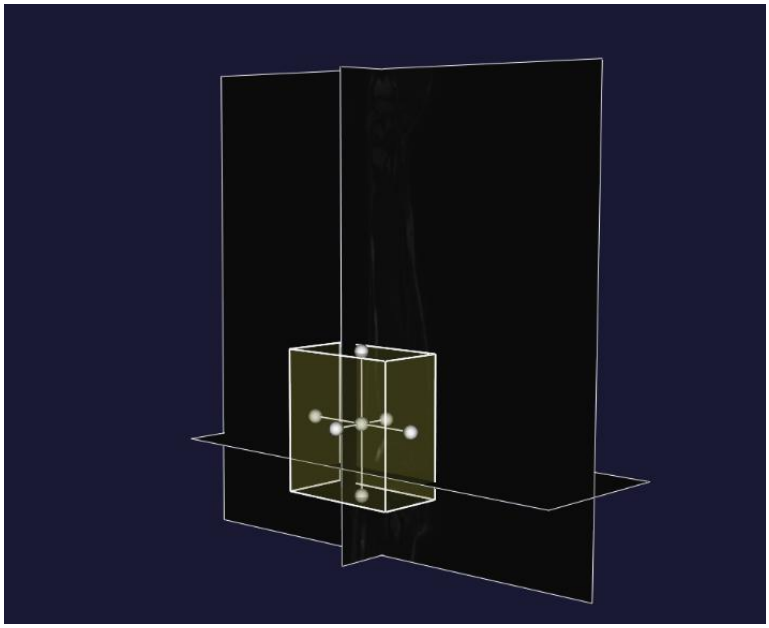

Figure 3.2 Extraction of the Volume of Interest

Translating, rotating and resizing the cube, as well as changing gray window-levels to better visualize the AVF, are the interactions permitted. They allow to select the VOI as the volume contained inside the cube and visualize it in the render window. An example of VOI is shown in Figure 3.3:

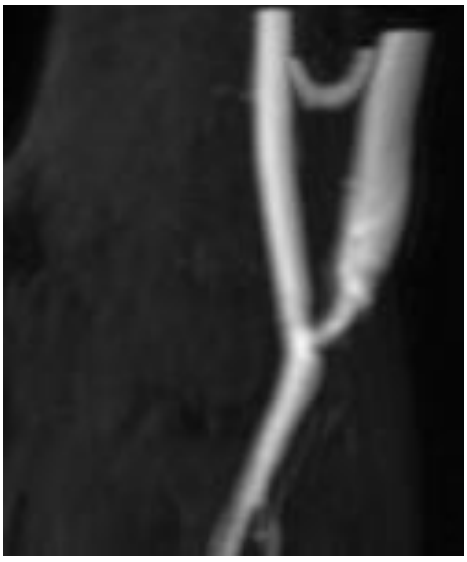

Figure 3.3 Result of the VOI extraction

3.1.2 Level set segmentation

Level sets [58] are a kind of deformable model in which the deformable surface is not represented by a set of points and triangles, but rather described by a 3D function (basically another image) whose contour at level zero is the surface in question. The advantage of using a deformable model is that the location of the surface does not depend on the chosen level, but on the regions corresponding to the steepest change of image intensity across the vessel wall, which is a robust and objective criterion.

In order to perform level sets in *vmtk* the following command has to be used:

`vmtklevelsetsegmentation` -ifile image_volume_voi.mha -ofile `levelset.mha`

This command lets the user choose the way in which the deformable model is initialized, maintaining the goal to initialize the model as close to the vessel wall as possible.

The options presented by the software are:

- *Colliding Fronts:* it consists of placing two seeds on the image which act as sources of wave fronts. Two fronts propagate from the seeds (one front from each) with their speeds proportional to the image intensity and the region where the two fronts collide is then the initial deformable model. This type of initialization is very effective when it is necessary to initialize the tract of a vessel, with the important advantage that side branches can be ignored.
- *Fast Marching:* it consists of placing a set of seeds and a set of targets on the image. A front is then propagated from the seeds until the first target is met at which point the region covered by the front is the initial deformable model.
- *Threshold:* in this option pixels comprised within two specified thresholds are selected as the initial level sets.
- *Isosurface:* in this option initial level sets correspond to an isosurface of the image with sub-pixel precision.

For this work it has been decided to use the Colliding Fronts method (Figure 3.4), because of its effectiveness in initializing the tract of a vessel.

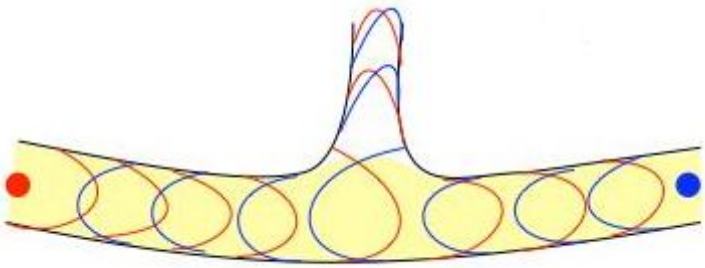

Figure 3.4 Colliding fronts method: the two seeds act as sources of wave fronts

Once Colliding Fronts have been selected, wave propagation can be restricted to a set of intensity levels above a lower threshold and below an upper threshold. Regarding the choice of the two thresholds, the image intensity that appears on the render window placing the mouse on the vessel's boundary is set as the lower threshold, instead the upper threshold can be omitted, selecting automatically all the values higher than lower threshold.

By interacting with the image planes it is possible to find the image planes where to place the two seeds. Then a translucent surface appears in the render window between the two seeds which is the initial deformable model. This procedure is used until the segmentations of all vessels the user is interested in has been completed.

In order to control the level sets some parameters has to be set:

- *Number of iterations*: the number of deformation steps the model performs;
- *Propagation scaling*: the weight assigned to model inflation;
- *Curvature scaling***:** the weight assigned to model surface regularization;
- *Advection scaling*: the weight that regulates the attraction of the surface of the image gradient modulus ridges.

In all the reconstructed models the parameters set are respectively 300 0 0 1. Setting advection to 1 and propagation and curvature to 0 can robustly lead to reproducible results

and setting the number of iterations at 300 should make the level set not to move anymore. At this point the render window shows the merged result and a file named **`level_sets.mha`**, which contains an image is generated. Figure 3.5 shows an example of segmentations with level sets:

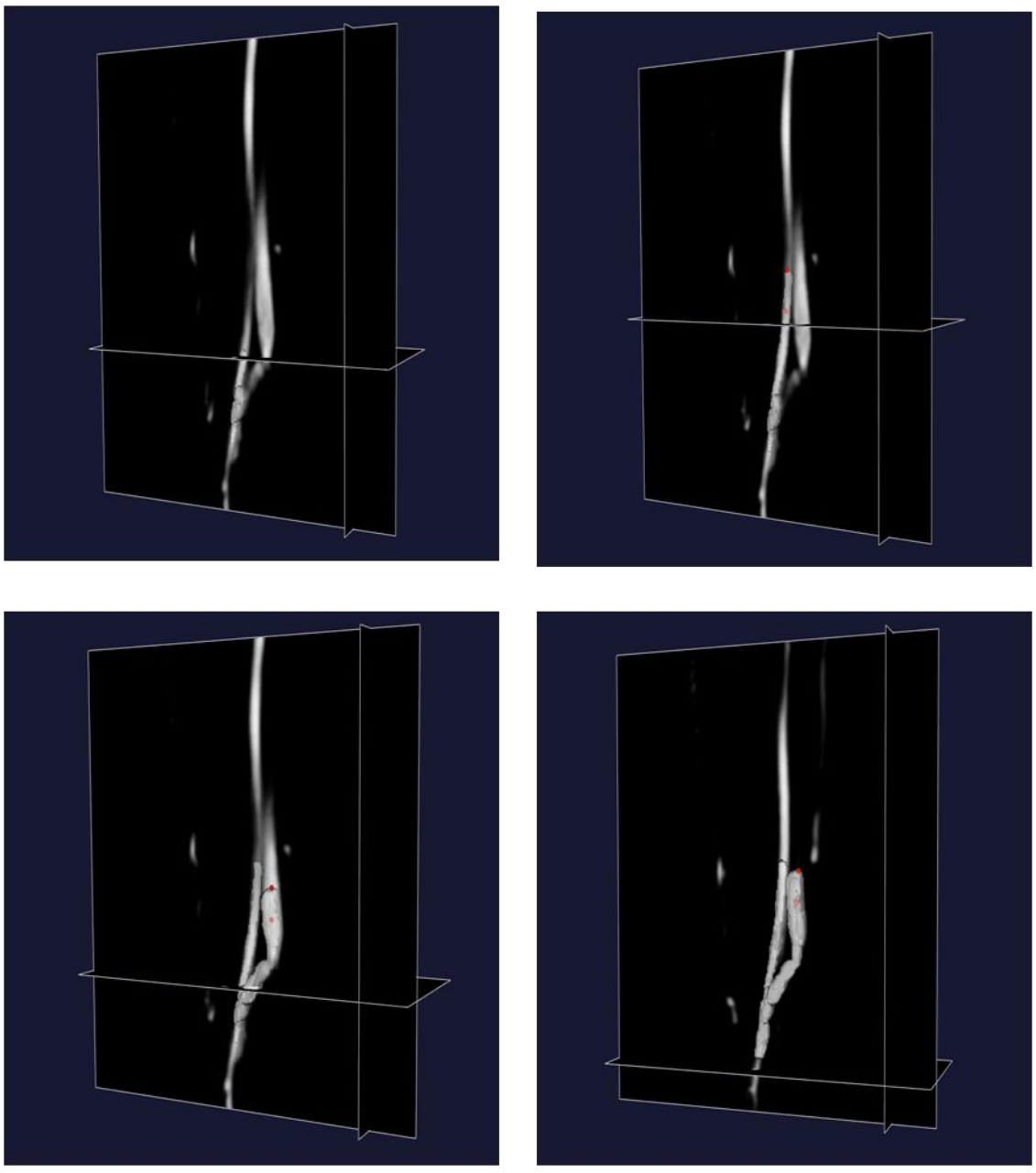

Figure 3.5 Segmentation of a radio-cephalic fistula with level sets

3.1.3 Generating the vessel wall surface with marching cubes

Once the file **`levelset.mha`**, containing the segmented image, has been obtained, a polygonal surface can be extract from it with the following command:

`vmtkmarchingcubes` -ifile levelset.mha -ofile `surface.vtp`

The algorithm marching cubes [59] uses a "divide-and-conquer" approach to generate inter-slice connectivity and then creates a topology surface based on triangles.
Figure 3.6 shows an example surface extracted with marching cubes:

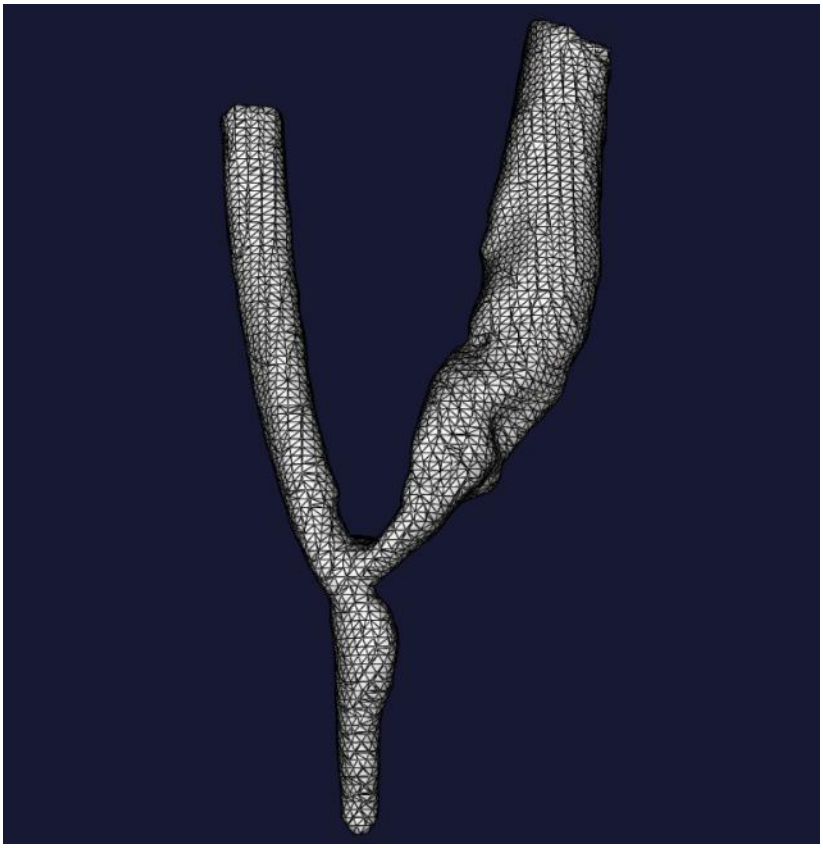

Figura 3.6 Surface extracted using marching cubes

3.1.4 Surface smoothing and adding flow extensions

Image segmentation can result in bumpy surfaces, especially if the image quality is rather poor. Since a bumpy surface can result in spurious flow features and affect wall shear stress distributions, it is important to smooth the surface prior to generating the mesh.

The command used to smooth the surface is:

```
vmtksurfacekiteremoval -ifile surface.vtp --pipe vmtksurfacesmoothing -method taubin -iterations 30 -passband 0.01 -ofile surface_smoothed.vtp
```

The artifacts derived from the segmentation can be removed using the script **vmtksurfacekiteremoval** and the smoothing can be performed with **vmtksurfacesmoothing**. The parameters that have to be set are the method (Taubin is better than Laplacian method because avoids the loss of geometrical features), the number of iterations (after making some attempts, the number of iterations considered the most precise was 30), and the passband (set to 0.01).
A comparison between the surface before and after the smoothing is shown in Figure 3.7:

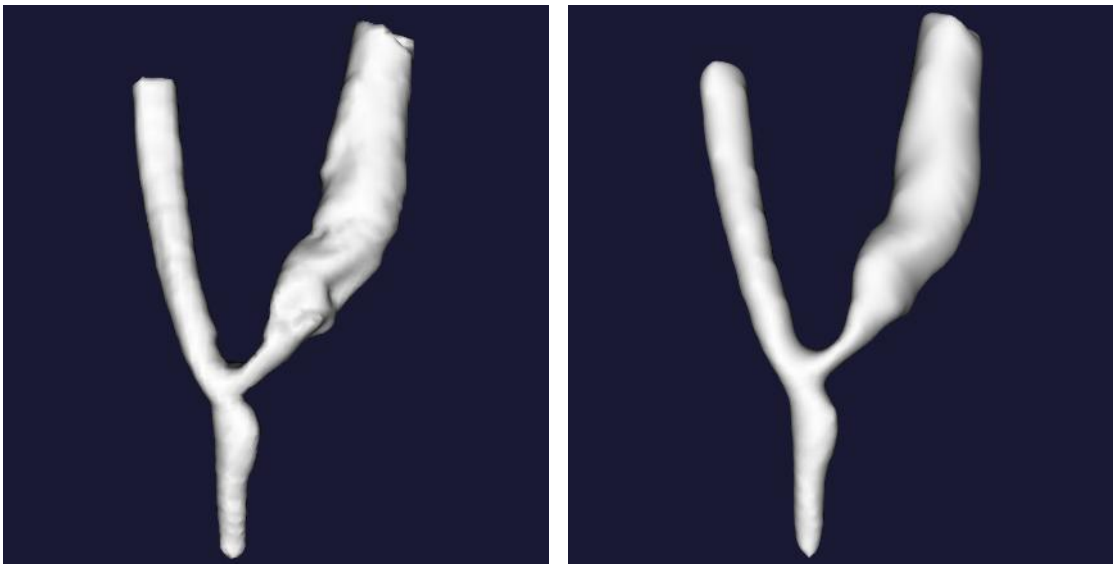

Figure 3.7 Comparison between the surface before and after the smoothing

As the surface has been generated using a deformable model, it is likely that is closed at inlets and outlets, with a blobby appearance. To proceed by opening the surface by clipping the blobby endcaps, the following command can be used:

```
vmtkreader -ifile surface_smoothed.vtp --pipe vmtkcenterlines -
vmtkendpointextractor –pipe vmtkbranchclipper -interactive 1 -ofile
surface_clipped.vtp
```

Endcaps clipping can be performed using **vmtkendpointextractor**, which needs centerlines to be computed before with **vmtkcenterlines**. Centerlines are determined as the paths that minimize the integral of the radius of maximal inscribed spheres along the path, which is equivalent to finding the shortest paths in the radius metric. Briefly, this is done is by propagating a wave from a source point (one endpoint of the centerline) using the inverse of the radius as the wave speed and recording the wave arrival time on all the point; then the line is traced from a target point (the other endpoint of the centerline) down along the gradient of arrival times. Each point of a centerline is associated with a corresponding maximal inscribed sphere radius.
Figure 3.8 shows the surface before and after clipping:

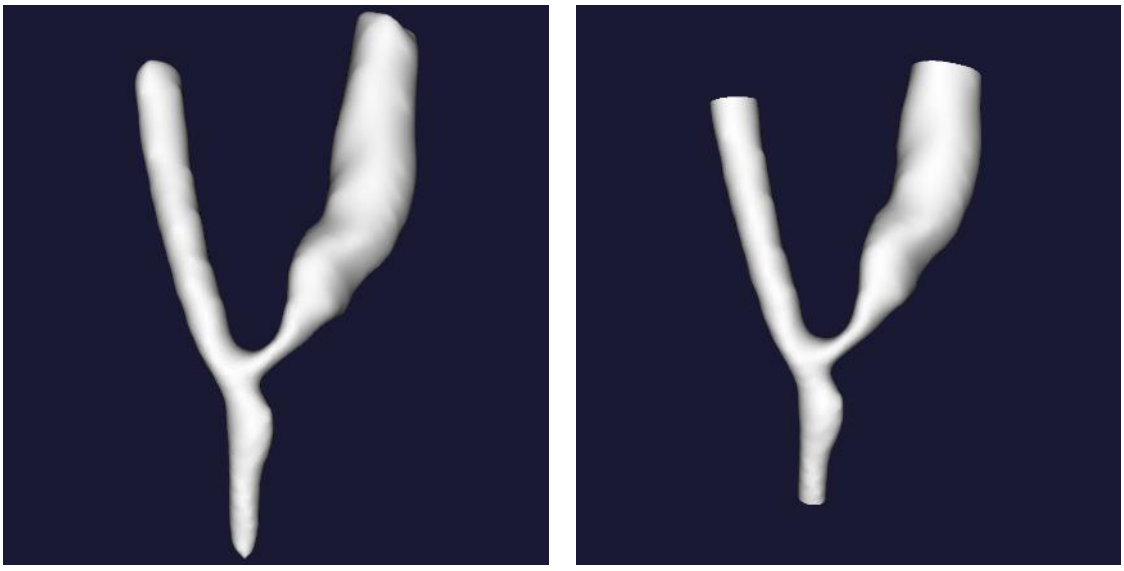

Figure 3.8 Comparison between the surface before and after clipping

Flow extensions are cylindrical extensions added to the inlets and outlets of a model to ensure fully development of flow. An automatic procedure, relying again on centerlines, can preserve reproducibility and speeding up the modeling phase considerably. This time centerlines can use open inlet and outlet profiles for the definition of seed and targets.
The command used for adding flow extensions is:

vmtksurfacereader -ifile surface_clipped.vtp --pipe vmtkcenterlines -seedselector openprofiles --pipe vmtkflowextensions -adaptivelength 1 -extensionratio 10 -ofile surface_ext.vtp

The parameters that have to be set are:
- *Adaptivelength*: a boolean flag which enables computing the length of each flowextension proportional to the mean profile radius;
- *Extensionratio*: the proportionality factor (setting the value 5 means obtaining flow extensions which are 5 times the radius);
Figure 3.9 shows a surface with flow extensions compared to the surface before the addition:

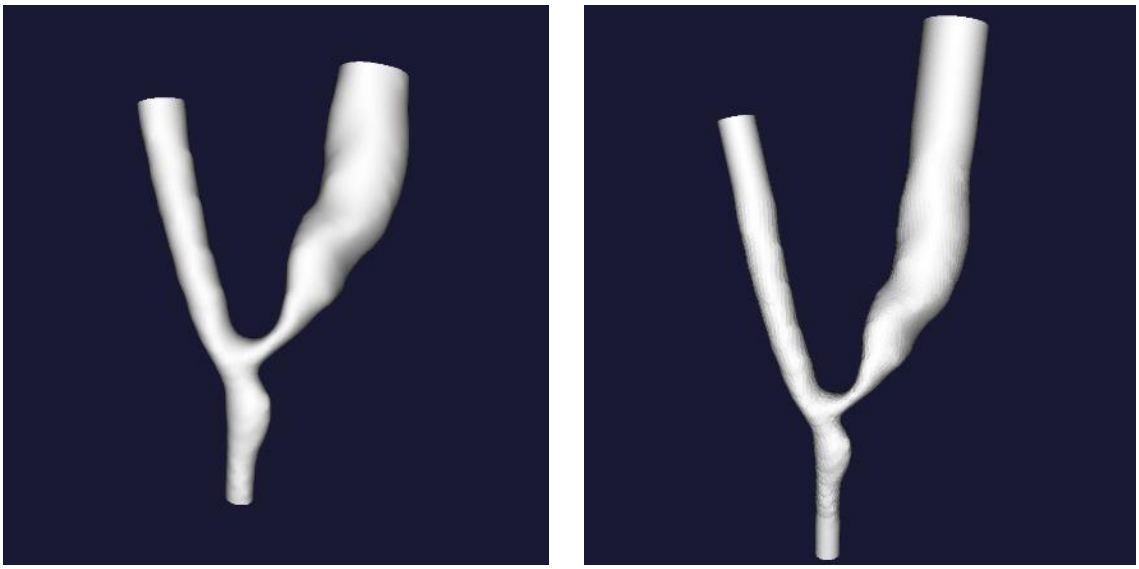

Figure 3.9 Comparison between the surface before and after the adding of flow extensions

3.1.5 Mesh generation

The mesh generator for *vmtk* works by performing two fundamental steps: surface remeshing and volume meshing. In the surface remeshing step the surface triangle edges are resized according to two alternative methods decided by the user: assigning a target edge length uniformly to the whole surface or adopting a scalar sizing function (usually the distance of the surface points from the centerline) to resize the triangles. In the volume meshing step the volume is filled with a combination of tetrahedral and prismatic elements. Some parameters can be used to control the size of the tetrahedral mesh and to create and control the thickness of the boundary layer that let to heighten the density of the mesh near the wall.

The command used to generate all the meshes of this work is the following:

vmtksurfacereader -ifile surface_ext.vtp --pipe vmtkcenterlines -endpoints 1 -seedselector openprofiles --pipe vmtkdistancetocenterlines -useradius 1 -centerlineradius 1 --pipe vmtkmeshgenerator -elementsizemode edgelengtharray -edgelengtharray DistanceToCenterlines -edgelengthfactor 0.2 -boundarylayer 1 -sublayers 4 -boundarylayeroncaps 0 -sublayerratio 0.7 -thicknessfactor 0.2 -ofile mesh.vtu

According to the choice of a radius-adaptive mesh, **vmtkmeshgenerator** has the input DistanceToCenterlines, the distances to the surface of the vessel. The **edgelengthfactor** specifies a proportionality of the length of the surface triangle edges (setting a value of 0.2 a mesh of about one million of element is usually obtained).

An example of surface obtained using the previous command is shown in Figure 3.10:

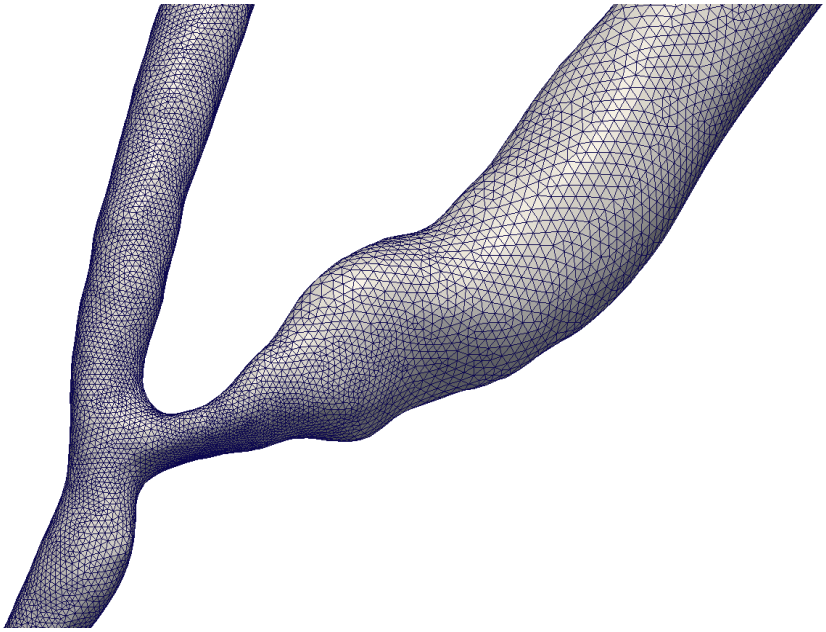

Figure 3.10 Radius-adaptive surface mesh

Regarding the boundary layer, using the sublayers parameter it is possible to choose how many sublayers to create and using sublayerratio parameter it is possible to set the ratio between one layer and its neighbor. For this work, it has been decided to use a boundary layer with four sublayers, as shown in Figure 3.11.

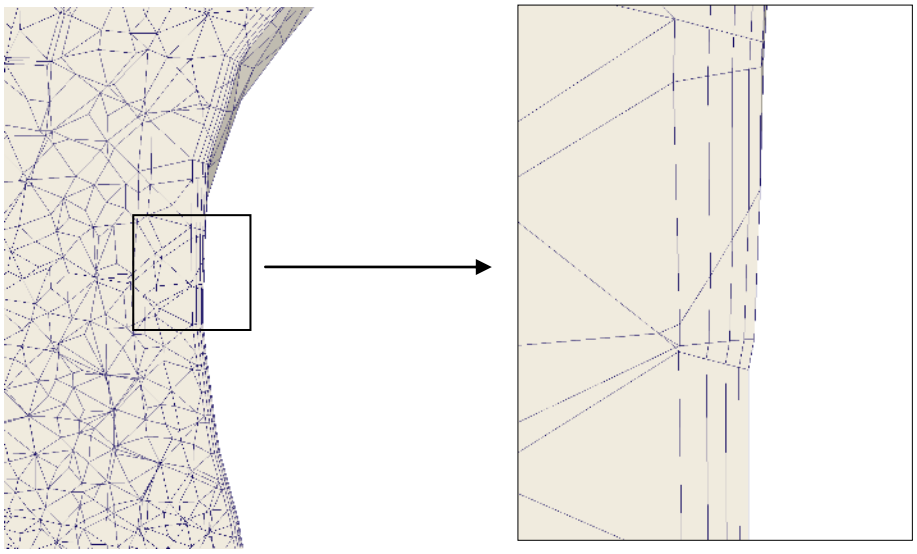

Figure 3.11 Boundary layers and sublayers

3.2 AVFs models

By using the *vmtk* it was possible to reconstruct patient specific side-to-end brachio-cephalic and radio-cephalic models shown in Figure 3.12 and Figure 3.13. Proximal artery, distal artery and vein have been named with the initials PA, DA and V respectively.

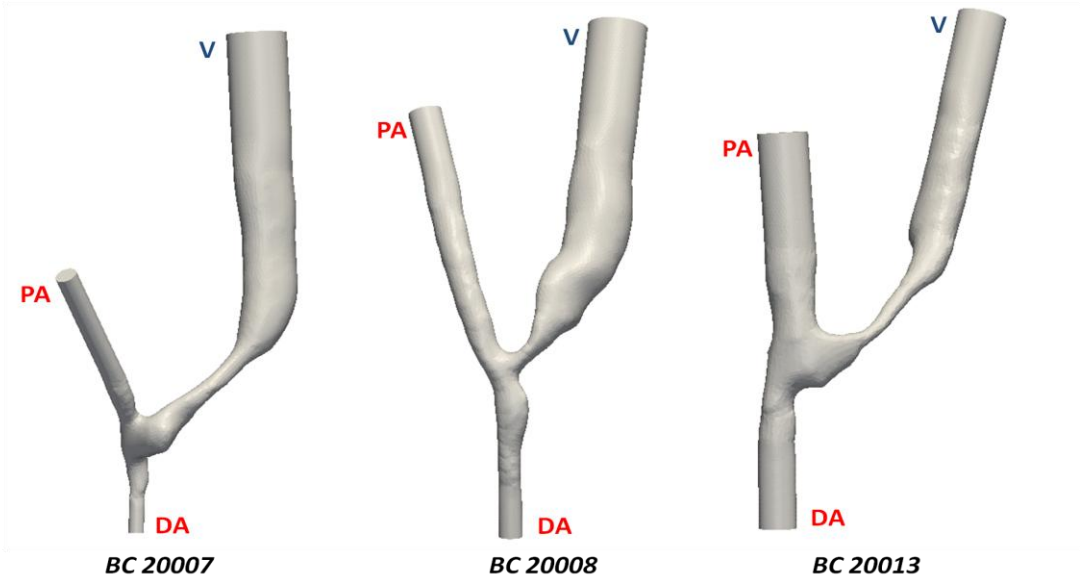

Figure 3.12 Models of brachio-cephalic AVF reconstructed from CE-MRA

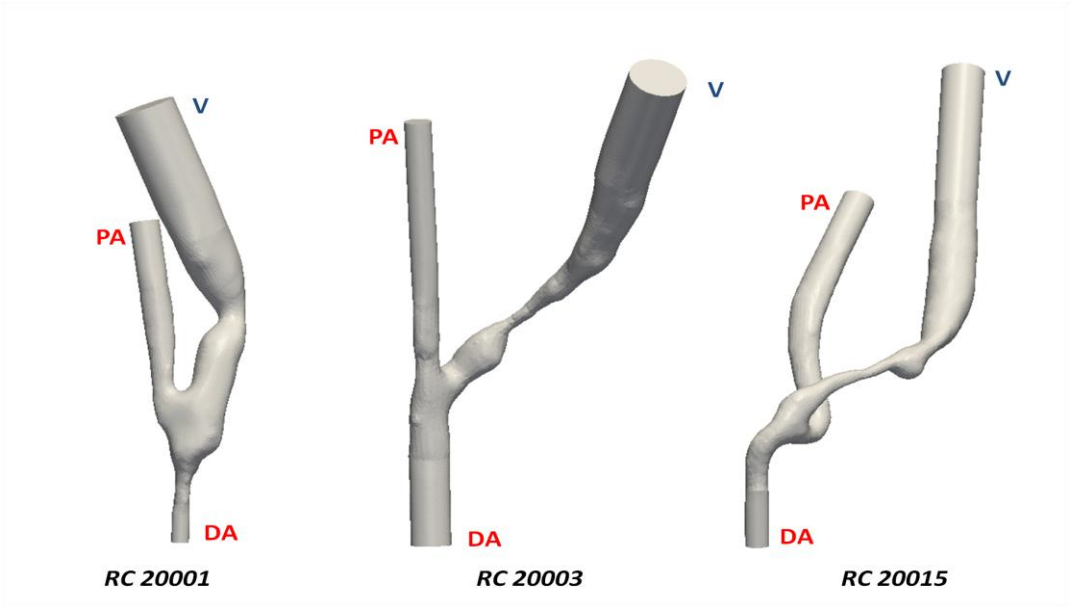

Figure 3.13 Models of radio-cephalic AVF reconstructed from CE-MRA

Three models were already available from previous work of Semperboni [53]: one brachio-cephalic AVF and two radio-cephalic AVF, shown in Figure 3.14:

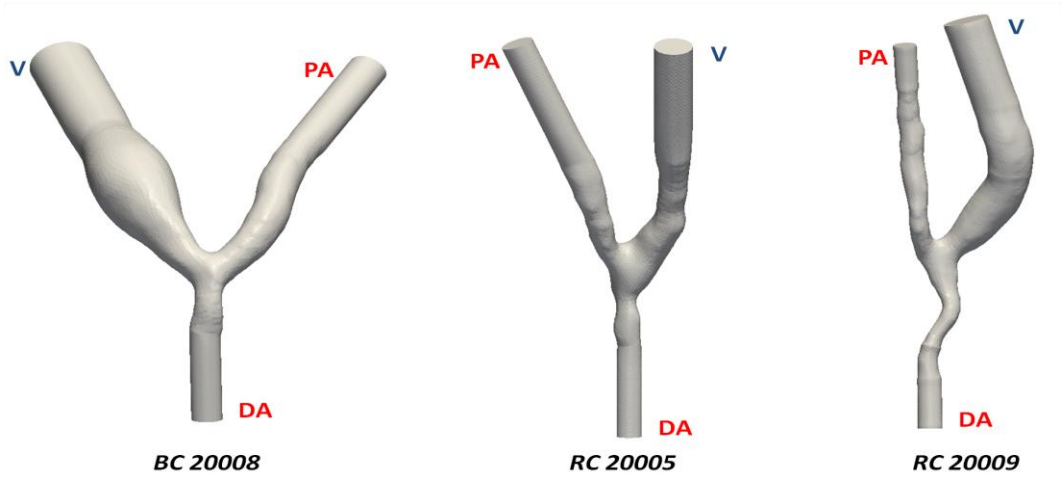

Figure 3.14 Models of AVF available from previous work [53]

As shown in the figures, some of the AVF have narrowing of the venous lumen due to stenosis formation, mainly located on the swing segment. It would be challenging to simulate the flow in these stenotic AVF and to assume the correct boundary conditions, since the blood volumetric flow rate was not directly measured and stenosis resistance was not yet implemented in the present 0D-1D solver [54].

In order to study the fluid dynamics in patient-specific AVF, we have decided to run CFD simulations in the "less stenotic" models, shown in Figure 3.15:

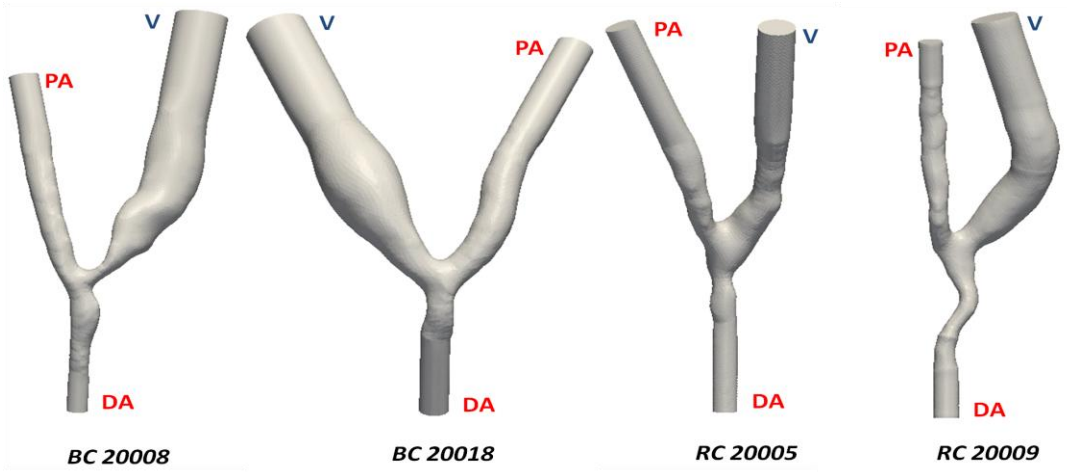

Figure 3.15 Models of AVF chosen for CFD simulations

4. CFD simulations

The present chapter contains the CFD patient-specific simulations. In the first part, the boundary conditions obtained using the pyNS solver and the numerical method used to run CFD simulations are presented, while the second part of the chapter contains the results obtained by CFD.

Regarding the hemodynamic variables of interest, special attention has been focused primarily on the instability of velocity and WSS vectors and then on disturbed flow parameters. Finally, we have analyzed the influence of three parameters on the transition to turbulence in these particular setting of high Reynolds AVF models: mesh density, position of zero-pressure boundary condition and the volumetric flow rate.

4.1 CFD patient-specific simulations

Numerical simulations have been performed using *Gnuid*, an open-source solver for the incompressible Navier-Stokes equations that, based on the flexibility in element type, adaptive mesh refinement and parallelization, offered by the *libMesh* finite element library [60], [61]. The discrete formulation of *Gnuid* is based on a pressure-correction scheme, combining a discontinuous Galerkin (dG) approximation for the velocity and a standard continuous Galerkin (cG) approximation for the pressure. The main advantage of the pressure-correction algorithm is the reduced computational cost, due to the use of cG approximation. Furthermore, the dG discretization of the decoupled momentum equation renders this method suitable for high Reynolds numbers simulations (convection-dominated pulsatile flows). The solver has been validated against a large set of classical two- and three-dimensional tests covering a wide range of Reynolds numbers and has proved effectiveness, accuracy and low computational cost for the simulation of convection-dominated flows [62]. Since the successful validation, the *Gnuid* solver can be employed to reliably predict flow patterns and pressure drops in patient-specific models of VA in patients on hemodialysis.

4.1.1 Boundary conditions

Patient-specific boundary conditions imposed on *Gnuid* have been obtained using the Python Network Solver (*pyNS*), an open source tool developed in order to simulate hemodynamic changes induced by AVF surgery and long-term vascular and cardiac adaptation. The computational model is based on 0D/1D pulse wave propagation of pressure and flow and is able to simulate vessel wall remodeling and related changes in blood flow [54].

4.1.1.1 The network model of arm vasculature

The arm vascular network model used in the present work has been defined considering the main arteries and veins of interest with great detail of the upper arm hosting the VA [54]

starting from the ascendent aorta. Figure 4.1 shows the left lower arm radio-cephalic end-to-side fistula network model:

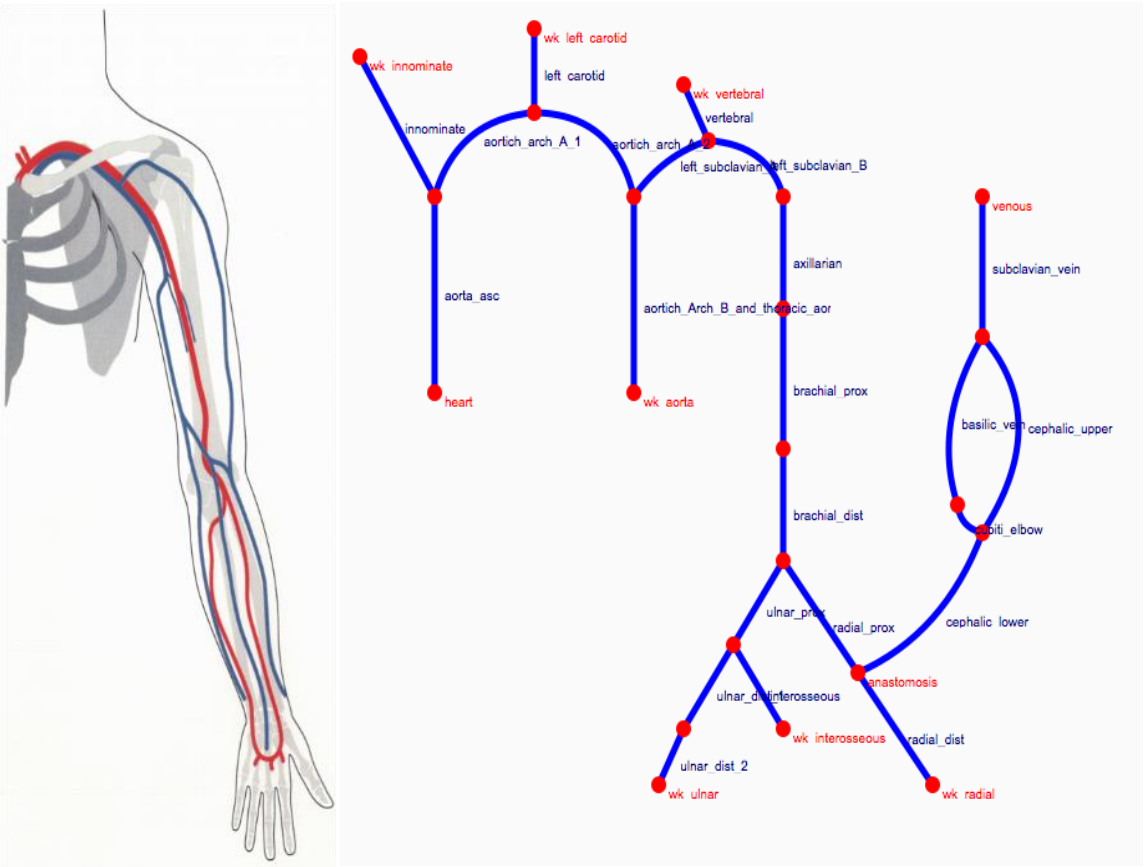

Figura 4.1 Left lower arm radio-cephalic end-to-side fistula network

In this lumped parameter network, the arm circulation is modeled with three types of elements, shown in Figure 4.2:

- 1D elements for principal arterial and venous vessels;
- 0D windkessel elements for peripherical resistances;
- 0D element for anastomosis.

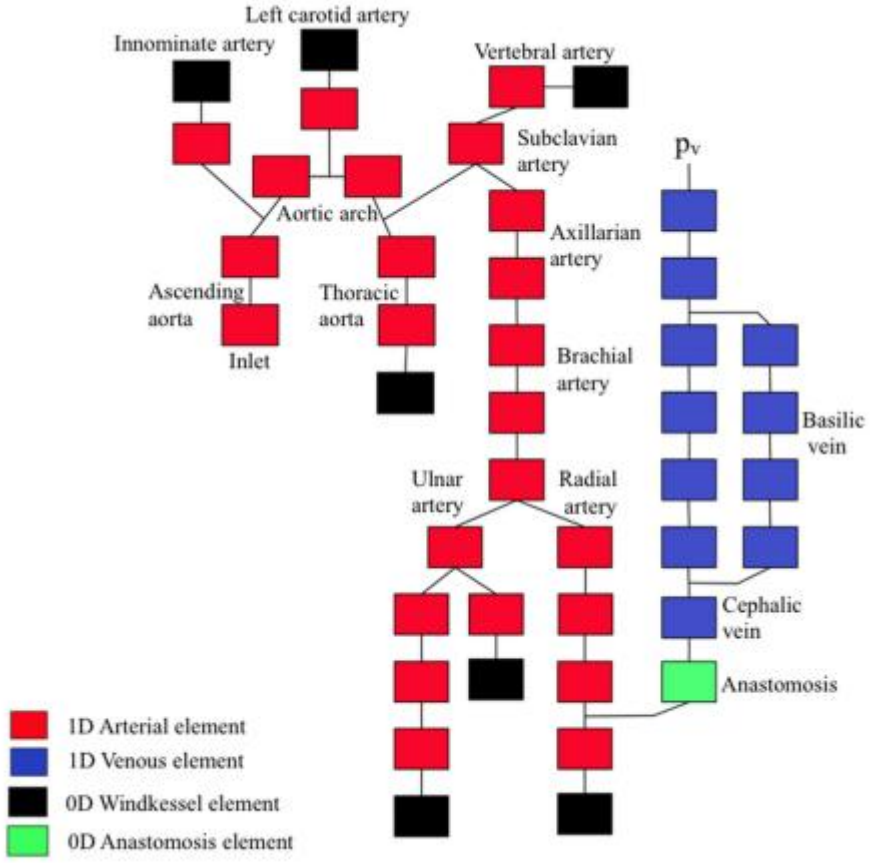

Figure 4.2 An example of left arm with side-to-end AVF: elements of the network

1D elements

This element has been implemented with a discretized 1D pulse wave propagation model as detailed in Huberts et al. [63]. The relation between pressure and volumetric flow rate for each vascular segment are derived from conservation of mass and momentum by assuming fully-developed incompressible Newtonian volumetric flow rate in a straight vessel. In the momentum equation the convection term, the axial diffusion term and the effect of body forces are neglected. The lumped parameter model obtained consists of a resistor per unit length R, representing the resistance to volumetric flow rate through the vessel and an inductor per unit length L, representing the inertia of the blood, in series (Figure 4.3).

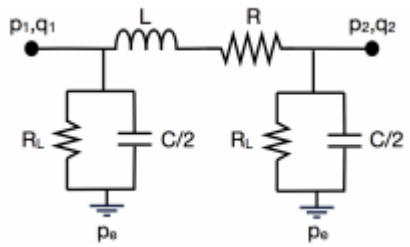

Figure 4.3 1D element for principal arterial and venous vessels

Resistance and inductance are evaluated as follows:

$$R_0 = \left(\frac{8\mu}{\pi a_0^4}\right) \quad L_0 = \left(\frac{\rho}{\pi a_0^4}\right)$$

$$R = \left(\frac{c_{q(\alpha_0)}}{2 - c_{p(\alpha_0)}}\right) R_0 \quad L = \left(\frac{1}{2 - c_p(\alpha_0)}\right) L_0$$

where a_0 is vessel's radius, and c_q and c_p are parameters depending on Womersley number α_0, corresponding to the characteristic frequency of a heartbeat (ω_0). To incorporate the storage capacity of the vessel in the model, a capacitor C is added to each side of the vascular segment, representing half of the total vascular compliance over that segment [63]. Furthermore, it is assumed that the artery is a thick-walled linear elastic tube.

The arterial compliance per segment length is then given by:

$$C = \frac{2\pi a_0^2 \left(\frac{2\, a_0^2\,(1 - \nu^2)}{h_0^2} + (1 + \nu)\left(\frac{2a_0}{h_0} + 1\right)\right)}{E_0 \left(\frac{2a_0}{h_0} + 1\right)}$$

with E_0 the Young's modulus, ν the Poisson's ratio and h_0 the wall thickness of the vessel. Veins diameter (D) and compliance (C) are defined as functions of pressure p:

$$D = D_0 \sqrt{1 - 0.55\left(1 - \frac{p}{1066.66 + p}\right)}$$

$$C = \frac{\pi D_0^2}{4} \frac{4.4}{1066.66 + p^2}$$

where D_0 is the vein diameter measured using the tourniquet.

The leakage *RL* is captured by adding linear resistances (representing resistance to volumetric flow rate through small side-branches) in parallel to the capacitors. In addition, extravascular pressures P_e are prescribed as a boundary condition parameter. The total resistance, total inertance and total compliance are obtained by integrating R, L and C over the segment length.

0D windkessel elements

Peripheral resistances have been modeled with a 0D three-element Windkessel model, as shown in Figure 4.4:

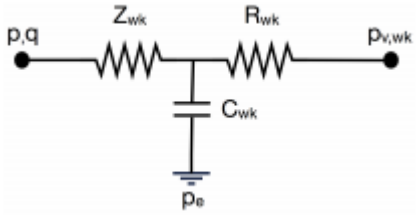

Figure 4.4 Windkessel element for peripheral resistances

The element consists of a characteristic impedance Z_{wk}, a resistance R_{wk} and a compliance C_{wk}. Total resistance R_{eq} (Z_{wk}+R_{wk}) is defined as:

$$R_{eq} = \frac{P_{mean}}{kQ_{CO}}$$

where *k is* the fraction of the cardiac output flowing though the peripheral bed, P_{mean} is the mean arterial pressure and Q_{CO} is the cardiac output. The pressure wave decreases during diastole with a time constant R_{wk}*C_{wk}, which can be obtained from the descending slope of the local pressure curve during diastole.

0D element for anastomosis

The anastomosis cannot be modeled by linear segments because the radial velocity component is no longer infinitesimally small compared to the axial velocity and flow separation occurs in this region. In this condition, the flow field is characterized by non-uniform velocity distribution and development of secondary flows.

Consequently, a special element is created to model the pressure drop, shown in Figure 4.5.

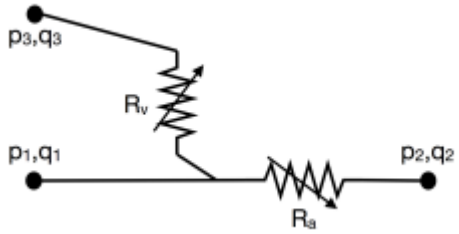

Figure 4.5 0D element for anastomosis modeling

The pressure drop is given by the following equation:

$$\Delta P = (\alpha \cdot Re^2 + \beta \cdot Re)\left(\frac{\mu_P^2}{1.557e^{-2}\rho_P\, radius^2}\right)$$

with α and β adimentional parameters depending on venous and arterial diameter.

4.1.1.2 The algorithm for vascular adaptation

The algorithm implemented in the solver is based on the finding that major increases in arterial blood flow lead to increases on arterial diameters and that artery diameter adapts to keep peak pulsatile WSS constant, rather than mean WSS [64]. Consequently, a deviation from a reference value (τ_{ref}) was assumed to induce a change in vessel diameter (Φ) according to the following equation:

$$\frac{d\Phi}{dt} = C \cdot (\tau_{peak} - \tau_{ref})$$

where C is an adaptation rate constant.

4.1.1.3 pyNS boundary conditions

Generic patient data for the vascular tree were implemented into the *pyNS* solver, representing geometrical characteristics of a normal subject (male or female). The *pyNS* solver may be informed by the user with patient-specific data if available, otherwise the model will take into account the generic data, matched by age and gender.

Table 4.11 shows an example of patient-specific data for the vascular network.

Vessel name	Length (cm)	Starting diameter (mm)	Ending diameter (mm)
Ascending Aorta	6.67	34.10	31.19
Aortic Arch 1	1.69	31.19	30.26
Aortic Arch 2	1.02	30.26	29.53
Thoracic aorta	12.88	29.53	25.09
Left carotid	20.16	6.61	6.61
Right carotid	16.80	6.42	6.42
Right subclavian A	3.10	8.88	8.44
Right subclavian B	7.94	8.68	7.74
Vertebral	14.11	3.60	3.42
Innominate	3.36	12.02	12.02
Left subclavian A	4.13	8.97	8.52
Axillary	9.74	7.74	5.13
Brachial proximal	13.80	5.13	4.91
Brachial distal	4.60	4.91	4.83
Radial proximal	15.77	3.14	2.40
Radial distal	5.26	2.40	2.32
Ulnar proximal	4.20	3.87	3.87
Ulnar distal	16.84	2.17	2.05
Interosseous	12.61	1.69	1.69
Lower cephalic vein	17.70	2.88	3.60
Medial cubital vein	4.00	2.40	2.64
Upper cephalic vein	30.30	3.60	6.00
Upper basilic vein	30.30	2.64	3.60
Axillary vein	17.40	8.40	10.80

Table 4.1 Example of patient for the vascular network model

Table 4.2 contains the minimal patient-specific dataset that the user has to set in *pyNS* to calculate realistic AVF boundary conditions:

Height	160	cm
Weight	70	kg
Age	62	years
Systolic pressure	110	mmHg
Diastolic pressure	80	mmHg
Cardiac frequency	60	bpm
Hematocrit	30	%
Plasmatic proteins concentration	6.2	g/dL
Hypertension	No	-
Diabetes	No	-

Table 4.2 Patient specific data for the vascular network model

Figure 4.6 shows the results of a simulation of a brachio-cephalic AVF: minimum and maximum diameters of the vessels and mean values of pressure, flow, WSS and Reynolds are available in preoperative conditions and at 0, 10, 20, 30 and 40 days after surgery.

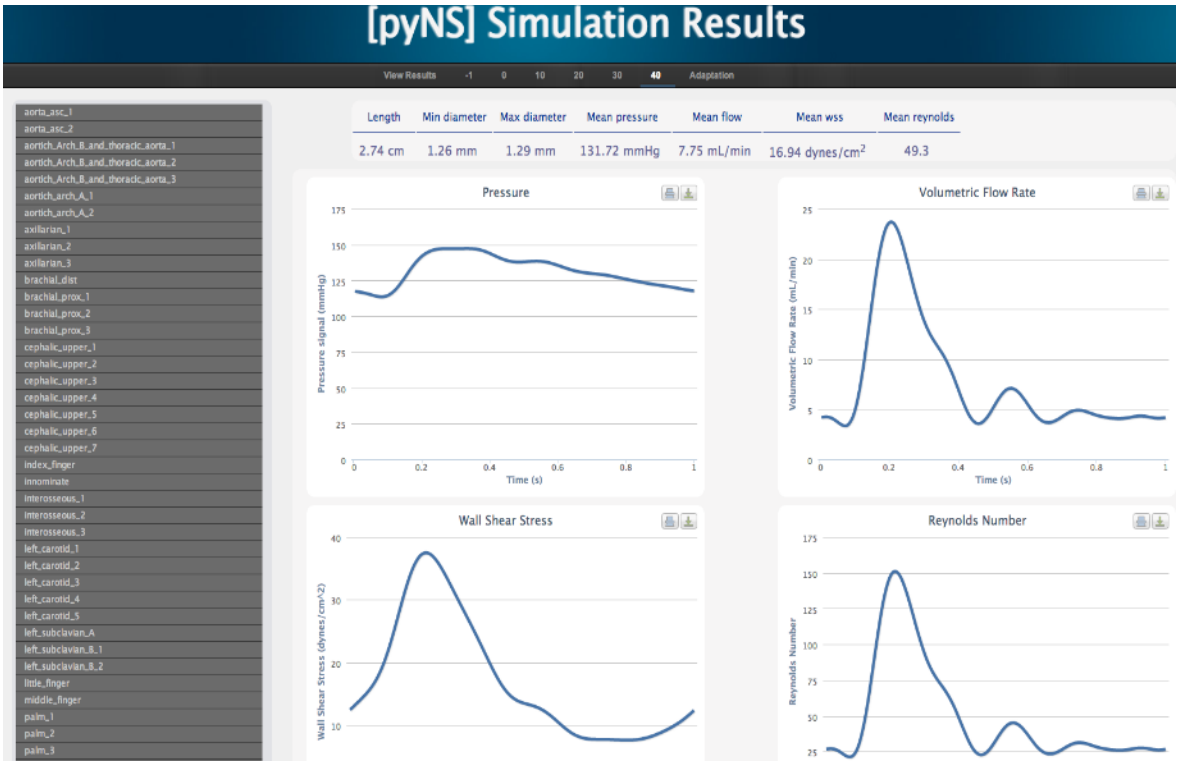

Figure 4.6 Example of a *pyNS* simulation: by selecting a vessel on the left, it is possible to visualize the waveforms of pressure, flow, WSS and Reynolds number during the cardiac cycle. On the top black strip it is possible to select the time after surgery which the user is interested in

4.1.1.4 Boundary condition used in the CFD simulations

The *pyNS* solver generated output of the volumetric flow rates throughout the cardiac cycle, which can be subsequently modeled by Fourier analysis. For the side-to-end AVF modeled in the present thesis, we used the flow waveform of the artery segment closer to anastomosis. Fourier coefficients have been calculated for the proximal artery inlet and distal artery outlet and set in *Gnuid* (an example of input file is shown in Appendix A). Zero-pressure boundary condition has been set on the vein outlet and zero-velocity on the walls, which were considered rigid, has been applied to ensure no-slip condition.

4.1.1.5 Blood rheology

Blood has been considered as a Newtonian and incompressible fluid, with constant density of 1.045 g/cm^3. Patient specific rheology has been, however, taken into account by calculating whole blood dynamic viscosity from patient's hematocrit and plasmatic proteins concentration, using the following relations [65]:

$$\ln(k) = 1.3435 - 2.803H_t + 2.71{H_t}^2 - 0.6479{H_t}^3$$

$$\mu = \sqrt{1 - H_t k} \cdot \left(0.204 + 0.177C_p\right)$$

where μ is the blood dynamic viscosity, H_t is the hematocrit (in %) and C_p is the plasmatic proteins concentration in (mg/dL).

4.1.1.6 Patient-specific parameters and velocity inlet and outlet

Simulations with pyNS solver have been computed for the selected brachio-cephalic and radio-cephalic cases. Patient-specific parameters for pyNS and corresponding velocity inlet and outlet boundary conditions to be used in CFD simulations are presented in tables and figures below.

BC 20008

Gender	female	
Arm	left	
Height	167	cm
Weight	44	kg
Systolic pressure	110	mmHg
Diastolic pressure	80	mmHg
Brachial flow	41	mL/min
Radial flow	9.2	mL/min
Ulnar flow	3.3	mL/min
Hematocrit	29	%
Plasmatic proteins concentration	6.23	g/dL
Hypertension	No	-
Diabetes	No	-

Table 4.3 Patient-specific parameters of BC 20008 set in the pyNS solver

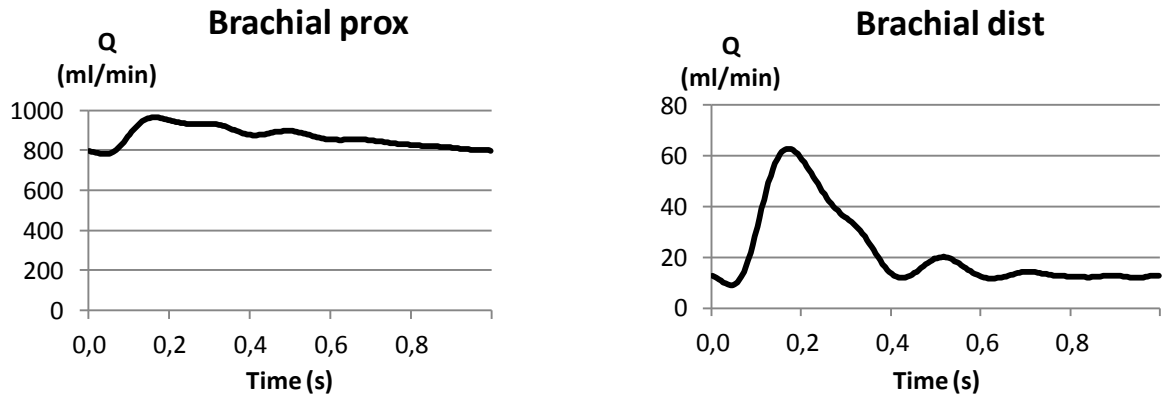

Figure 4.7 Boundary conditions of BC 20008 obtained using pyNS solver

BC 20018

Gender	female	
Arm	left	
Height	162	cm
Weight	72	kg
Systolic pressure	125	mmHg
Diastolic pressure	60	mmHg
Brachial flow	87	mL/min
Radial flow	30	mL/min
Ulnar flow	24	mL/min
Hematocrit	36	%
Plasmatic proteins concentration	7.0	g/dL
Hypertension	No	-
Diabetes	No	-

Table 4.4 Patient-specific parameters of BC 20018 set in the pyNS solver

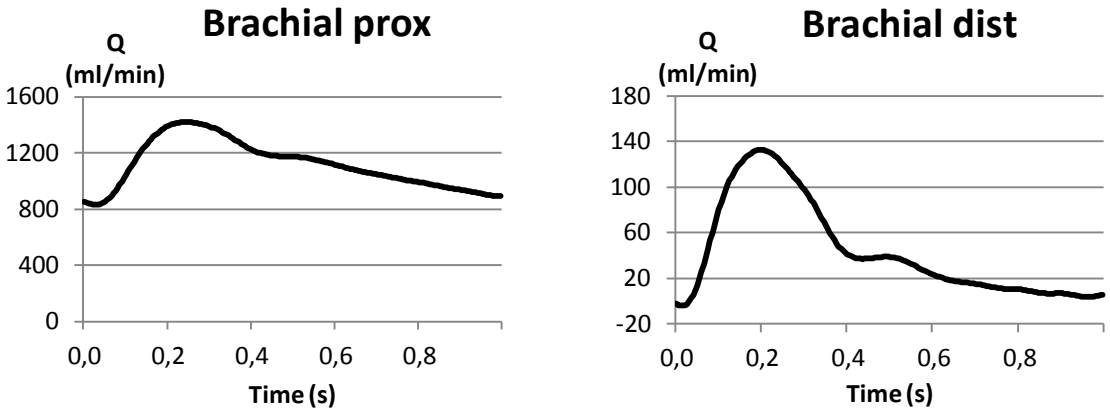

Figure 4.8 Boundary conditions of BC 20018 obtained using pyNS solver

RC 20005

Gender	male	
Arm	left	
Height	186	cm
Weight	71	kg
Systolic pressure	155	mmHg
Diastolic pressure	90	mmHg
Brachial flow	228	mL/min
Radial flow	54	mL/min
Ulnar flow	30	mL/min
Hematocrit	29	%
Pasmatic proteins concentration	5.39	g/dL
Hypertension	Yes	-
Diabetes	No	-

Table 4.5 Patient-specific parameters of BC 20005 set in pyNS solver

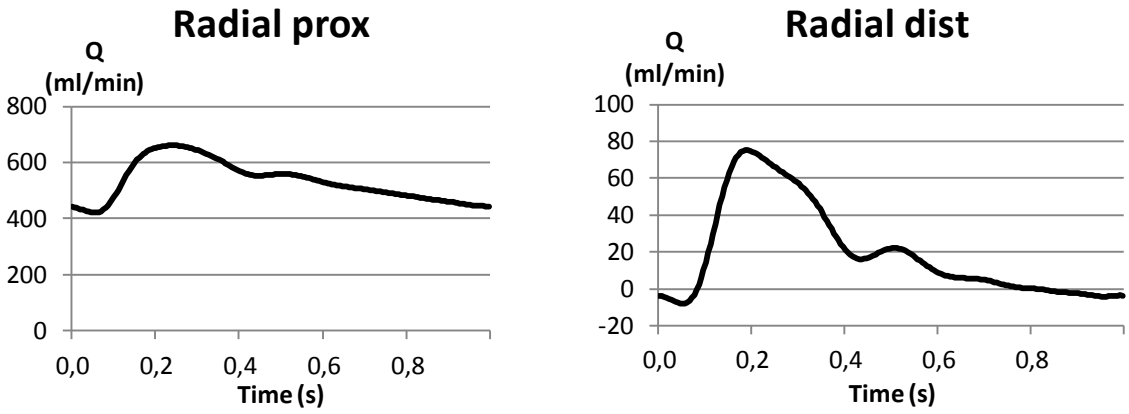

Figure 4.9 Boundary conditions of BC 20005 obtained using pyNS solver

RC 20009

Gender	male	
Arm	right	
Height	178	cm
Weight	92	kg
Systolic pressure	110	mmHg
Diastolic pressure	60	mmHg
Brachial flow	143	mL/min
Radial flow	48	mL/min
Ulnar flow	30	mL/min
Hematocrit	39	%
Pasmatic proteins concentration	7.0	g/dL
Hypertension	No	-
Diabetes	Yes	-

Table 4.6 Patient-specific parameters of BC 20009 set in pyNS solver

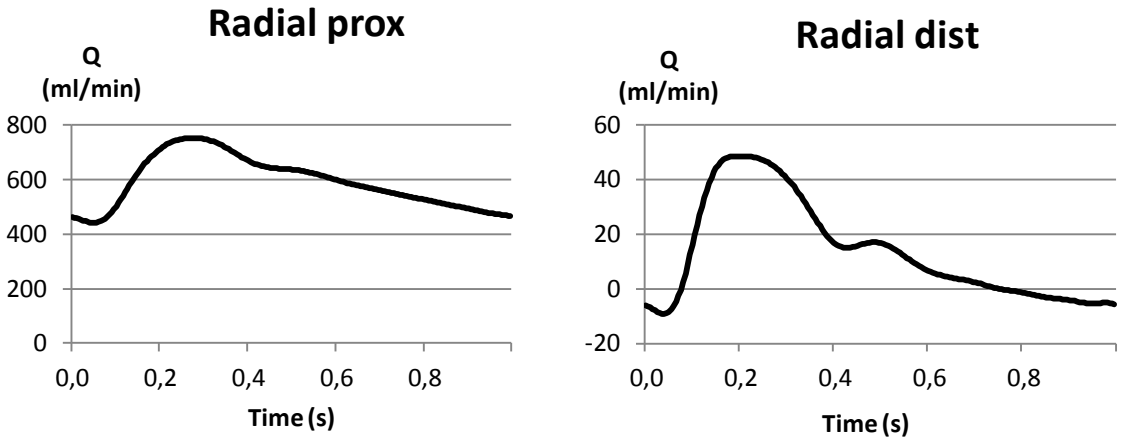

Figure 4.10 Boundary conditions of BC 20009 obtained using pyNS solver

4.1.2 Computed simulations

In the first part of the thesis, with the aim of studying the fluid dynamics in patient-specific AVF, pulsatile CFD simulations were computed on four models: two brachio cephalic AVF (BC 20008 and BC 20018) and two radio-cephalic AVF (RC 20005 and RC 20009). Table 4.7 contains the most important CFD patient-specific data.

The scaling factor specifies the percentage of flow through the distal artery compared to the flow entering from the proximal artery and *Re* and α indicate the Reynolds number and the Womersley number respectively.

PATIENT	BC 20008	BC 20018	RC 20005	RC 20009
Mesh [elements]	855327	668853	1259417	1053447
Qmean inlet [mL/min]	866.06	1104.35	531.78	591.51
Qmean outlet [mL/min]	22.2	41.86	19.73	13.52
Scaling factor [%]	2.56	3.79	3.71	0.02
Re inlet	1517	1450	969	1502
α inlet	3.86	4.26	3.28	3.40
Blood viscosity [Poise]	0.027	0.034	0.024	0.024

Table 4.7 CFD data

In the second part of our study four additional simulations have been computed in order to study the influence of the following parameters on the solution:

- ***Mesh density***: RC20005 has been simulated reducing the number of elements from 1259417 to 503981 elements.
- ***Zero-pressure boundary condition:*** RC20009 has been simulated imposing the zero-pressure boundary condition to the distal outlet (initial simulation was done with this boundary condition on the vein outlet).
- ***Blood volumetric flow rate***: RC 20009 has been simulated reducing the input and setting a half and a quarter of the starting flow rate (621 l/min): the new input flow rates are 310,5 l/min and 155,25 l/min, respectively.

4.1.3 Postprocessing

The hemodynamic parameters of interest (velocity, streamlines, WSS, disturbed flow metrics) have been post-processed using Paraview (**http://www.paraview.org**), an open- source multiple-platform application for scientific visualization. Paraview was built on top of the Visualization Tool Kit (VTK) C++ libraries (**http://www.vtk.org**), and has a client-server architecture to facilitate remote visualization of large datasets. A big part of post-processing was based on Paraview filters: the most used filter was *Calculator*, which processes one or more input arrays based on an expression provided by the user to produce a new output array.

4.1.4 Disturbed flow parameters

Time-Averaged Wall Shear Stress (TAWSS) represents the time-averaged WSS calculated as:

$$TAWSS = \frac{1}{T}\int_0^T |\tau_w| dt$$

where τ_w (t) is the instantaneous WSS vector and T is the period of the cardiac cycle. TAWSS has been computed in every surface node of the mesh with *Temporal Statistics* Paraview filter.

Oscillatory Shear Index (OSI), originally introduced by Ku and al. [66] with the aim of quantifying the degree of deviation of the WSS from its average direction, was calculated [67] as follows:

$$OSI = \frac{1}{2}\left(1 - \frac{|\int_0^T \tau_w dt|}{\int_0^T |\tau_w|\, dt}\right)$$

This index is non-dimensional and can take values between 0 and 0.5, higher OSI indicating larger shear stress directions variations. OSI has been calculated by using *Calculator* Paraview filter.

Because of the lack of a parameter able to distinguish between uniaxial and multidirectional flows, the *Transverse Wall Shear Stress* (transWSS) was introduced by

Peiffer et al. [68], with the aim of better describing disturbed flows. In fact, a characteristic of multidirectional disturbed flow is that the WSS vector does not remain parallel to a single axis throughout the cardiac cycle. TransWSS was defined as the time-average of WSS components perpendicular to the mean flow direction, according to the following definition:

$$transWSS = \frac{1}{T}\int_0^T \left| \tau_w \left(\vec{n} \, \frac{\int_0^T \tau_w \, dt}{\left| \int_0^T \tau_w dt \right|} \right) \right|$$

where $\vec{n}$ is the normal to the AVF wall surface.

On the basis of this definition, we calculated transWSS from the time-averaged WSS component in the mean flow direction, defined as dirWSS. Briefly, once dirWSS has been calculated, it has been normalized (unit_dir) and the direction perpendicular to the mean flow (unit_trans) was obtained using a cross product between this normalized vector and WSS. A dot product between unit_trans and WSS resulted in transWSS vector, perpendicular to dirWSS.

We also introduced a new index called *Instability Index*, defined as follows:

$$Instability\ Index = \frac{\tau_{mean} - \frac{(\tau_{max+}\tau_{min})}{2}}{\frac{\tau_{max-}\tau_{min}}{2}}$$

where τ_{mean} is the average value of WSS vector and τ_{max} and τ_{min} are respectively the maximum and minimum magnitude of the WSS vector. The instability index locates sudden changes in WSS magnitude and provides more information regarding zones with oscillating WSS.

4.2 Results of the CFD simulations

4.2.1 General flow pattern

4.2.1.1 Velocity 2D streamlines

Streamlines are curves that are instantaneously tangent to the velocity vector of the flow. These show the direction a fluid element will travel at any point in time. Velocity 2D streamlines are shown on a longitudinal slice of the AVF at systolic peak (Figure 4.11). All the models show straight streamlines in the proximal artery that evolve in vortices and secondary flows in the anastomosis: the flow entering the vein collides against the outer wall near the anastomosis creating an area of recirculation on the opposite innerwall.

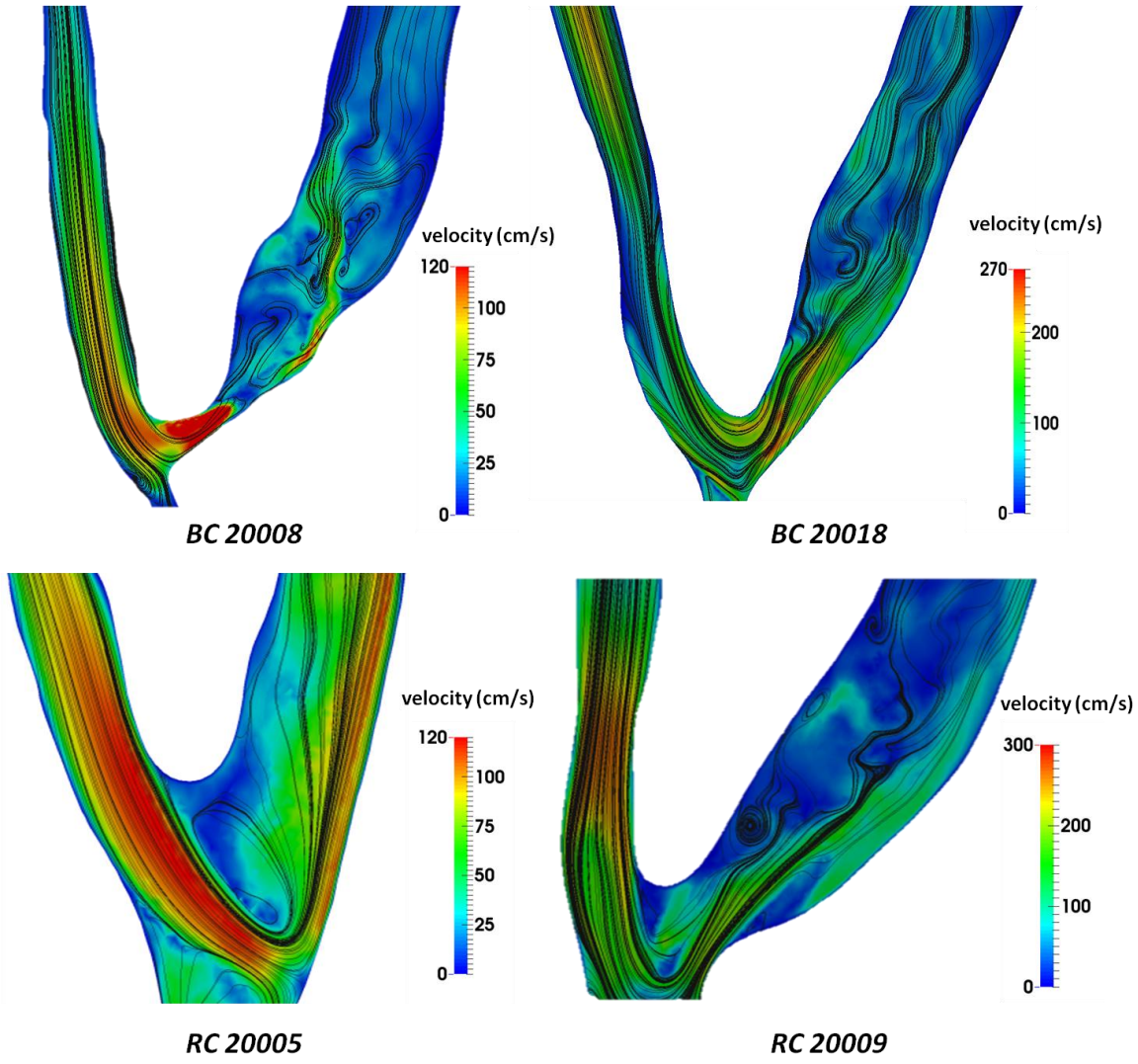

Figure 4.11 Velocity 2D streamlines of the AVF, representative of at the peak systolic blood flow volume instance

4.2.1.2 Velocity 3D streamlines

3D streamlines of velocity vector are useful to visualize flow instability in the anastomosis. Representative velocity 3D streamlines for peak systole for the AVF are reported in Figure 4.12: in the proximal artery they are straight, while they start sling right after the anastomosis, where the flow split and the high flow (Reynolds number) cause vortices and instabilities in the vein.

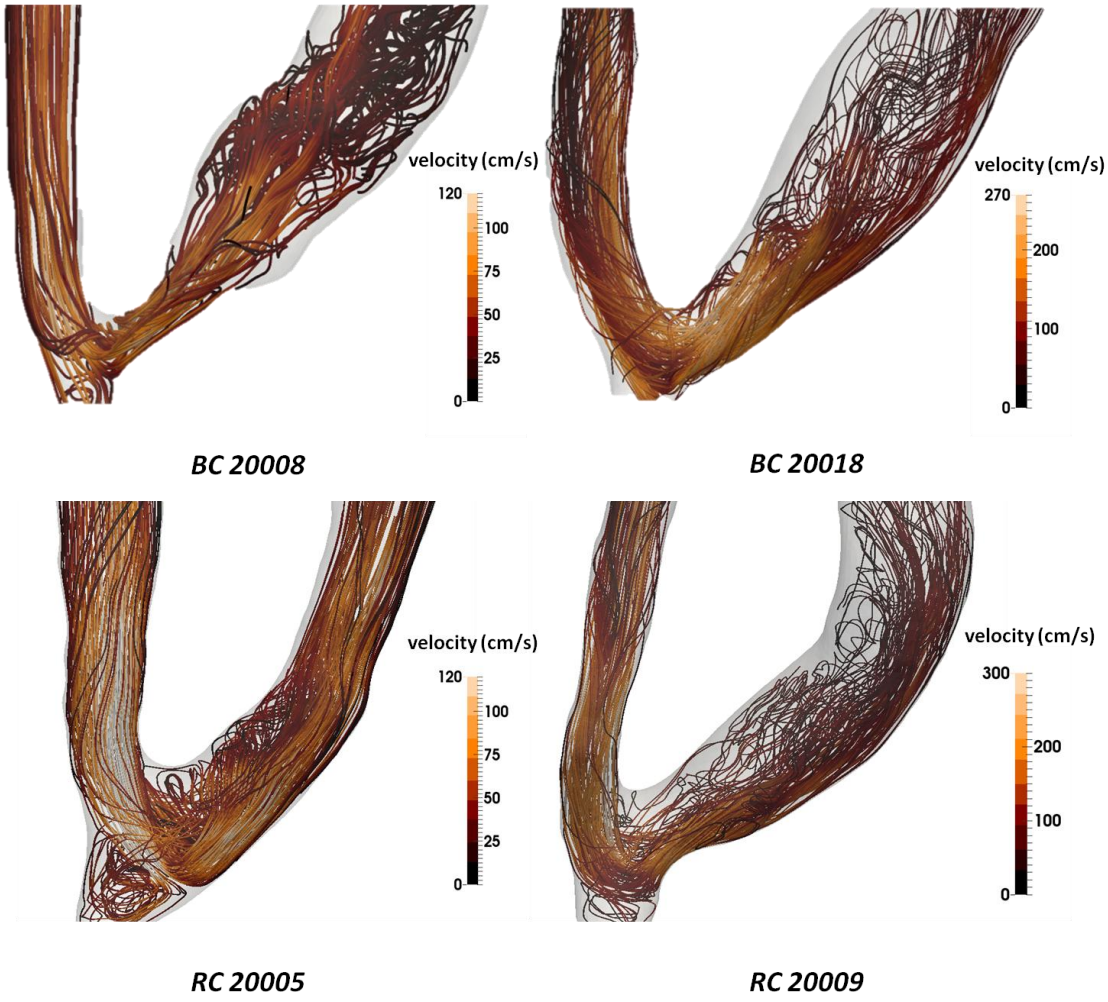

Figure 4.12 Velocity 3D streamlines inside the AVF, representative of at the peak systolic blood flow volume instance

4.2.2.3 Velocity instability

In order to describe the trend of velocity in the AVF some feature points have been identified along the centerline of every model. Figures 4.13 to 4.16 show the velocity, normalized by its cycle-averages, at the selected feature points. In all models velocity traces show similar trends in different zones of the AVF revealing laminar flow in the proximal feeding artery and flow instability right after the anastomosis that damps slightly as it moves in the distal vein. In the distal artery, there are fewer oscillations than in the anastomosis, since the blood volumetric flow rate is rather small.

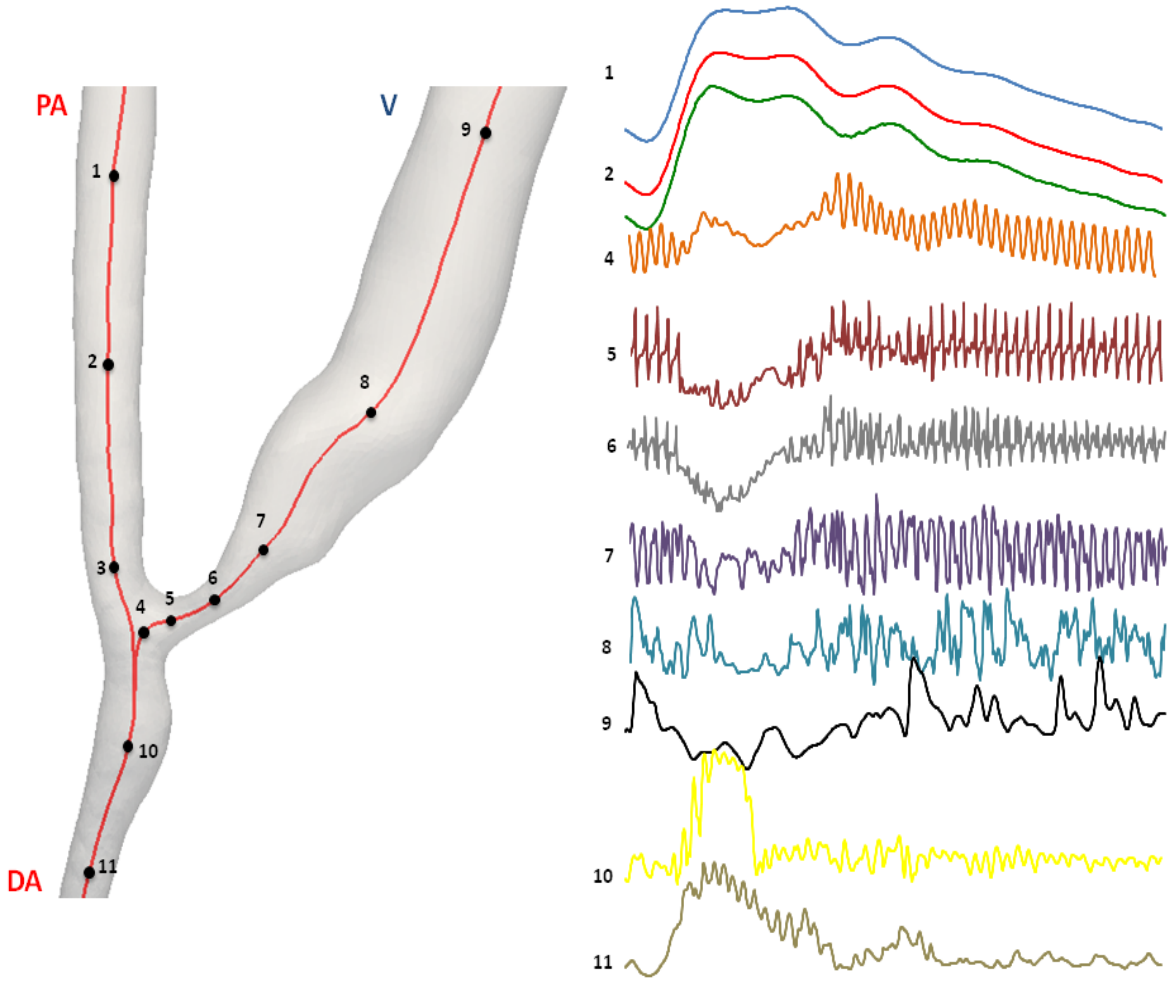

Figure 4.13 Velocity vs. time traces, normalized by their respective cycle averages, at selected probe points of BC 20008

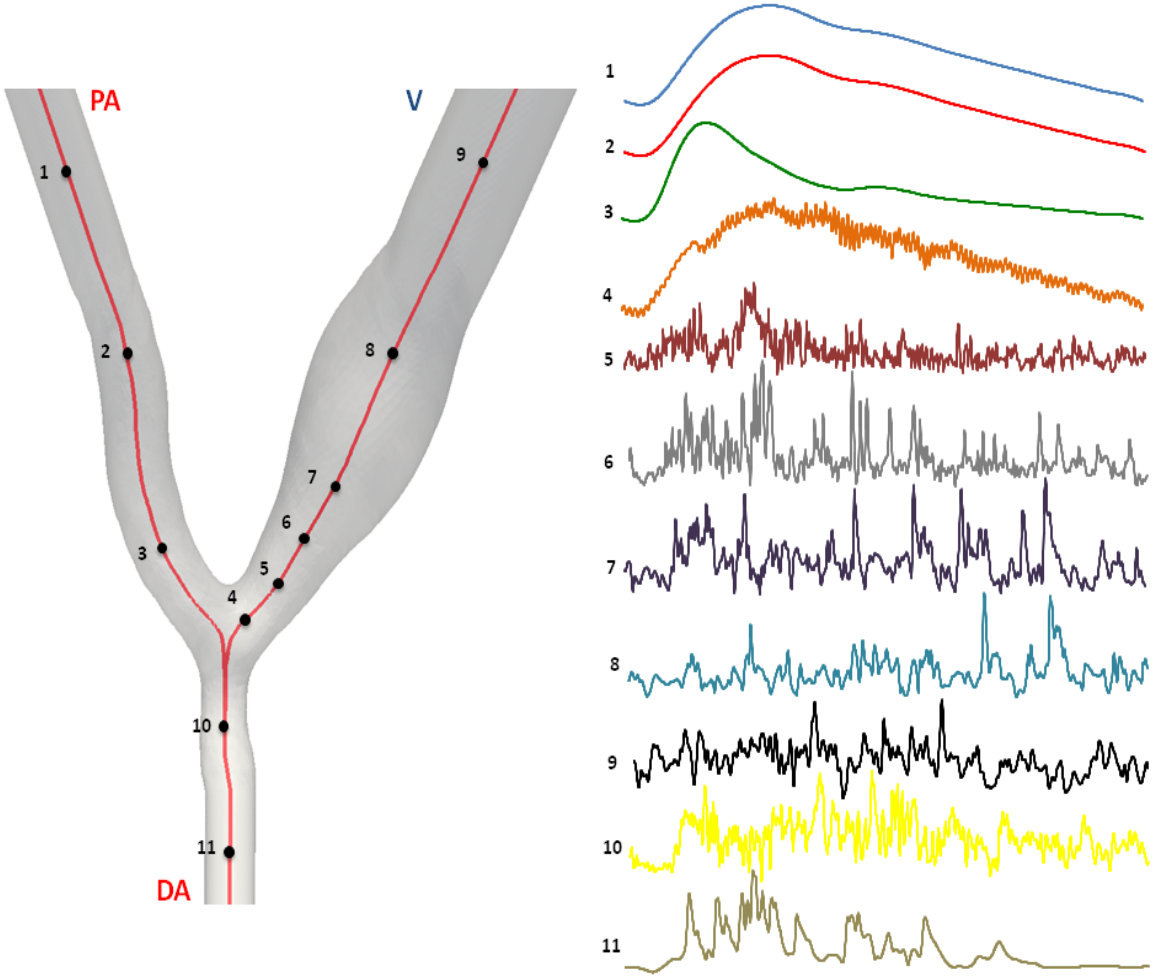

Figure 4.14 Velocity vs. time traces, normalized by their respective cycle averages, at selected probe points of BC 20018

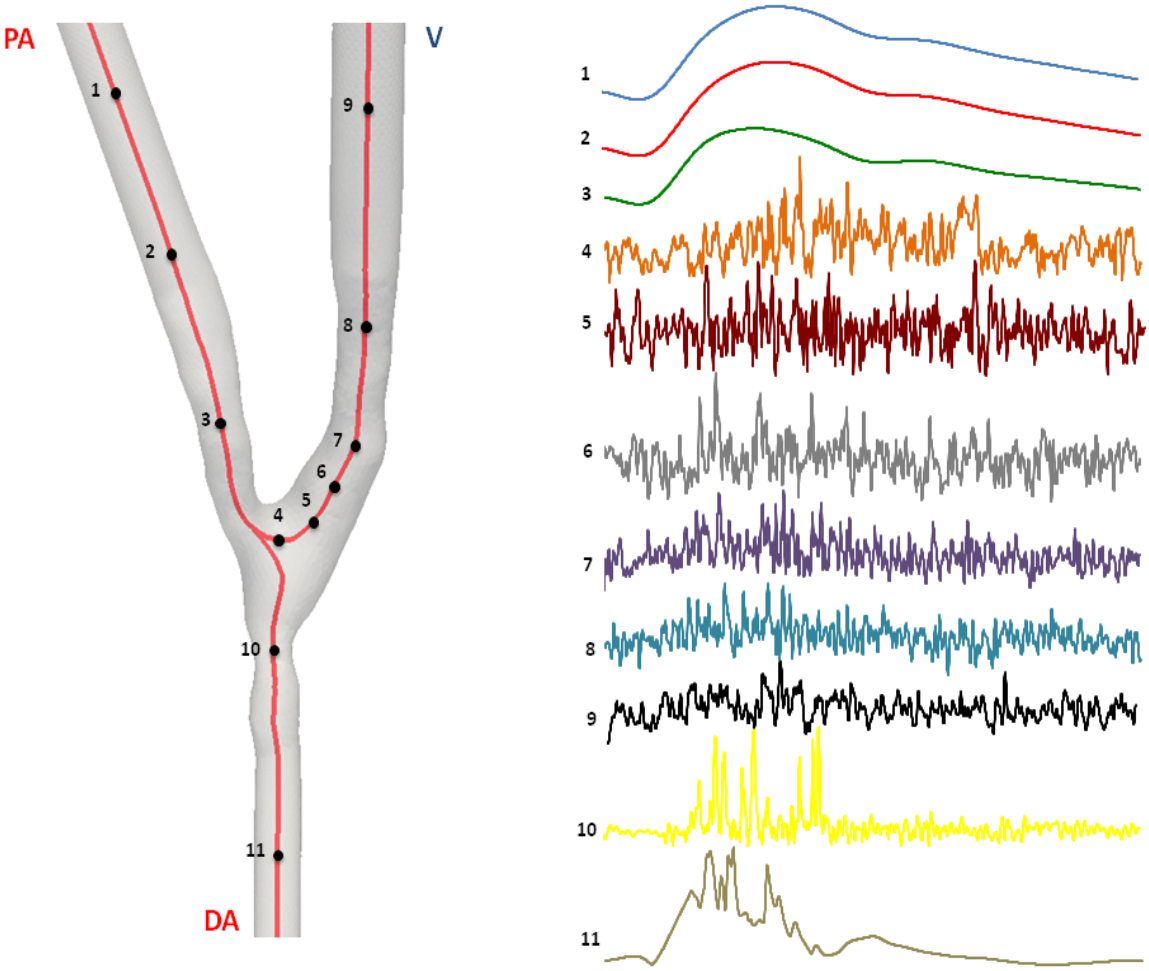

Figure 4.15 Velocity vs time traces, normalized by their respective cycle averages, at selected probe points of RC 20005

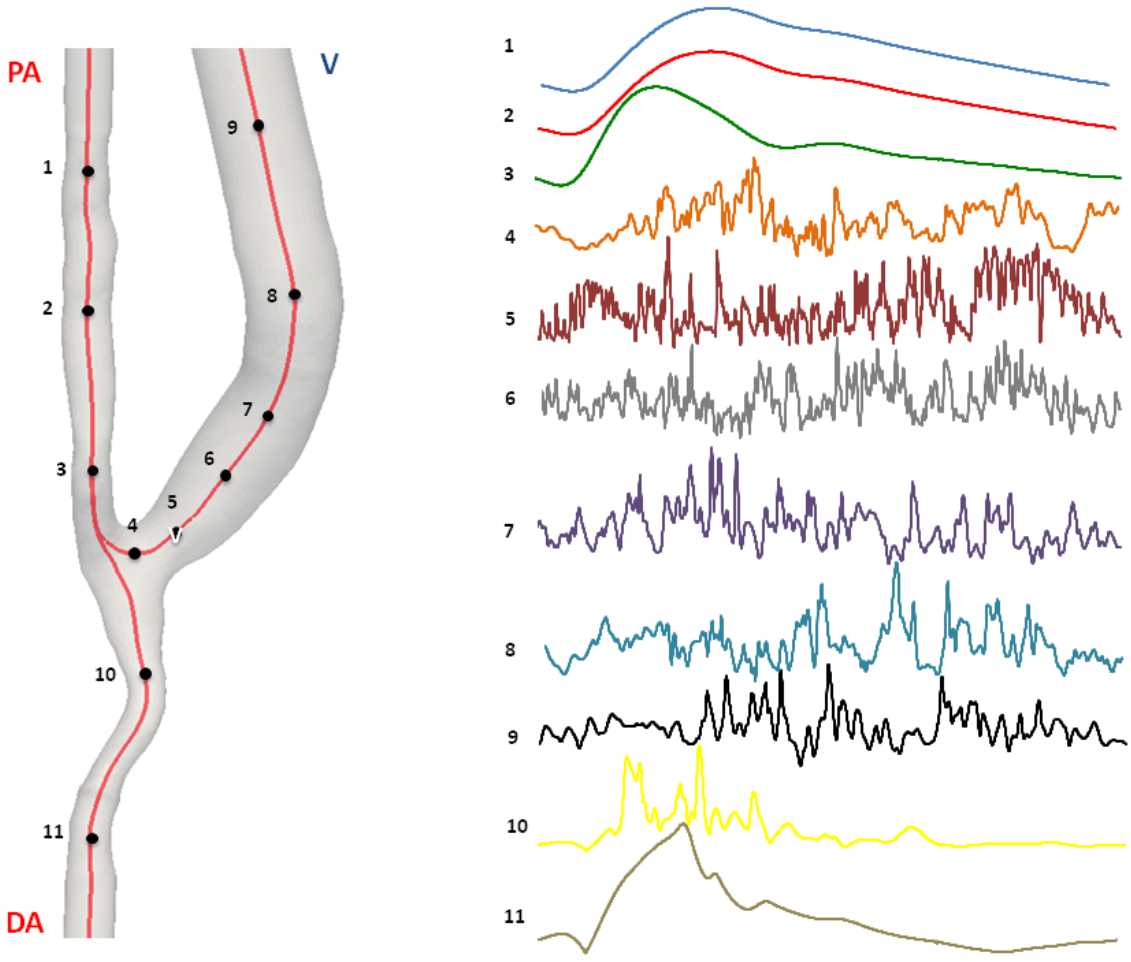

Figure 4.16 Velocity vs time traces, normalized by their respective cycle averages, at selected probe points of RC20009

4.2.2.4 Velocity isosurfaces

The increase in flow complexity in the vein can be observed in Figure 4.17 where velocity magnitude isosurfaces are represented at three different instances of the cardiac cycle: peak systole, mid-diastole and end-diastole. Right after the anastomosis, the isosurface loses the well-constructed shape and the smoothness shown in the proximal artery: it breaks and fills just a limited part of the vessel, revealing the flow instability characteristic for the vein.

Figure 4.17 Velocity magnitude isosurfaces representative of the peak systolic, mid-diastole and end-diastole blood volume flow instance, using a velocity threshold value of 80 cm/s

Furthermore, after the change in direction at the anastomosis, the bulk flow becomes more adherent to the outer wall of the vein, as inertial forces start to dominate viscous forces. It is evident that the flow can be considered stable in the proximal artery and presents a significant instability in the anastomosis and in swing segment of the vein. This characteristic feature of flow is similar in all AVF cases.

4.2.2.5 Flow vorticity (λ2 criterion)

A typical vortex flow structure is shown in Figure 4.18, which shows coherent structures of case RC 20009 identified by the λ_2 criterion of Jeong and Hussain [69] at three different times of the cardiac cycle. The majority of the flow entering the fistula through the proximal artery must make a 180° turn as it leaves through the proximal vein, generating vortex cores on the anastomosis. Vortex structures are more extended at peak systole but they are present even during diastole.

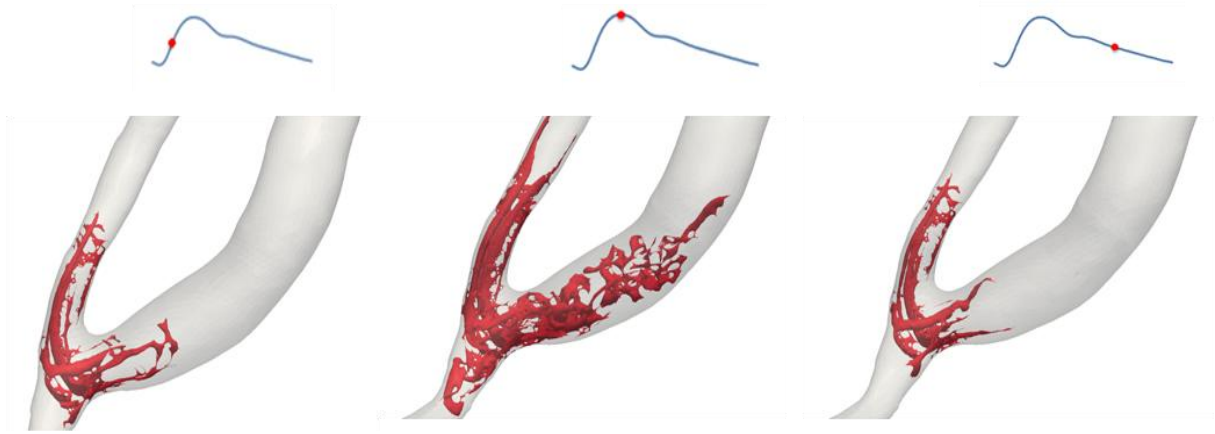

Figure 4.18 Coherent vortex structures within the anastomosis at three different time points of cardiac cycle, identified by the λ2 criterion, using a threshold velocity value of 80cm/s

4.3.1 Wall shear stress patterns

Figures 4.19 to 4.22 show the WSS patterns for the four simulated AVF: the symmetry in the distribution of high WSS at the anastomosis zone is evident. Blood coming from the proximal artery impinges the wall of the vein and creates a high WSS at anastomosis, which is a common feature of all the AVF. High WSS area is more extended at peak systole, but at mid-diastole and end-diastole the position of high WSS zones is maintained, as well as the position of low WSS zones.

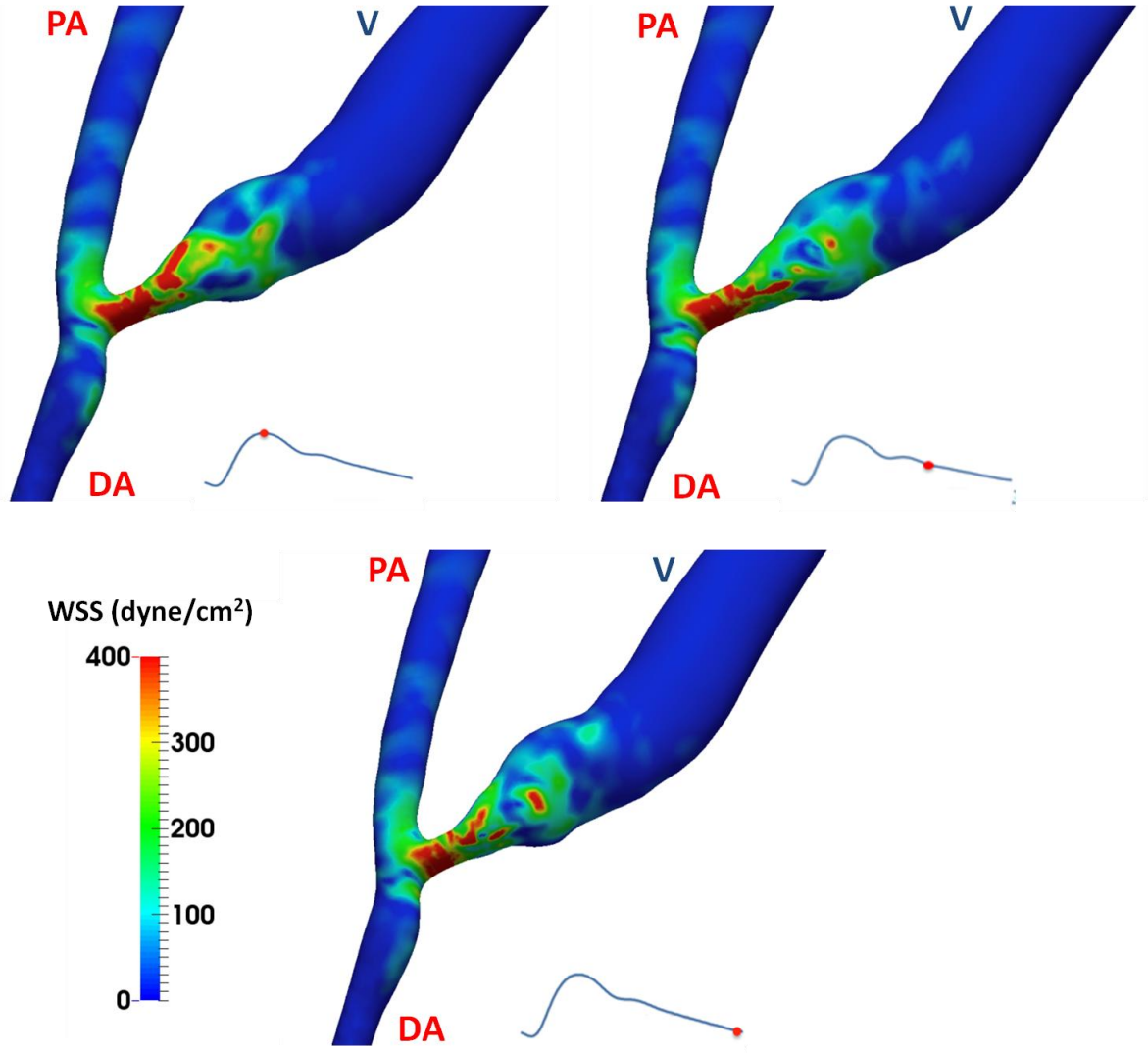

Figure 4.19 WSS patterns on the AVF surface of BC 20008 representative of the peak systolic, mid-diastolic and end-diastolic blood flow volume

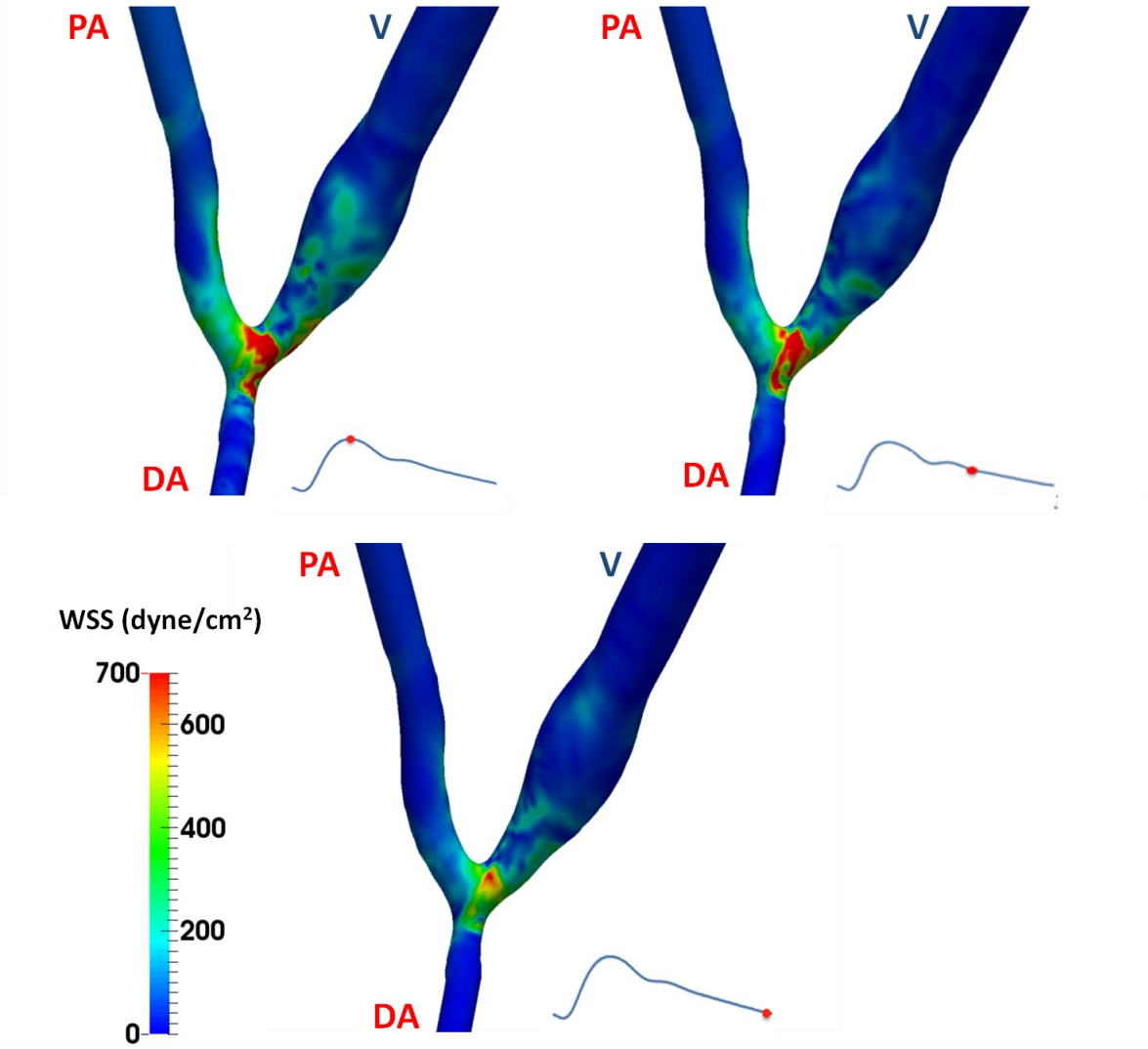

Figure 4.20 WSS patterns on the AVF surface of BC 20018 representative of the peak systolic, mid-diastolic and end-diastolic blood flow volume

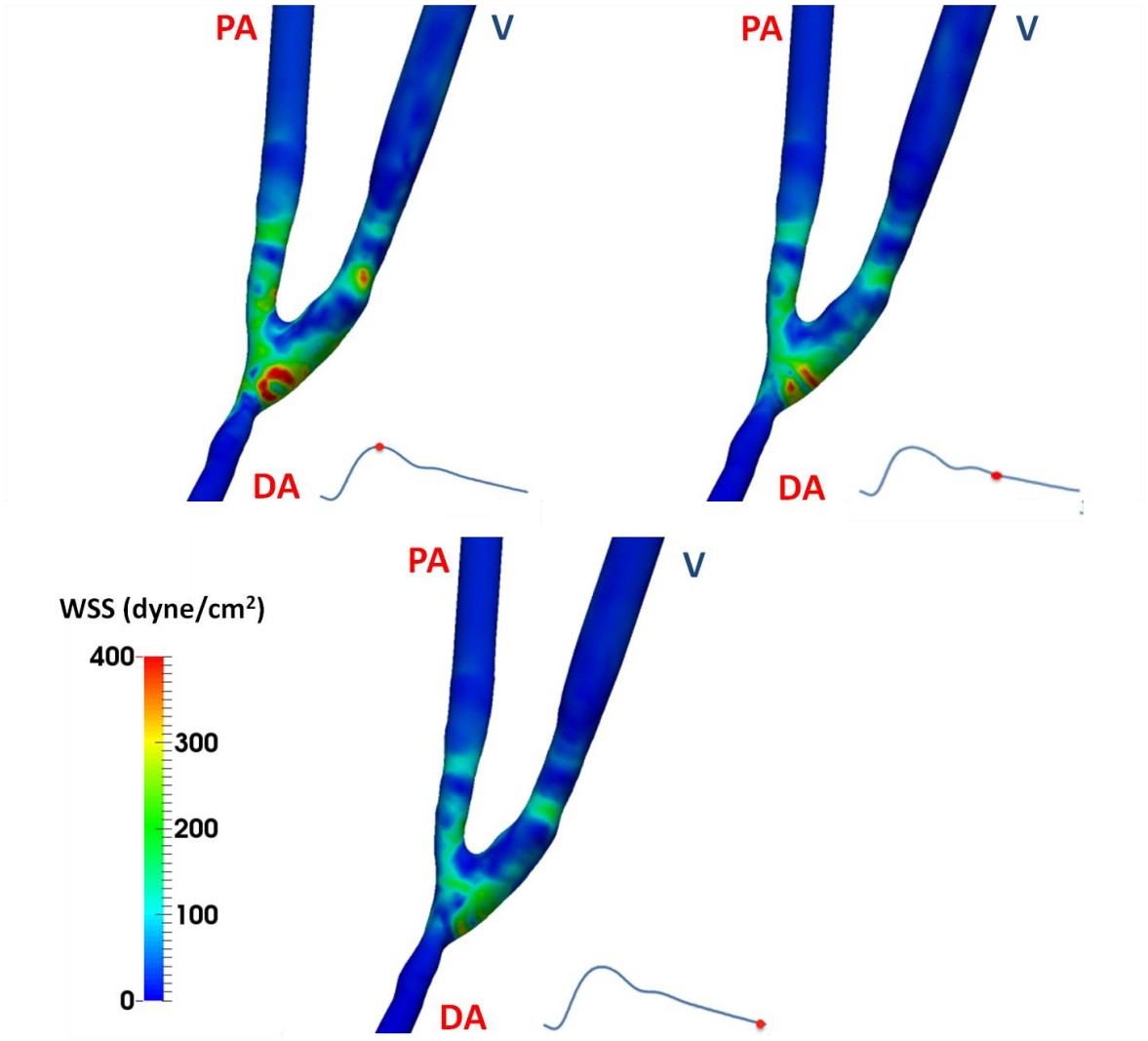

Figure 4.21 WSS patterns on the AVF surface of RC 20005 representative of the peak systolic, mid-diastolic and end-diastolic blood flow volume

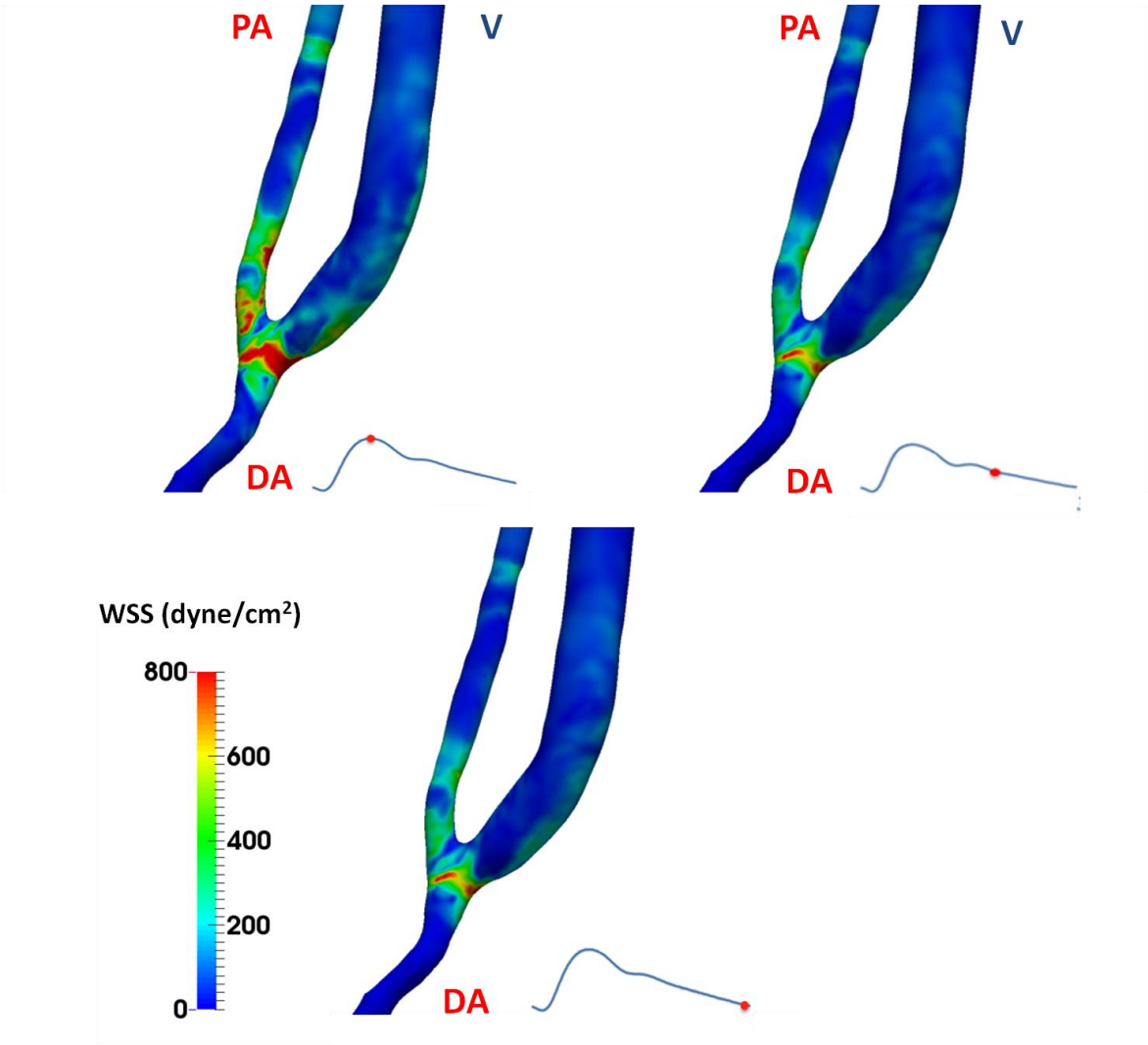

Figure 4.22 WSS pattern on the AVF surface of RC 20009 representative of the peak systolic, mid-diastolic and end-diastolic blood flow volume

4.3.2 Disturbed flow parameters

4.3.2.1 Time averaged WSS (TAWSS)

Plots of TAWSS with a cut-off value of 80 dyne/cm^2, representing the maximum value in the normal arteries [70], are shown for the four simulated AVF in Figure 4.23. Blood flow from the proximal artery is forced to change direction at anastomosis and causes high WSS in this region of the fistula. Areas of low TAWSS are found along the wall of anastomotic floor, near the anastomosis heel on the inner wall of the vein and on the inner wall after the curvature of the vein. Low WSS matches well the sites of flow recirculation and stagnation presented in Figure 4.11 and 4.12.

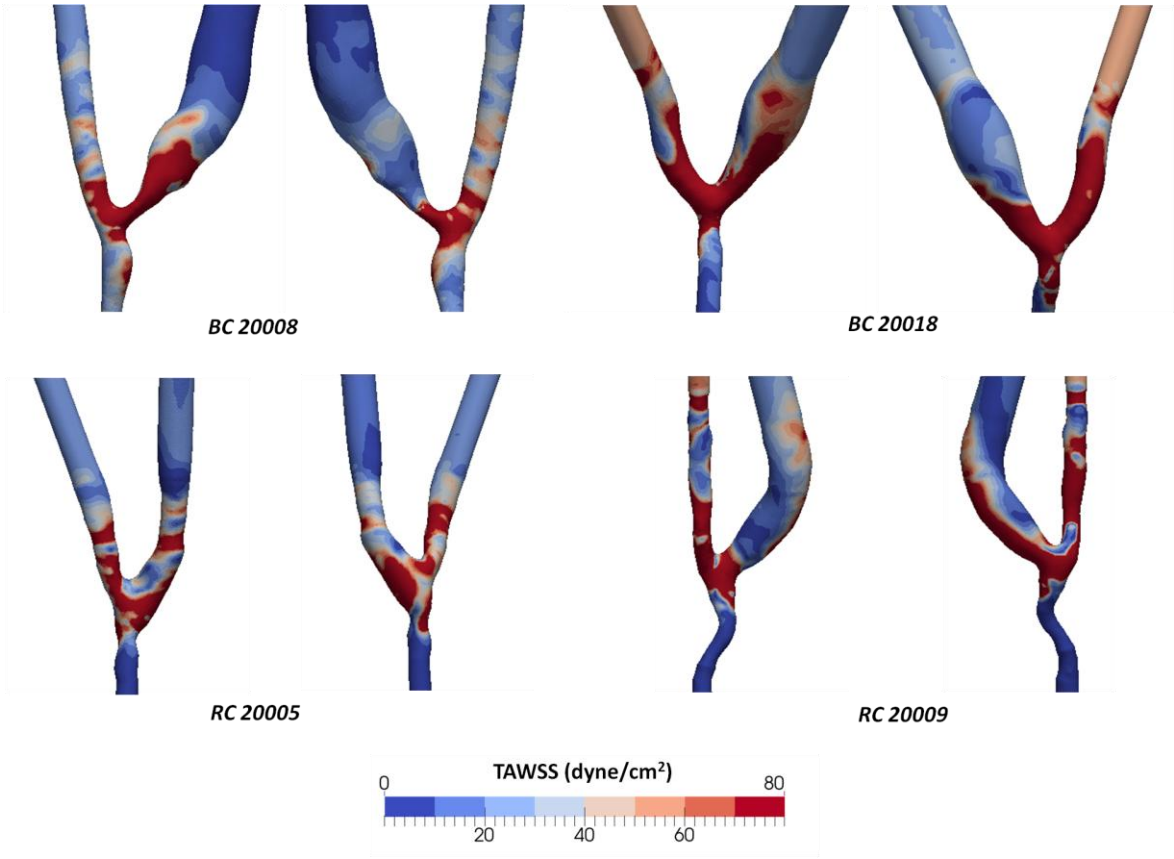

Figure 4.23 TAWSS plots of the four simulated AVF. Models are seen from front (left) and rear side (right)

4.3.2.2 Oscillatory shear index (OSI)

Surface maps of OSI are presented in Figure 4.24: for all the cases, zones of non-null OSI were found on the inner wall of the vein after anastomosis and on the distal artery. High OSI zones, representing reciprocating WSS, are located in the same zones presenting flow instabilities and recirculation described in the previous paragraphs.

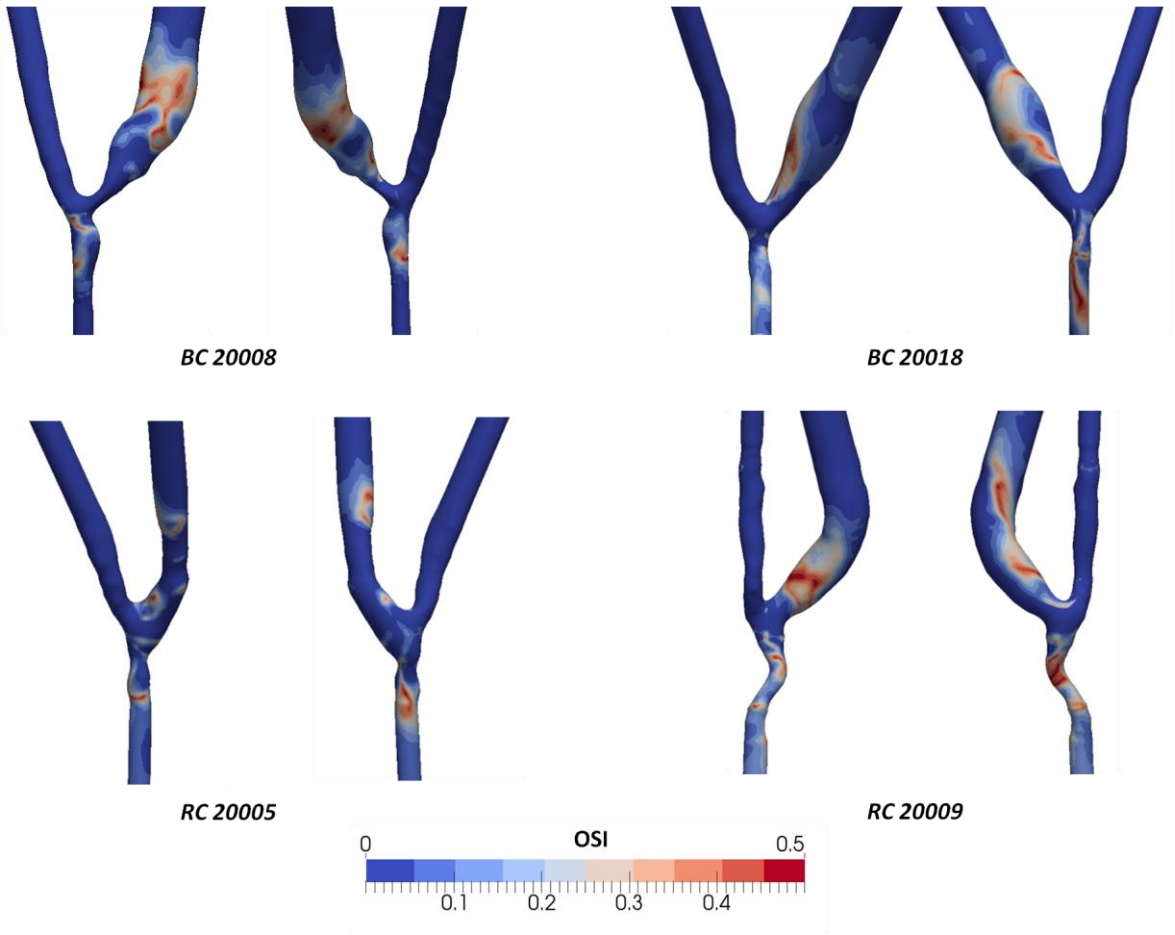

Figure 4.24 Plots of OSI on the AVF surface: front and back side

4.3.2.3 TransWSS components of the WSS vector

Figure 4.25 shows the trends of transWSS, the component of WSS vector perpendicular to the mean direction of the flow, and dirWSS, the component of WSS directed in the mean direction of the flow, in high OSI points on the inner wall of the swing segment. All the simulated AVF have non-zero and oscillating transWSS and dirWSS, representing the instability and the multidirectional nature of the flow near the wall.

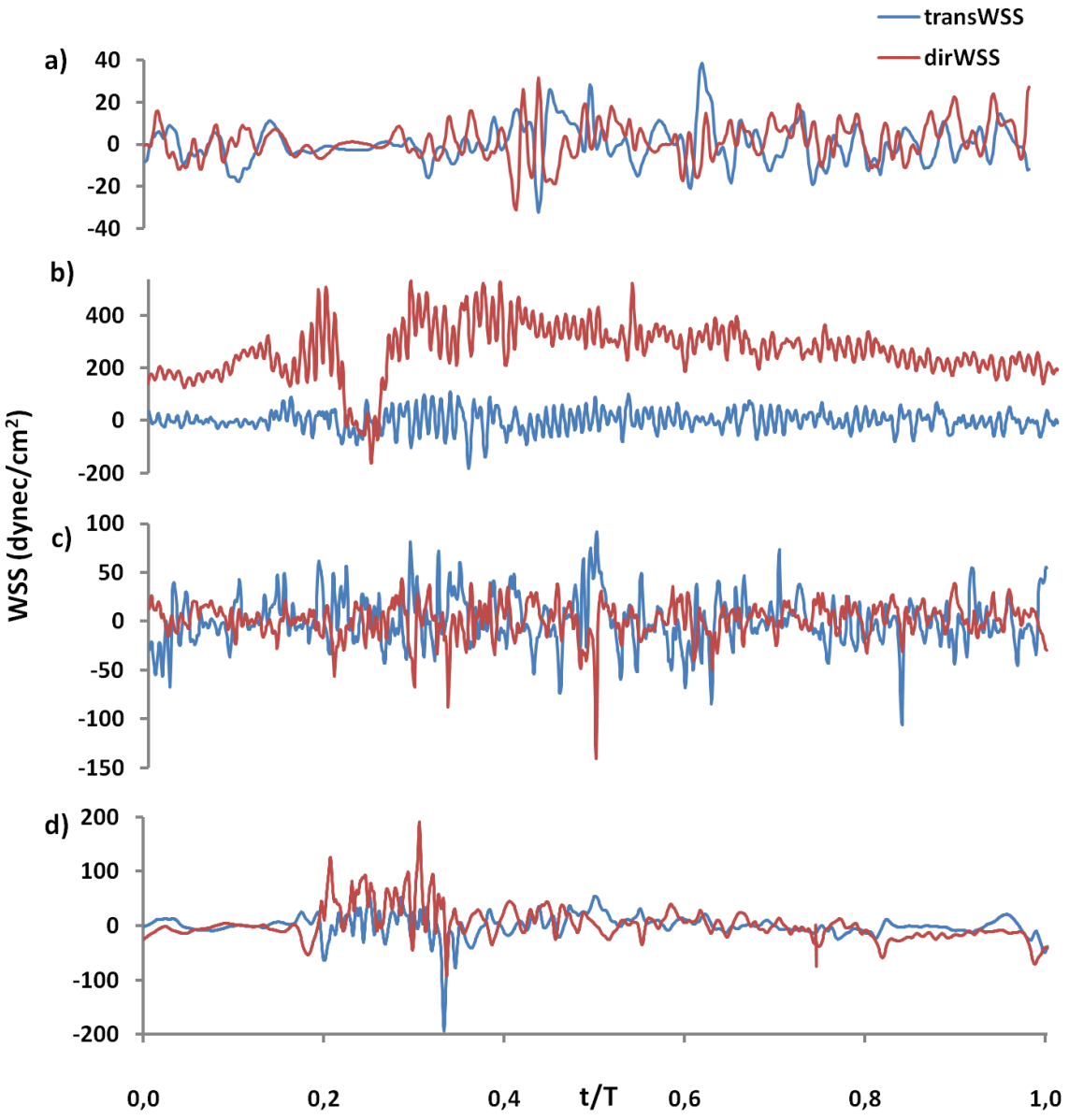

Figure 4.25 Plot of dirWSS and transWSS throughout the cardiac-cycle, representative of the instability of the WSS vector in the four simulated cases: a) BC 20008, b) BC 20018, c) RC 20005 and d) RC 20009

4.3.2.4 Instability index of WSS

A simple comparison between OSI and the *Instability index* represented in Figure 4.26 shows a good correlation between the two indexes, underlining the ability of the second metric to provide more information than OSI regarding zones with oscillating WSS and sudden changes in WSS magnitude.

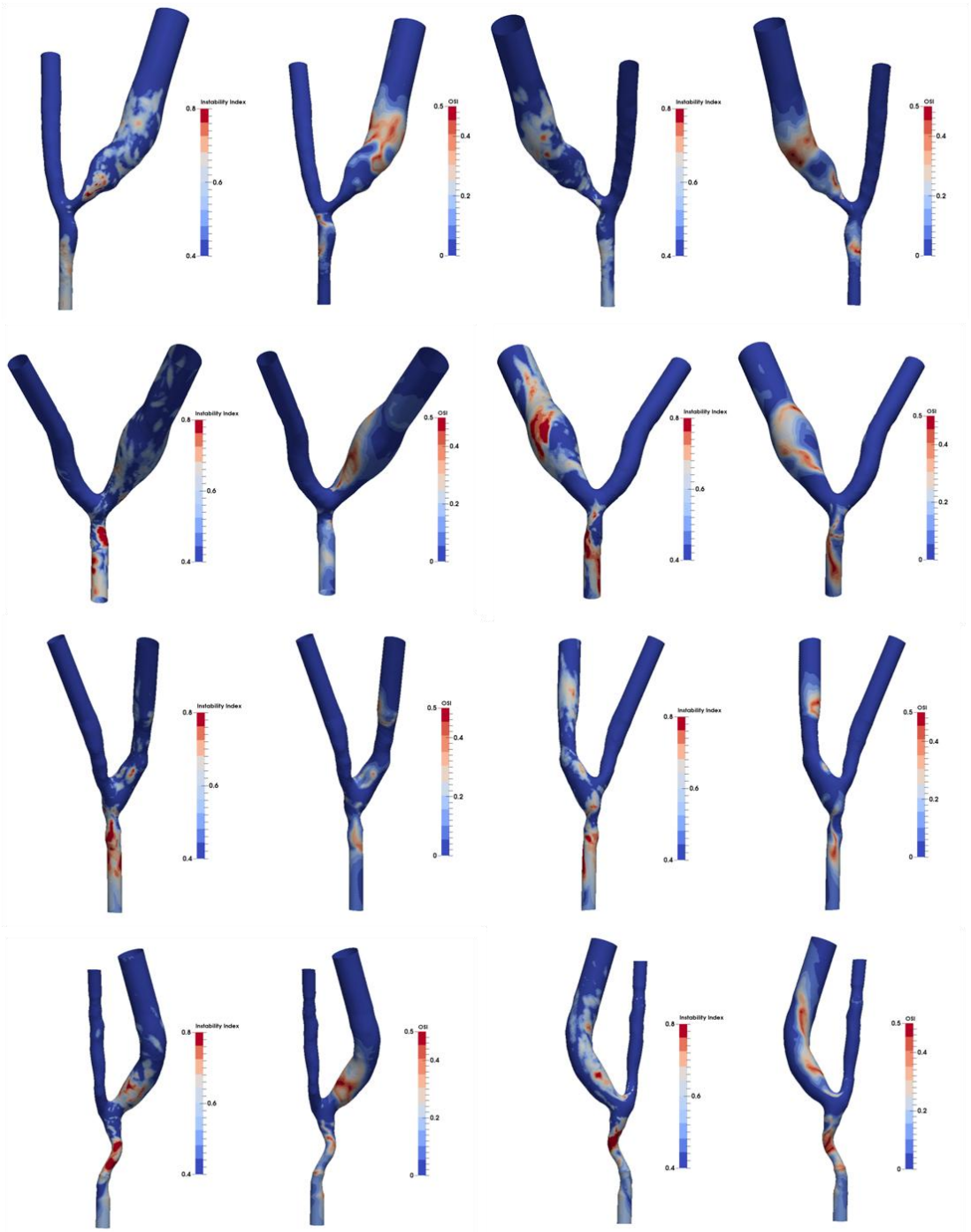

Figure 4.26 Comparison between OSI and Instability Index in simulations

4.3.3 Influence of some parameters on flow instability

4.3.3.1 Mesh density

Figure 4.27 shows TAWSS and OSI of case RC20005 with the initial mesh elements (N=1259417) and the reduced element density (N=503981). Since they reveal no significant differences in the two patterns, they demonstrate the ability of the CFD solver to capture the main flow features also with relatively coarse mesh.

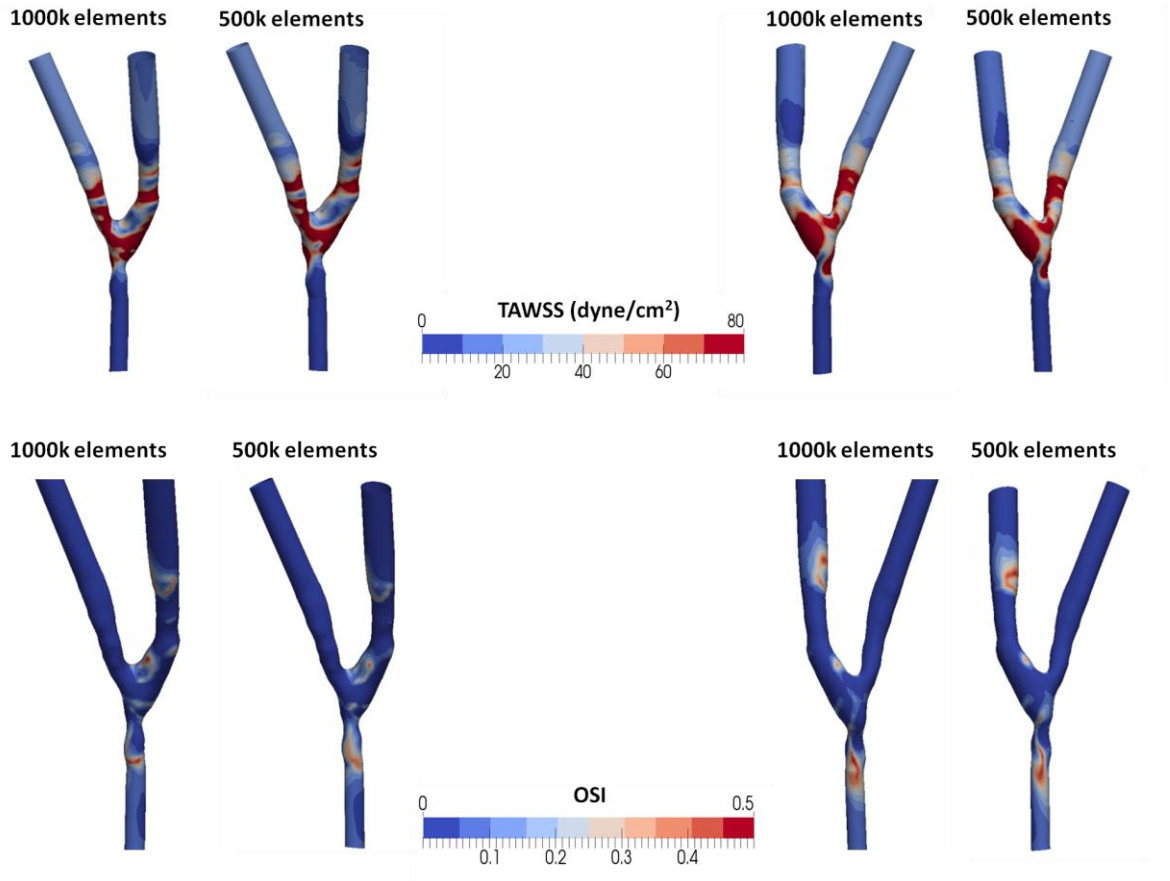

Figure 4.27 Plot of TAWSS and OSI on the AVF RC20005 surface for two with different mesh density

4.3.3.2 Position of the zero-pressure boundary condition

In Figure 4.28 a comparison beetween TAWSS and OSI of the two simulations with different positioning of the zero-pressure boundary condition reveals some differences in the patterns, especially in the OSI. AVF RC20009 simulated with zero-pressure imposed at the outlet of the distal artery shows the presence of a more extended high OSI zone in the distal artery. At the same time the vein presents a less extended OSI area in case of zero-pressure imposed at the outlet of the artery.

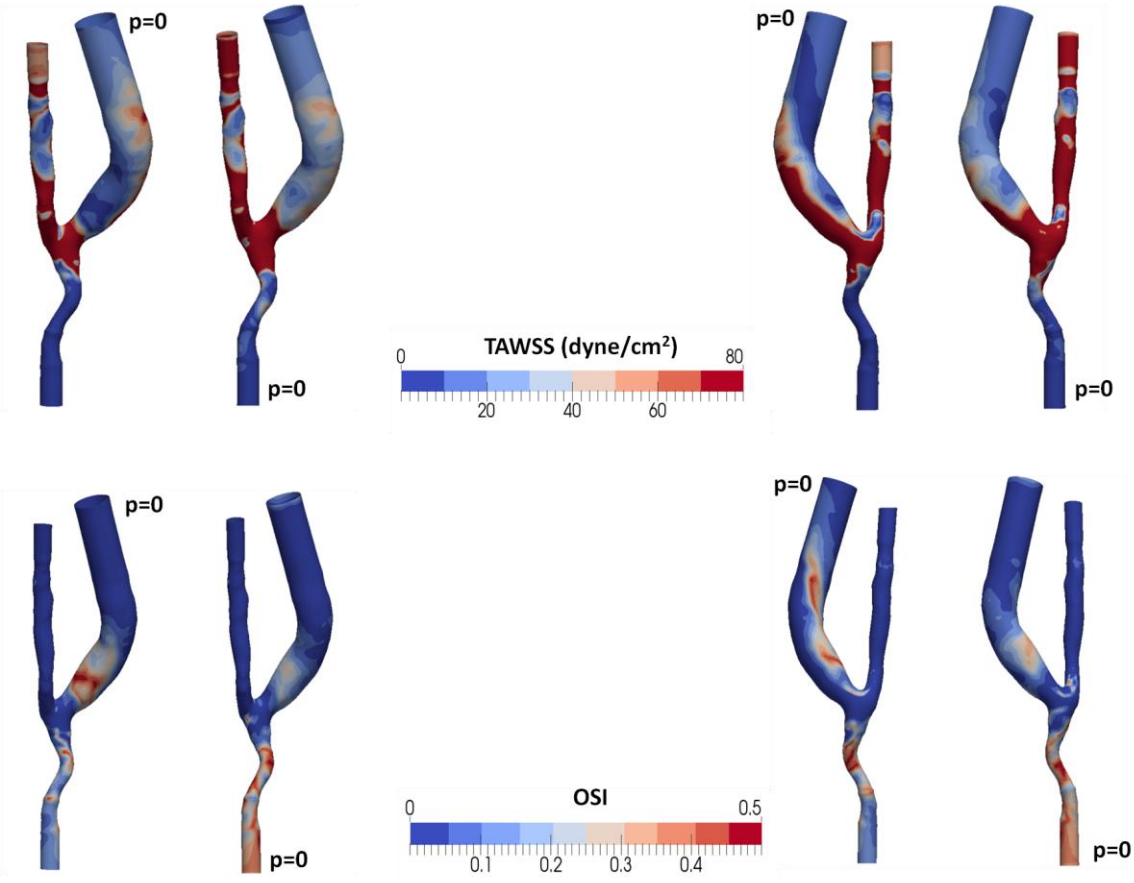

Figure 4.28 Plot of TAWSS and OSI on the AVF RC20009 surface with different position of the pressure boundary condition, revealing some differences in the two patterns

4.3.3.3 Blood volumetric flow rate

Figure 4.29 shows a comparison between the velocity vs. time traces corresponding to different flow rates:

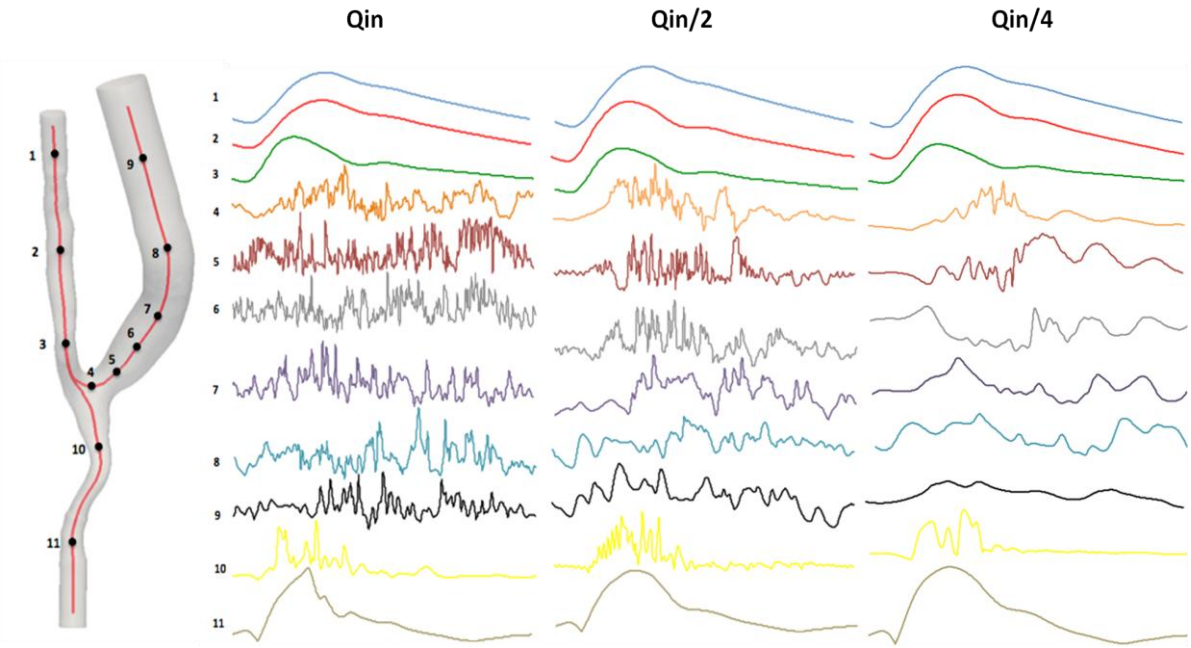

Figure 4.29 Velocity vs. time traces in AVF RC20009 corresponding to Qin, Qin/2 and Qin/4

It appears evident that the high instability of velocity traces taking place in the juxta anastomotic vein was significantly damped by blood flow rate reduction.

Figure 4.30 shows TAWSS of AVF RC20009 simulated with different flow rates. As it was expected a decreasing of the flow rate corresponds to a decreasing of TAWSS in every zones of the AVF:

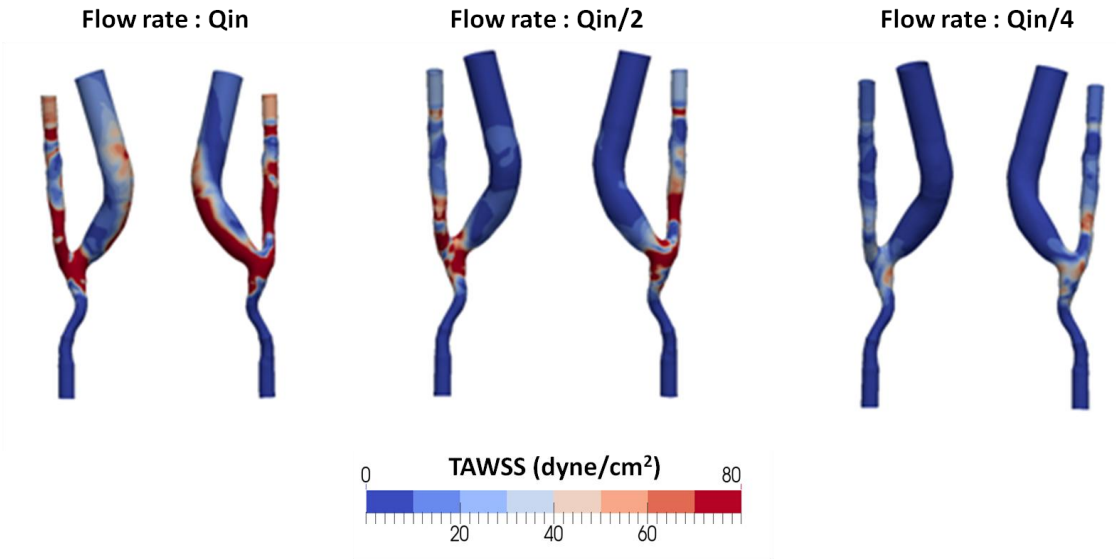

Figure 4.30 Plot of TAWSS on the AVF 20009 surface with fistula flow rate (Qin), halved (Qin/2) and reduced to a quarter (Qin/4)

Figure 4.31 shows the OSI of AVF RC20009 simulated as previously described. A decreasing of flow rate corresponds to a decreasing of OSI, especially on the inner wall of the vein: the high OSI zone (OSI ~ 0.4-0.5) corresponding to Q_{in} turns to a zone of mid-OSI values (OSI ~ 0.2-0.3) in case of halved flow and finally to a null-OSI zone corresponding to $Q_{in}/4$.

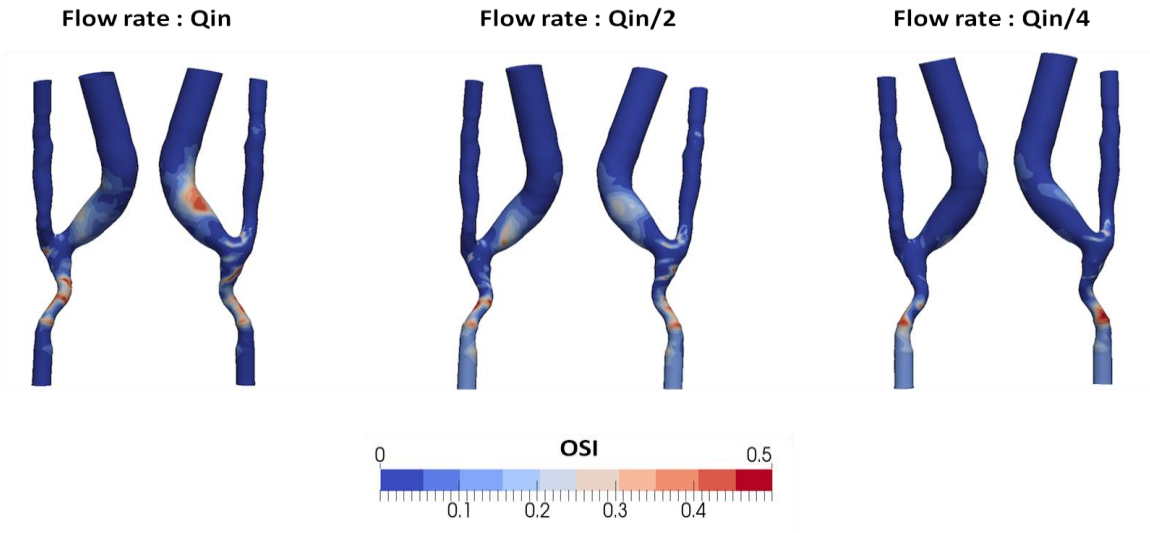

Figure 4.31 Plot of OSI on the AVF 20009 surface with starting flow rate (Qin), halved (Qin/2) and reduced to a quarter (Qin/4)

In order to better understand the trend of WSS, time traces of the magnitude of WSS vectors in some probe points on the wall surface in the proximal artery, in the vein and in the distal artery are shown in Figure 4.32. As expected, a decreasing of WSS magnitude is evident from the initial value that is reduced to a quarter. But the most interesting result is the damping of the oscillation of WSS magnitude in the vein according to the flow decrease.

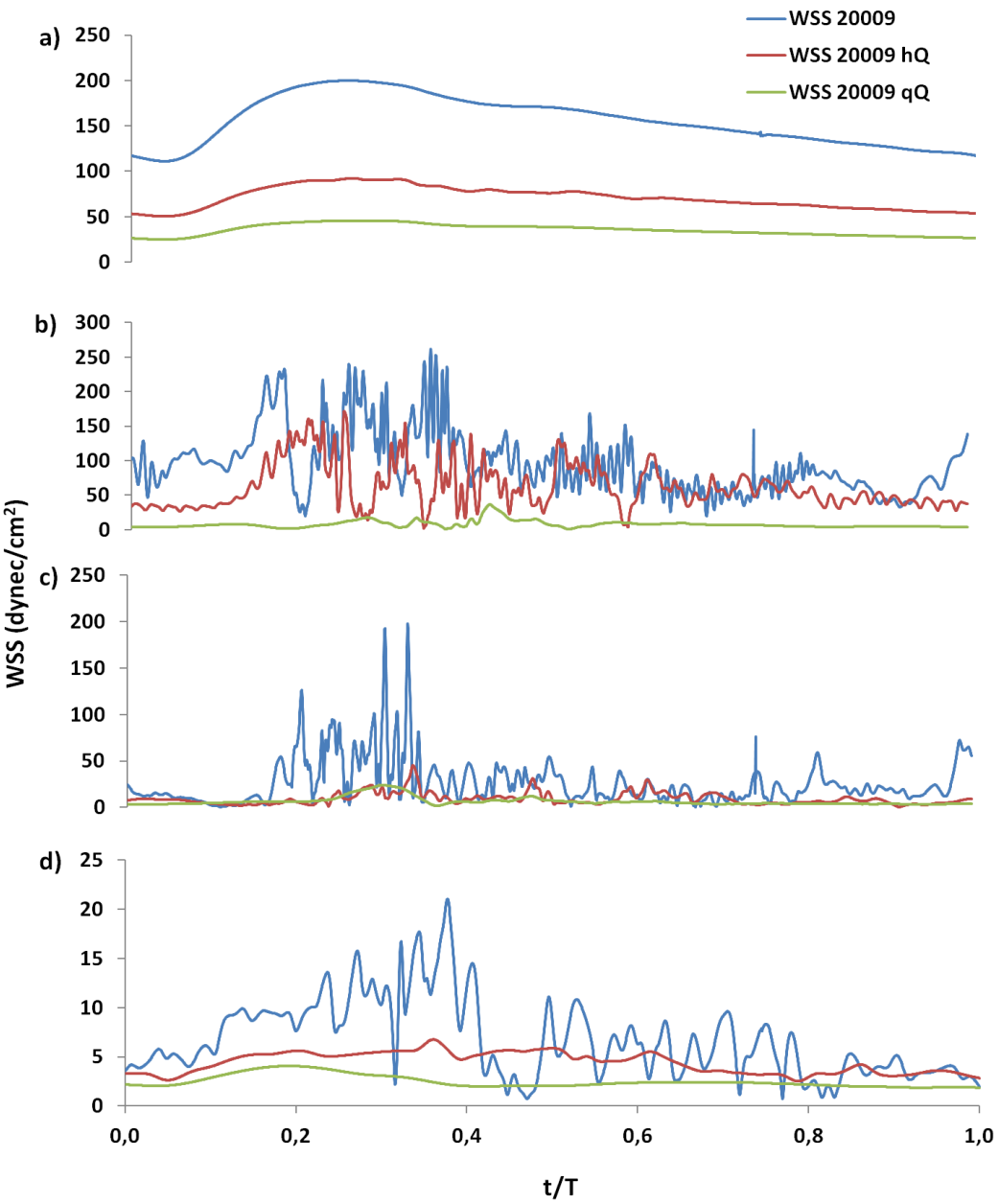

Figure 4.32 Time traces of WSS magnitude on the period in different sites of the RC 20009 AVF: a) proximal artery, b) and c) vein, d) distal artery

5. A comparison with a normal carotid bifurcation

This chapter contains a description of the flow field observed in a normal carotid bifurcation. The attention is focused on the velocity traces, in order to investigate the potential presence of flow instability. Furthermore, the common hemodynamic wall parameters (TAWSS and OSI) previously used to describe regions of disturbed flow in the AVF were also computed.

5.1 The carotid bifurcation: a site of interest

Considering the results of the numerical simulations performed in the AVF, where the blood flow dynamics is greatly influenced by the non physiological condition of the anastomosis between a peripheral artery and a vein segment, it appeared interesting to investigate the flow field and the velocity pattern in a normal carotid bifurcation, a common site for clinically significant atherosclerotic plaque formation. We compared the flow pattern observed in AVF models with the flow pattern of a model obtained from a normal carotid bifurcation, a vascular segment characterized by a complex geometry with high flow rate. The aim was to investigate to which extent transitional flow may develop also in physiological conditions or if it characterizes selectively the AVF. .

5.1.1 Carotid bifurcation anatomy

The common carotid artery (CCA) is a paired structure, meaning that there are two in the body, one for each half. The left and right common carotid arteries follow the same course with the exception of their origin. The right common carotid originates in the neck from the brachiocephalic trunk. The left arises from the aortic arch in the thoracic region. The bifurcation into the external (ECA) and internal (ICA) carotid arteries occurs at the upper border of the thyroid cartilage, at around the level of the fourth cervical vertebra (Figure 5.1).

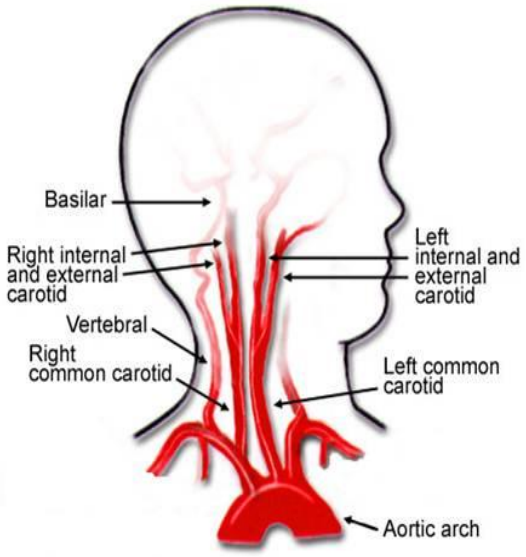

Figure 2.1 Representation of The common carotid arteries branches into internal and external carotid arteries

The average diameter of the common carotid for adult males and females is 6.5 mm and 6.1 mm, respectively [71].

5.2 CFD simulation

The CFD simulation and post-processing of the normal carotid has been performed with the same software used for AVFs and explained in chapter 4. As in case of AVFs it was necessary to reconstruct a carotid 3D model and to set appropriate boundary conditions.

5.2.1 Carotid model

A mesh of left carotid bifurcation with 853,700 elements to be used for the CFD simulation has been obtained starting from a set of MRI images and using the methodology described in chapter 3 (Models reconstruction). As shown in figure 5.1, this model is free from any stenosis or any other pathological evidence.

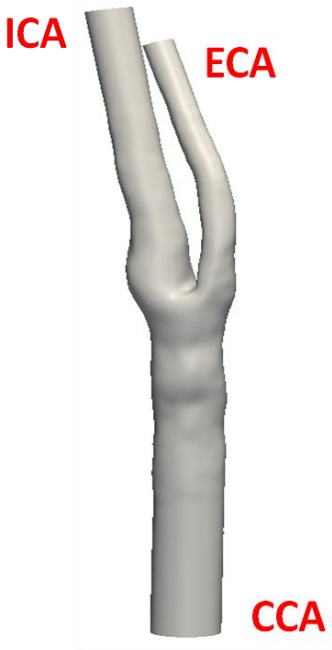

Figure 5.2 Carotid model

5.2.2 Boundary conditions

Few studies have attempted to characterize the volumetric flow rate of dynamics over the cardiac cycle. Lee et al. [72] combined the normal ICA flow waveform of Ford et al. [73] with the time-varying ICA:CCA flow division data of Marshall et al. [74] in order to determine whether investigations of local risk factors in atherosclerosis can rely geometric markers of disturbed flow. In order to characterize the flow field in the normal carotid bifurcation it was reasonable to use the same curves, shown in Figure 5.3.

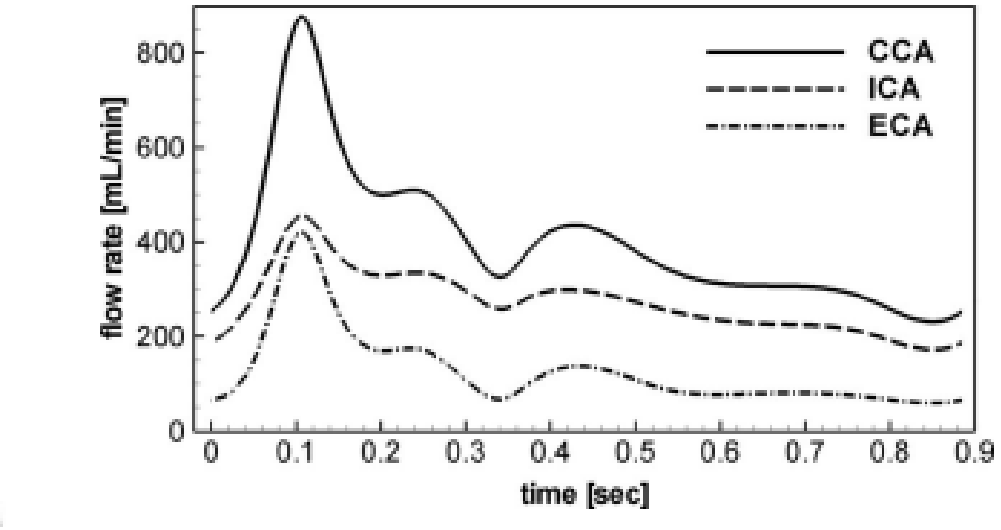

Figura 5.3 Flow rate waveforms corresponding to average CCA, ICA and ECA [72]

With the aim of maintaining boundary conditions similar to those used for the AVFs, flow rate boundary conditions were imposed on the inlet CCA and the outlet ICA, and zero-pressure boundary condition has been imposed on the ECA.

5.2.3 CFD results

5.2.3.1 2D and 3D streamlines

Figure 5.4 shows 2D and 3D velocity streamlines representative of the peak systolic flow rate: they reveal laminar flow in the whole carotid bifurcation, even in the region where the flow coming from the CCA has to split into the ECA and ICA.

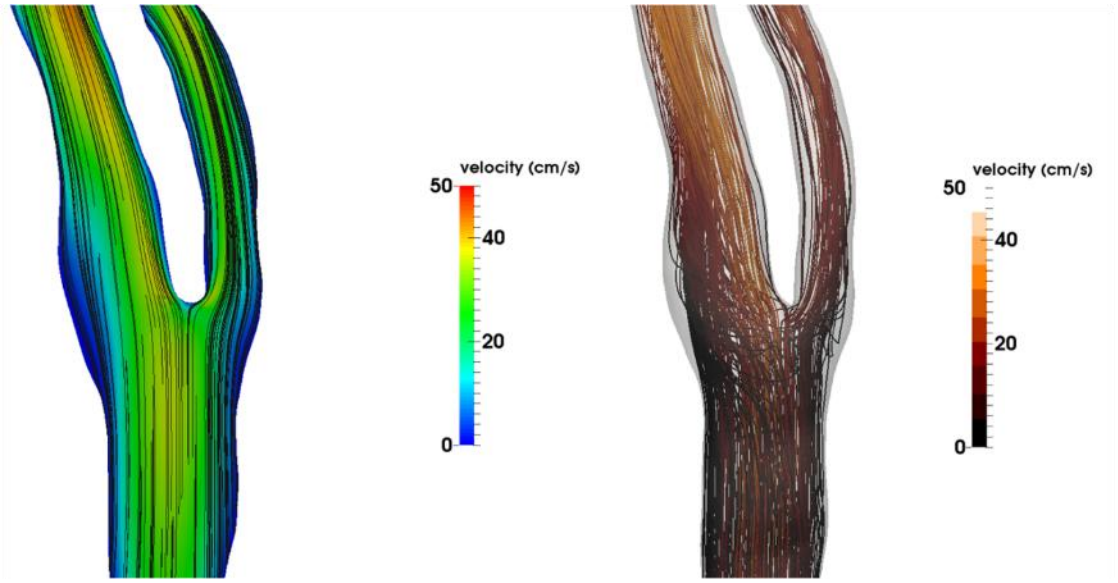

Figure 5.4 Velocity 2D streamlines (left) and velocity 3D streamlines (right), both representative of the peak systolic blood flow volume instance

5.2.3.2 Velocity traces

As previously performed for the AVFs, we described the trend of velocity in some feature points identified along the centerline of the carotid model. Figure 5.5 shows the velocity, normalized by its cycle-averages, at the selected feature points. As expected, the presence of laminar flow in every region of the carotid was confirmed by the CFD simulation, ruling out any presence of flow instability.

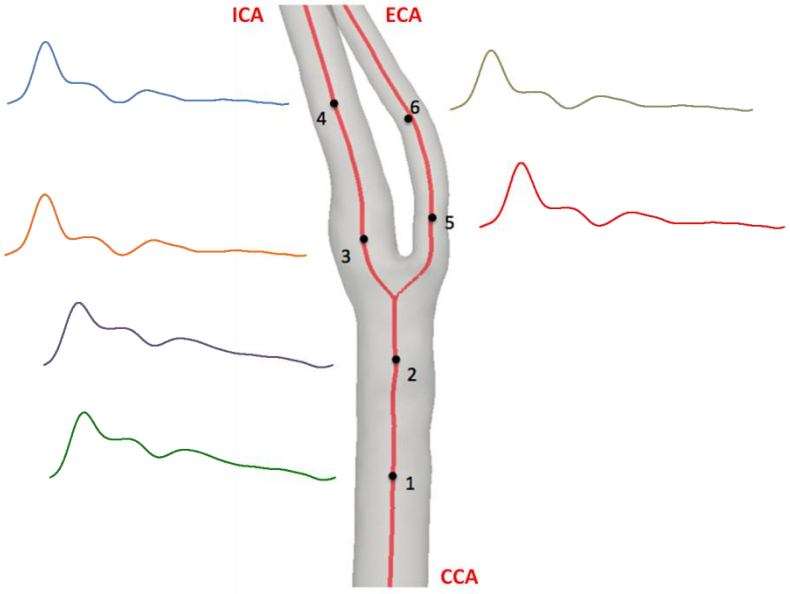

Figure 5.5 Velocity vs. time traces, normalized by their respective cycle averages, at selected probe points of the carotid model

5.2.3.3 Disturbed flow parameters

Figure 5.6 shows the plot of TAWSS and OSI of the carotid model. High values of TAWSS can be observed at the bifurcation, where the flow splits, whil the high OSI region was concentrated around the outer walls of the ICA, in line with the results of Lee et al. [72] and Hyun et al. [75]

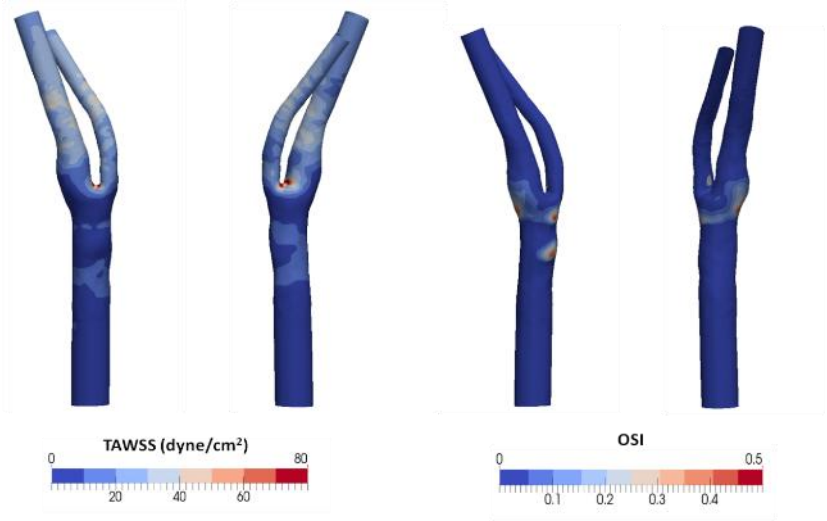

Figure 5.6 Plot of TAWSS and OSI on the carotid surface

6. Discussion, limitations and future perspectives

This final chapter contains the discussion of the results of the present thesis, the limits of the computational work and possible future developments and perspectives of this research study field.

6.1 Discussion

In the present thesis, by employing pulsatile CFD simulations in patient-specific models, it was possible to describe the nature of the disturbed flow, with focus on flow instability.
In all simulated cases, transitional laminar-to-turbulent flow developing in the juxta-anastomotic vein and along the distal artery was observed. Both 2D and 3D velocity streamlines revealed laminar flow in the proximal artery and secondary flows and local vortexes in the venous and distal artery segment. Marie et al. [76] found spiral laminar flow (SLF), within the vein segment above the swing segment, whereas in the swing segment had chaotic characteristics consistent with turbulence, in line with our findings. Velocity traces revealed instability right after the anastomosis that damped moving towards the distal vein, or by decreased flow rate. Valen-Sendstad et al. [77]found similar velocity traces in the carotid siphon: a study focused on five internal carotid artery aneurisms revealed flow instabilities, with strong periodic vortexes shedding at a frequency of 100 Hz. The oscillations of the velocity vectors in the AVF result in low and reciprocating WSS on the inner surface of the juxta-anastomotic segment and on the distal artery, in line with previous patient-specific studies [45], [50], [49]. The increase in flow complexity in the vein was also described using isosurfaces and $\lambda 2$ criterion for vorticity, in line with a similar study on side-to-end AVF by McGah et al. [78].

Maps of TAWSS and OSI as indicators of disturbed flow were obtained in all AVF models, with localizations as demonstrated in the previous thesis work by Semperboni [53]; their patterns confirmed also the correspondence to the locations of *in vivo* stenoses detected by Sivanesan et al. [27].

By studying which parameters may affect the transition from turbulence to laminar flow, i.e. mesh density, position of zero-pressure boundary condition and volumetric flow rates on CFD results, we have found that the most important one was the reducing of the flow rate. In fact, this was an expected finding, since blood flow reduction corresponds to a proportional reduction of the Reynolds number [77]. Moreover, the disturbed flow zones (high OSI) diminished accordingly and the high instability of both velocity and WSS traces showed a significant damping.

A comparison CFD study performed on a normal carotid bifurcation, revealing laminar flow in all the regions of the model, led to the conclusion that the flow instability found in the AVF is not observed in such a vascular district, at least for physiological flow and absence of stenosis. Considering the study of Lee et al. [79] that demonstrated transitional or weakly turbulent state in a stenosed carotid bifurcation, with rapid velocity and pressure fluctuations in the post-stenotic region of the ICA, it should be underlined the similarity between AVF and carotid bifurcation in their geometry, but also their distance in the flow pattern.

6.2 Limitations

Some limitations, inherent to our CFD numerical simulations, require acknowledgement and further examination:

- *Newtonian rheology model for the blood*. For most large arteries under normal and fully-developed flow conditions, the Newtonian approximation is widely justified, but non-Newtonian effects can become non-negligible in large and persistent recirculation zones, and hence persistent low WSS. For aneurisms Rayz et al. [80] have convincingly demonstrated that regions of stagnant flow predicted by a non-Newtonian CFD model matched the subsequently observed distribution of thrombus better than that predicted by a Newtonian rheological model. In fact, it has been observed that the Newtonian model yields WSS even 30% lesser than the WSS obtained using a non-Newtonian model [81]. In contrast to this findings, Chen et al. [82] found that WSS calculated using a Newtonian model is consistent with the data obtained using a non-Newtonian model and the pattern of the OSI of the Newtonian model compare well to that of the non-Newtonian model.

- *Rigid walls.* This assumption widely discussed by Ambrosi et al. [83] removes the effects that the compliance of vascular vessels has on flow and WSS. It has been demonstrated that the mean velocities will be necessarily overestimated of 20%, as well as maximal velocity, pressure and WSS are overestimated. Hence, the use of rigid walls models, while undoubtedly convenient and justified in many cases, should not overlook the fact that real vessels are influenced by the effect of the

compliance. For cases where the compliance and vessel motion are known to have non-negligible quantitative or qualitative effects, a popular modeling approach is fluid structure interaction (FSI). In this order of ideas, it has to be considered that in patient-specific studies, uncertainties in data needed to model the effects of compliance may mask any perceived benefit in doing this [84], especially in light of the extra conceptual and computational effort required in including the effect of compliance. Furthermore, McGah et al. [85] determined that rigid-walls hemodynamic simulations can predict blood hemodynamics within the same order of accuracy of the FSI equivalent simulations, justifying our rigid-walls assumption.

- *Zero-pressure boundary condition*. Many CFD studies typically use a zero outlet pressure condition: in the present thesis this condition was assigned to the outlet of the cephalic vein. As this boundary condition is likely to produce different results compare to clinical measurements, new methods have been proposed in the last years: Lee et al. [86] introduced the minimum energy loss method (MEL), while Vignon-Clementel et al. [87] proposed an alternative approach coupling the solution at the outflow boundaries of the modeled domain with lumped parameter. These alternative solutions are worthy of attention and could represent a future development of the solver.

6.3 Future developments and perspectives

In this study transitional flow developing in the juxta-anastomotic vein has been observed in all AVF cases. The oscillations of the velocity vectors in these areas result in eddies that rotates also the WSS. On these sites, the development of both oscillating and multi-directional disturbed flow may sum together to boost the neointima formation in the newly created AVF.

On the basis of this hypothesis, two main future developments could be imagined:

- Investigation of the flow status by using an electronic stethoscope (3M Littmann) for AVF sound recording, followed by software analysis by using waveform decomposition, principle component analysis (PCA) and sequential forward selection algorithm. Previous studies [88], [89]indicated that stethoscope waveform analysis can detect sound features associated with the change from laminar flow to turbulent flow downstream the site of vascular stenosis. As VA angiographic studies are expensive and invasive and diagnostic accuracy of color duplex ultrasound in AVF stenosis is not always available when decreased flow occurs, auscultation seems to be a simple monitoring method to assess the VA.

- Realization of a device that can impose flow and velocity patterns resulting from CFD simulations to the EC. Davies et al. [90]exposed ECs to a turbulent flow, even with low WSS magnitude. Also Fry et al. [91] and Prado et al. [92] found that the EC in the turbulent region were non-directional and neointimal plaques were focally distributed, by exposing EC to velocity and WSS patterns that are phenotipically similar to those presented in this thesis.

Appendix A: Gnuid input file

```
n_velocity_boundaries = 2

[vel_bc_00]
inlet_outlet = inlet

vel_bc_id = 4

vel_bc_radius = 0.235608

vel_bc_center_x = -1.551855
vel_bc_center_y = 10.16657
vel_bc_center_z = 23.813856

vel_bc_normal_i = 0.112114
vel_bc_normal_j = -0.989572
vel_bc_normal_k = 0.090433

scaling = 1

n_fourier_modes = 12
f_mode_00_re = 1.0000000000
f_mode_00_im = 0.0000000000
f_mode_01_re = -0.0327052203
f_mode_01_im = -0.0577697276
f_mode_02_re = -0.0324478191
f_mode_02_im = -0.0147872814
f_mode_03_re = -0.0236304161
f_mode_03_im = 0.0085815818
f_mode_04_re = -0.0049958551
```

f_mode_04_im = 0.0108118724
f_mode_05_re = -0.0080643808
f_mode_05_im = 0.0124268401
f_mode_06_re = 0.0100203587
f_mode_06_im = 0.0080419510
f_mode_07_re = 0.0041600047
f_mode_07_im = 0.0006345681
f_mode_08_re = 0.0029341826
f_mode_08_im = 0.0001981528
f_mode_09_re = 0.0021755798
f_mode_09_im = -0.0007666003
f_mode_10_re = 0.0008200681
f_mode_10_im = -0.0006050539
f_mode_11_re = 0.0000208262
f_mode_11_im = 0.0000888773
[]

[vel_bc_01]
inlet_outlet = outlet

vel_bc_id = 3

vel_bc_radius = 0.164437

vel_bc_center_x = -1.377888
vel_bc_center_y = 16.397295
vel_bc_center_z = 22.246185

vel_bc_normal_i = 0.332830
vel_bc_normal_j = 0.865509
vel_bc_normal_k = -0.374324
scaling = 0.26

n_fourier_modes = 12
f_mode_00_re = 1.0000000000
f_mode_00_im = 0.0000000000
f_mode_01_re = 0.1166700534
f_mode_01_im = -0.6998140808
f_mode_02_re = -0.4201689420
f_mode_02_im = -0.2974540939
f_mode_03_re = -0.3129639900
f_mode_03_im = 0.1708842696
f_mode_04_re = -0.0123036921
f_mode_04_im = 0.1471100201
f_mode_05_re = -0.0215912956
f_mode_05_im = 0.1630703528
f_mode_06_re = 0.1251372931
f_mode_06_im = 0.0269716257
f_mode_07_re = 0.0384073719
f_mode_07_im = -0.0113264565
f_mode_08_re = 0.0266105449
f_mode_08_im = -0.0094827310
f_mode_09_re = 0.0171643495
f_mode_09_im = -0.0163584822
f_mode_10_re = 0.005137788
f_mode_10_im = -0.0098112885
f_mode_11_re = 0.0007573098
f_mode_11_im = 0.0004789546
[]

n_pressure_boundaries = 1

[press_bc_00]
press_bc_id = 2
[]

```
mass_flow = 7.35

Re_number = 0

wall_id = 1

penalty = 4.

density = 1.05      # [g/cm3]

viscosity = 0.027    # [poise]

dt = 0.001      # [s]

velocity_approximation_order = 1

pressure_approximation_order = 1

first_to_second_order_mesh = false

step = 0            # !=0 when restarting a simulation

time = 0.           # !=0 when restarting a simulation, time = step * dt

period = 0.91

n_timesteps = 1820

linear_solver_maximum_iterations = 4000

linear_solver_tolerance = 1.e-8
```

```
nonlinear_solver_maximum_iterations = 10

nonlinear_solver_tolerance = 1.e-1

n_uniform_refinement_steps = 0

n_steps_between_solution_output = 1

n_steps_between_equation_system_output = 50

second_order_start_step = 20

n_washin_steps = 2

read_es_file = false

mesh_file = ./mesh.xda

es_file = ./gnuid_test.xdr

write_continuous = true

write_discontinuous = false
```

BIBLIOGRAPHY

[1] Lauder A, Schieppati A, Conte F, Remuzzi G. Batlle.D: Low mortality and key aspects of delivery of care for end-stage renal disease in Italy. Scientic World Journal 9: 349- 359. 2009

[2] Registro italiano di dialisi e trapianto (RIDT): Report 2010. **http://www.sinidt.org/web/procedure/protocollo.cfm**

[3] National Kidney Foundation. K/DOQI clinical practice guidelines for chronic kidney disease: evaluation, classification, and stratification. American Journal of Kidney Diseases. vol 38: Suppl 1, S1-S266, 2002

[4] Fresenius Medical Care. ESRD Patients in 2012. A global perspective, 2012. **http://www.fmc-ag.com**

[5] Abel JJ, Rowntree LG Turner BB: On the Removal of Diffusible Substances from the Circulating Blood of Living Animals. Dialysis. J. Pharmacol. & Exper. Therap. 11: 275-316, 1914

[6] Kolff WJ: Dialysis in treatment of uremia: artificial kidney and peritoneal lavage. Archives of Internal Medicine, 94.1: 142-160, 1954

[7] Quinton W, Dillard D, Scribner BH: Cannulation of blood vessels for prolonged hemodialysis. Trans Am Soc Artif Intern Organs, 6: 104-113, 1960

[8] Brescia MJ, Cimino JE, Appel K, Hurwich BJ: Chronic Hemodialysis Using Venipuncture and a Surgically Created Arteriovenous Fistula. The New England Journal of Medicine, 275: 1089-1092, 1966

[9] Sperling M, Kleinschmidt W, Wilhelm A, HeidlandA, Klutsch K: Die subkutane arteriovenose Fistel zur intermittierenden Hamodialyse-Behandlung. Dtsch Med Wschr, 92: 425-426, 1967;

[10] Konner K: History of vascular access for haemodialysis. Nephrol Dial Transplant, 20: 2629-2635, 2005

[11] Konner K: Interventional Nephrology and Dialysis: The Initial Creation of Native Arteriovenous Fistulas: Surgical Aspects and Their Impact on the Practice of Nephrology. In: Seminars in dialysis. Vol. 16. 4: 291-298, 2003

[12] National Kidney Foundation: KDOQI Clinical Practice Guidelines and ClinicalPractice Recommendations for 2006 Updates: Hemodialysis Adequacy, Peritoneal Dialysis Adequacy and Vascular Access. Am J Kidney Dis 48(1): 1-322, 2006

[13] NKF-K/DOQI Clinical practice guidelines for vascular access. Am J Kidney Dis, 48 Suppl 1: S176-247, 2011

[14] Centers for Medicare and Medicaid Services: 2010 annual report: End-stage renal disease clinical performance measures project. Am J Kidney Dis, 46: 1 –100, 2011

[15] KDOQI clinical practice guidelines and clinical practice recommendations for vascular access 2009. Am J Kidney Dis, 48 Suppl 1: Suppl. 1: 176 –S322, 2009

[16] National Kidney Foundation: KDOQI Clinical Practice Guidelines and Clinical Practice Recommendations for 2006 Updates: Hemodialysis Adequacy, Peritoneal Dialysis Adequacy and Vascular Access. J Kidney Dis 48.Suppl 1: 1-322, 2006

[17] Tordoir J, Canaud B, Haage P, Konner K, Basci A, Fouque D, Kooman J, Martin-Malo A, Pedrini L, Pizzarelli F, Tattersall J, Vennegoor M, Wanner C, ter Wee P, Vanholder R.: EBPG on vascular access. Nephrology Dialysis Transplantation 22. Suppl 2: ii88-ii117, 2007

[18] Caroli A, Manini S, Antiga L, Passera K, Ene-Iordache B, Rota S, Remuzzi G, Bode A, Leerrmakers J, van de Vosse FN, Vanholder R, Malovrh M, Tordoir J and Remuzzi A: Validation of a patient-specific hemodynamic computational model for surgical planning of vascular access in hemodialysis patients. Kidney Int, 84(6):1237-45, 2013

[19] Al-Jaishi AA, Oliver MJ, Thomas SM, Lok CE , Zhang JC, Garg AX, Kosa SD, Quinn RR, Moist LM: Patency rates of the arteriovenous fistula for hemodialysis: a systematic review and meta-analysis. Am J Kidney Dis, 63(3):464-78, 2014

[20] Majesky MW, Dong XR, Regan JN, Hoglund VJ: Vascular smooth muscle progenitor cells: building and repairing blood vessels. Circ Res, 108: 365–377, 2011

[21] Mitra AK, Gangahar DM, Agrawal DK: Cellular, molecular and immunological mechanisms in the pathophysiology of vein graft intimal hyperplasia. Immunology and cell biology, 84.2: 115-124, 2006

[22] Chiu JJ, Chien S: Effects of disturbed flow on vascular endothelium: athophysiological basis and clinical perspectives. Physiol Rev 91: 327-387, 2011

[23] Majesky MW, Dong XR, Hoglund V, Daum G, William M. Mahoney WM Jr: The Adventitia: A Progenitor Cell Niche for the Vessel Wall. Cells Tissues Organs, 195: 73–81, 2011

[24] Lee T, Chauhan V, Krishnamoorthy M, Wang Y, Arend L, Mistry MJ, El-Khatib M, Banerjee R, Munda R, Roy-Chaudhury P: Severe venous neointimal hyperplasia prior to dialysis access surgery, 26: 2264-70, 2011

[25] Kim YO, Song HC, Yoon SA, Yang CW, Kim NI, Choi YJ, Lee EJ, Kim WY, Chang YS, Bang BK: Preexisting intimal hyperplasia of radial artery is associated with early failure of radiocephalic arteriovenous fistula in hemodialysis patients, 41: 422-428, 2003

[26] Allon M, Litovsky S, Young CJ, Deierhoi MH, Goodman J, Hanaway M, Lockhart ME, Robbin ML: Medial fibrosis, vascular calcification, intimal hyperplasia, and arteriovenous fistula maturation, 58(3): 437-43, 2011

[27] Sivanesan S, How TV, Bakran A: Sites of stenosis in AV stulae for haemodialysis access. Nephrology Dialysis Transplantation 14(1): 118-120, 1999

[28] Asif A, Gadalean FN, Merrill D, Cherla G, Cipleu CD, Elpstein DL, Roth D: Inflow stenosis in arteriovenous fistulas and grafts: multicenter, prospective study. Kidney International. 67: 1986–1992, 2005

[29] Maya ID and Allon M: Vascular access: Core curriculum 2008. Am J Kid Dis, 51:702-708, 2008

[30] Roy-Chaudhury P, Sukhatme VP, Cheung AK: Hemodialysis Vascular Access Dysfunction: A Cellular and Molecular Viewpoint. Journal of American Society of Nephrology, 17: 1112-1127, 2006

[31] Roy-Chaudhury P, Wang Y, Krishnamoorthy M, Zhang J, Banerjee R, Munda R, Heffelfinger S,Arend L. Cellular phenotypes in human stenotic lesions from haemodialysis vascular access. Nephrol Dial Transplant. 24(9): 2786–2791, 2009

[32] Roy-Chaudhury P, Arend L, Zhang J: Neointimal hyperplasia in early arteriovenous fistula failure. Am J Kidney Dis. 50: 782–790, 2007

[33] Schwab SJ, Oliver MJ, Suhocki P, McCann R: Hemodialysis arteriovenous access: detection of stenosis and response to treatment by vascular access blood flow. Kidney Int 59: 358-362, 2001

[34] Kim YO, Yang CW, Yoon SA, Yoon SA, Chun KA Kim NI, Park JS, Kim BS, Kim YS, Chang YS, Bang BK: Access blood flow as a predictor of early

failures of native arteriovenous fistulas in hemodialysis patients. Am J Nephrol, 21(3): 221-5, 2001

[35] Pries AR, Reglin B e Secomb TW: Remodeling of Blood Vessels Responses of Diameter and Wall Thickness to Hemodynamic and Metabolic Stimuli Hypertension, 46.4: 725-731, 2005

[36] Giddens DP, Zarins CK, Glagov S: The role of fluid mechanics in the localization of and detection of atherosclerosis. Journal of Biomechanics Engineering, 115: 588-594, 1993

[37] Corpataux JM, Haesler E, Silacci P,Ris HB, Hayoz D: Low-pressure environment and remodelling of the forearm vein in Brescia-Cimino haemodialysis access. Nephrol Dial Transplant, 17(6):1057-62, 2002

[38] Davies PF: Hemodynamic shear stress and the endothelium in cardiovascular pathophysiology. Nat Clin Pract Cardiovasc Med, 6: 16-26, 2009

[39] Dai G, Kaazempur-Mofrad MR, Natarajan S, Zhang Y, Vaughn S, Blackman BR, Garcia-Cardena G, Gimbrone MA Jr: Distinct endothelial phenotypes evoked by arterial waveforms derived from atherosclerosis-susceptible and-resistant regions of human vasculature. Proceedings of the National Academy of Sciences of the United States of America 101. 41: 14871-14876, 2004

[40] Bussolari SR., Dewey CF, Gimbrone MA Jr: Apparatus for subjecting living cells to fluid shear stress. Rev Sci Instrum. 53: 1851-1854, 1982

[41] Dewey CF, Bussolari S R, Gimbrone MA, Davies PF. The dynamic response of vascular endothelial cells to fluid shear stress. J. Biomech. Eng.103**:** 177-185, 1981

[42] Cunningham KS, Gotlieb AI, The role of shear stress in the pathogenesis of atherosclerosis. Lab Invest, 85: 9-23, 2005

[43] Morinaga K, Okadome K, Kuroki M, Miyazaki T, Muto Y, Inokuchi K: Effect of wall shear stress on intimal thickening of arterially transplanted autogenous veins in dogs. Journal of Vascular Surgery: 2(3): 430-433, 1985

[44] Krishnamoorthy M, Roy-Chaudhury P, Wang Y, Sinha AR, Zhang J , Khoury S Munda R, Bane R: Measurement of hemodynamic and anatomic parameters in a swine arteriovenous fistula model The Journal of Vascular Access, 9: 28-34, 2008

[45] Gimbrone MA Jr, Garcia-Cardena G: Vascular endothelium, hemodynamics and pathobiology of atherosclerosis. Cardiovasc Path, 22: 9-15, 2013

[46] Krueger U, Zanow J, Sholza H. Computational fluid dynamics and vascular access. Artificial Organs, 26: 571-575, 2002

[47] Kharbountly Z, Fenech M, Treutenaere JM, Claude I, Legallais C: Investigations into the relationship between hemodynamics and vascular alterations in an established arteriovenous fistula, 29: 999-1007, 2007

[48] Kharboutly Z, Deplano V, Bertrand E, Legallais C. Numerical and experimental study of blood flow through a patient-specific arteriovenous fistula used for hemodialysis. Med Eng Phys, 32: 111-118

[49] Ene-Iordache B, Mosconi L, Remuzzi G, Remuzzi A: Computational fluid dynamics of a vascular access case for hemodialysis. J Biomech Eng, 123: 284-292, 2001

[50] Carroll GT, McGloughlin TM, Burke PE, Egan M, Wallis F, Walsh MT: Wall shear stresses remain elevated in mature arteriovenous fistulas: a case study. J Biomech Eng, 133(2): 021003 , 2011

[51] Ene-Iordache B &Remuzzi A: Disturbed flow in radial-cephalic arteriovenous fistulae for haemodialysis: low and oscillating shear stress locates the sites of stenosis. Nephrol Dial Transplant, 27: 358-68, 2012

[52] Ene-Iordache B, Cattaneo L, Dubini G, Remuzzi A: Effect of anastomosis angle on the localization of disturbed flow in 'side-to-end' fistulae for haemodialysis access. Nephrol Dial Transplant, 28: 997-1005, 2013

[53] Semperboni C. Analisi computazionale patient specific dell'emodinamica in fistole arterovenose utilizzate come accesso vascolare per l'emodialisi a partire da immagini RM. Polimi Master thesis, 2012

[54] Manini S, Passera K, Huberts W, Botti L, Antiga L, Remuzzi A: Computational model for simulation of vascular adaptation following vascular access surgery in haemodialysis patients Computer Methods in Biomechanics Biomedical Engineering, 17(12):1358-67, 2014.

[55] Passera K, ManiniS, Antiga L, Remuzzi A: Patient-specific model of arterial circulation for surgical planning of vascular access. J Vasc Access, 14(2):180-92, 2013

[56] Remuzzi A & Ene-Iordache B: Novel paradigms for dialysis vascular access: upstream hemodynamics and vascular remodeling in dialysis access stenosis. Clinical Joural American Society of Nephrology, 8: 2186-93, 2013

[57] Antiga L, Piccinelli M, Botti L, Ene-Iordache B, Remuzzi A, Steinman DA: An image-based modeling framework for patient-specific computational hemodynamics. Med Biol Eng Comput. 46(11): 1097-112, 2008

[58] Sethian JA: Level set methods and fast marching methods: evolving interfaces in computational geometry, fluid mechanics, computer vision, and materials science, 3. Cambridge Univ Pr, 1999

[59] Lorensen WE, Harvey EC: Marching Cubes: A high resolution 3D surface construction algorithm. Computer Graphics, Vol. 21, Nr. 4, 1987

[60] Botti L, Piccinelli M, Ene-Iordache B, Remuzzi A, Antiga L: An adaptive mesh refinement solver for large-scale simulation of biological flows. Communications in Numerical Methods in Engineering, 26(1): 86-100, 2010

[61] Botti L, Van Canneyt K, Kaminsky R, Claessens T, Planken RN, Verdonk P, Remuzzi A, Antiga L: Numerical evaluation and experimental validation of pressure drops across a patient-specific model of vascular access for hemodialysis. Cardiovascular Engineering and Technology, 4(4): 85-499, 2013

[62] Botti L, Di Pietro DA: A pressure-correction scheme for convection-dominated incompressible flows with discontinuous velocity and continuous pressure. Journal of Computational Physics, 230: 572-585, 2011

[63] Huberts W, Bodeb AS, Kroonc W, Plankend RN, Tordoirb JHM, van de Vossea FN, Bosbooma EM: A pulse wave propagation model to support decision-making in vascular access planning in the clinic. Medical engineering & physics 34.2: 233-248, 2012

[64] Ene-Iordache B, Mosconi L, Antiga L, Bruno S, Anghileri A, Remuzzi G, Remuzzi A: Radial artery remodeling in response to shear stress increase within arteriovenous fistula for hemodialysis access. Endothelium, 10 (2):95-102, 2003

[65] Remuzzi A, Ene-Iordache B, Mosconi L, Bruno S, Anghileri A, Antiga L, Remuzzi G: Radial artery wall shear srtess evaluation in patients with arteriovenous fistula for hemosialisys access Biorheology, 40(1-3):423-30, 2003.

[66] Ku DN, Giddens DP, Zarins CK e Glagov S: Pulsatile flow and atherosclerosis in the human carotid bifurcation: Positive correlation between plaque location and low oscillating shear stress. Arteriosclerosis, thrombosis, and vascular biology, 5.3: 293-302, 1985.

[67] He X. & Ku D: Pulsatile flow in the human left coronary artery bifurcation: Average Conditions. J. Biomech. Eng. 118: 74–82, 1996

[68] Peiffer V, Sherwin SJ, Weinberg PD: Computation in the rabbit aorta of a new metric - the transverse wall shear stress - to quantify the multidirectional character of disturbed blood flow. J Biomech. 46(15): 2651-8, 2013

[69] Jeong J, Hussain F: On the identification of a vortex. Journal of Fluid Mechanics, 285: 69–94, 1995

[70] Malek AM, Alper SL, Izumo S: Hemodynamic shear stress and its role in atherosclerosis. JAMA, 282: 2035–2042, 1999

[71] Krejza J, Arkuszewski M, Kasner S, Weigele J, Ustymowicz A, Hurst R, Cucchiara B, Messe S: Carotid Artery Diameter in Men and Women and the Relation to Body and Neck Size. Stroke, 37(4): 1103–1105, 2006

[72] Lee SW, Antiga L, Spence JD, Steinman DA: Geometry of the Carotid Bifurcation Predicts Its Exposure to Disturbed Flow. Stroke, 39: 2341-2347, 2008

[73] Ford M, Alperin N, Lee SH, HoldsworthDW and Steinman DA: Characterization of volumetric flow rate waveforms in the normal internal carotid and vertebral arteries. Pysiol Meas, 26: 477-488, 2005

[74] Marshall I, Papathanasopoulou P, Wartolowska K. Carotid flow rates and flow division at the bifurcation in healthy volunteers. Physiol Meas, 25: 691– 697, 2004

[75] Hyun S, Kleinstreuer C, . Longest PW and Chen C. Particle-Hemodynamics Simulations and Design Options for Surgical Reconstruction of Diseased Carotid Artery Bifurcations. J Biomech Eng 126(2), 188-195, 2004

[76] Marie Y, Guy A, Tullett K, Krishnan H, Jones RG, Inston NG: Patterns of blood flow as a predictor of maturation of arteriovenous fistula for haemodialysis. J Vasc Access 15(3): 169-74, 2014

[77] Valen-Sendstad K, Piccinelli M, Steinman DA: High-resolution computational fluid dynamics detects flow instabilities in the carotid siphon: implications for aneurysm initiation and rupture? Journal of Biomechanics. pii: S0021-9290(14)00239-5, 2014

[78] McGah PM, Leotta DF, Beach KW, Eugene Zierler R, Aliseda A. Incomplete restoration of homeostatic shear stress within arteriovenous fistulae. Journal of Biomech Eng, 135: 011005, 2013

[79] Lee SE, Lee SW, Fisher PF, Bassiouny HS: Direct numerical simulation of transitional flow in a stenosed carotid bifurcation. Journal of Biomechanics 41(11): 2551‑2561, 2008

[80] Rayz VL, Boussel L, Lawton MT, Acevedo-Bolton G, Ge L, Young WL, Higashida RT, Saloner D: Numerical modeling of the flow in intracranial aneurysms: prediction of regions prone to thrombus formation. Ann Biomed Eng, 36: 1793-804, 2008

[81] Cho YI, Kensey KR. Effects of the non-Newtonian viscosity of blood on flows in a diseased arterial vessel. Part 1: Steady flows. Biorheology, 28(3-4): 241-262, 1991

[82] Jie Chen, Xi-Yun Lu: Numerical investigation of the non-Newtonian pulsatile blood flow in a bifurcation model with a non-planar branch. Journal of Biomechanics 39(5): 818‑832, 2006

[83] Ambrosi D, Quarteroni A, Rozza G: Modeling of physiological flow. Springer Editor. Chapter 1: 7-9

[84] Thomas JB, Milner JS, Rutt B, Steinman DA: Reproducibility of Image-Based Computational Fluid Dynamics Models of the Human Carotid Bifurcation. Annals of Biomedical Engineering, 31: 132–141, 2003

[85] McGah PM, Leotta DF, Beach KW, Aliseda A: Effects of wall distensibility in hemodynamic simulationsof an arteriovenous fistula. Biomech Model Mechanobiol, 13: 679–695, 2014

[86] Lee CJ, Uemiya N, Ishihara S, Zhang Y, Qian Y: A comparison of estimation methods for computational fluid dynamics outflow boundary conditions using patient-specific carotid artery. J. Engineering in Medicine. 227(6): 663-671

[87] Vignon-Clementel IE, Figureoa CA, Jansen KE, Taylor CA. Outflow boundary conditions for three-dimensional finite element modeling of blood flow and pressure in arteries. Comput. Method. Appl. Mech. Engrg, 195: 3776-3796, 2005

[88] Wang HY, Wu CH, Chen CY, Lin BS: Novel noninvasive approach for detecting arteriovenous fistula stenosis. IEEE Trans Biomed Eng, 61:1851-1857, 2014

[89] Grama M, Olesena JT, Riisa HC, M Selvaratnama, Urbania M: Stenosis detection algorithm for screening of arteriovenous fistulae. SEMCON conference paper 1–6, 2010

[90] Davies PF, Remuzzi A, Gordon E J, Dewey, C F Jr, and Gimbrone MA Jr: Turbulent fluid shear stress induces vascular endothelial cell turnover in vitro. Proc Natl Acad Sci 8: 2114–2117, 1986

[91] Fry DL: Acute vascular endothelial changes associated with increased blood velocity gradients. Circulation, 22: 165-197, 1968

[92] Prado CM, Ramos SG, Alves-Filho JC, Elias J Jr, Cunha FQ, Rossi MA: Turbulent flow/low wall shear stress and stretch differentially affect aorta remodeling in rats. Journal of Hypertension, 24: 503-515, 2006